AN INVESTIGATION OF FACTORS WHICH DEGRADE PHASE ACCURACY IN A VLF RELATIVE NAVIGATION SYSTEM

JOHN DOUGLAS MCKAY
and
GERRY LEE PRESTON

AN INVESTIGATION OF FACTORS WHICH DEGRADE PHASE ACCURACY IN A VLF RELATIVE NAVIGATION SYSTEM

by

John Douglas McKay
Lieutenant, United States Navy
B. S., Michigan State University, 1961

and

Gerry Lee Preston
Lieutenant, United States Navy
B.S.E.E., Rice University, 1961

Submitted in partial fulfillment
for the degree of

MASTER OF SCIENCE IN ENGINEERING ELECTRONICS

from the

UNITED STATES NAVAL POSTGRADUATE SCHOOL
December 1966

ABSTRACT

A VLF relative navigation system makes use of the fact that, at any given point on the earth, phase delay of a received VLF signal is highly stable and predictable. As the receiver is physically moved, phase delay changes linearly with distance from the transmitting station, so that by keeping track of the phase delay of the received signal from several VLF stations, one may keep an accurate plot of geographical position.

Two problems experienced in measuring phase delay are the diurnal shift and long path interference. An investigation is made into a method of predicting the diurnal phase shift and the resultant phase due to simultaneous reception of long and short path signals. Also investigated is a receiving antenna having a cardioid shaped radiation pattern which could provide discrimination against long path signals.

TABLE OF CONTENTS

Section		Page
1.	Introduction	9
2.	Characteristics of Very Low Frequency Radio Propagation	11
3.	A proposed Very Low Frequency Relative Navigation System	26
4.	VLF Receivers	35
5.	Frequency Standards	40
6.	Antennas	46
7.	Determination of Signal Strengths	63
8.	Calculation of VLF Phase Velocities	72
9.	Calculation of Resultant Signal Phase	85
10.	Conclusions	95
	Bibliography	97
Appendix		
I.	Geodesics and Long Paths	100
II.	Proportion of Daylight and Darkness on Paths of Propagation	109
III.	Loop Antenna Calculations	121
IV.	Cardioid Antenna Calculations	124

LIST OF ILLUSTRATIONS

Figure		Page
2-1.	Electrical Field Structure for Waveguide Modes	13
2-2.	Attenuation Rates Over Predominantly Sea Water Paths for n=1 (Experimental and Theoretical)	19
2-3.	Attenuation Rates Over Predominantly Sea Water Paths for n=2 (Experimental and Theoretical)	19
2-4.	Attenuation Rate of the First Mode for a Perfectly Conducting Earth and an Imperfectly Reflecting Ionosphere	20
2-5.	Attenuation Rate of the Second Mode for a Perfectly Conducting Earth and an Imperfectly Reflecting Ionosphere	20
2-6.	Attenuation Rate of the First Mode for an Imperfectly Conducting Earth and an Imperfectly Reflecting Ionosphere	21
2-7.	Attenuation Rates for Predominantly Sea Water Paths for Moderate and Low Sunspot Numbers (Experimental)	21
2-8.	Phase Velocity of the First or Dominant Mode for a Perfectly Conducting Earth and a Perfectly Reflecting Ionosphere	22
2-9.	Phase Velocity of the First Mode for a Perfectly Conducting Earth and an Imperfectly Reflecting Ionosphere	22
2-10.	Phase Velocity of the First Mode for an Imperfectly Conducting Earth and an Imperfectly Reflecting Ionosphere	23
2-11.	Phase Velocity as a Function of Frequency Showing Effect of Reflecting Height and Magnetic Field	24
2-12.	Attenuation rates deduced from various experimental data	25
2-13.	Experimental phase velocities with pertinent theoretical data	25
2-14.	Experimental phase velocities with pertinent theoretical data	25
3-1.	Relative Phase of Haiku Omega Station, 13.6 kHz, as Received at Monterey	28

LIST OF ILLUSTRATIONS
(continued)

Figure		Page
3-2.	Trapezium Approximation of Diurnal Shift	29
3-3.	Phasor Diagram	32
4-1.	VLF Tracking Receiver	36
5-1.	Precision Crystal Oscillator	43
6-1.	Loop Radiation Pattern	47
6-2.	Loop Relative Output	48
6-3.	Loop Relative Phase Shift	49
6-4.	Cardioid System Schematic	50
6-5.	Cardioid Radiation Pattern	51
6-6.	Cardioid Relative Output ($0^o < \alpha < 180^o$)	52
6-7.	Cardioid Relative Output ($-180^o < \alpha < 0^o$)	53
6-8.	Cardioid Relative Phase Shift ($0^o < \alpha < 180^o$)	55
6-9.	Cardioid Relative Phase Shift ($-180^o < \alpha < 0^o$)	56
6-10.	Cardioid Amplitude	59
6-11.	Cardioid Phase	61
7-1.	Calculated Attenuation of 13.6 kHz Signal on Trinidad to Monterey Short Path for 1 Oct. 1966	66
7-2.	Calculated Attenuation of 13.6 kHz Signal on Trinidad to Monterey Long and Short Paths for 1 Oct. 1966	67
7-3.	Calculated Attenuation of 13.6 kHz Signal on Forestport to Monterey Short Path for 1 Oct. 1966	69
7-4.	Calculated Attenuation of 13.6 kHz Signal on Haiku to Monterey Short Path for 1 Oct. 1966	69
7-5.	Observed Relative Carrier Level of Trinidad 13.6 kHz at Monterey, 30 Aug. to 2 Sept. 1966	70
7-6.	Observed Relative Carrier Level of Forestport 13.6 kHz Signal at Monterey, 5 Sept. to 8 Sept. 1966	70

LIST OF ILLUSTRATIONS
(Continued)

Figure		Page
7-7.	Observed Relative Carrier Leval of Haiku 13.6 kHz Signal at Monterey, 2 Sept. to 5 Sept. 1966	70
8-1.	Calculated Phase Velocity Curves	74
8-2.	Calculated Phase Delay on Trinidad to Monterey Short Path at 13.6 kHz	78
8-3.	Aldra to Monterey Phase Delay, Short Path	79
8-4.	Haiku to Monterey Phase Delay, Short Path	80
8-5.	Forestport to Monterey Phase Delay, Short Path	81
8-6.	Trinidad to Monterey Phase Delay, Short Path	82
8-7.	Typical Diurnal Shifts on a Polar Path	83
8-8.	Observed and calculated phase of GBR at Sydney, Australia for October 1961 and October 1966 respectively	84
9-1.	Attenuation on GBR to Sydney Short and Long Paths at 16 kHz	87
9-2.	Short Path and Resultant Phase of GBR at Sydney	88
9-3.	Attenuation on GBR to Wellington Short and Long Paths at 16 kHz	89
9-4.	Short Path and Resultant Phase of GBR at Wellington	90
9-5.	Short Path and Resultant Phase of GBR at Wellington (Short Path 7 km Longer)	91
9-6.	Phasor Representation of a 24-hour Phase and Amplitude Curve	92
9-7.	Phasor Representation of a 24-hour Phase and Amplitude Curve with a Large Diurnal Phase Shift	93
9-8.	Phasor Representation of Loss of Carrier Level Due to Rapid Phase Change	94
I-1.	Geodetic and Parametric Latitudes	100
I-2.	Ellipse of Geodesic	102

LIST OF ILLUSTRATIONS
(continued)

Figure		Page
I-3.	Parametric and Geocentric Latitudes	102
II-1.	Point of Sunrise on Great Circle Path	110
II-2.	Sunrise/Sunset at Ionospheric Height	111
II-3.	Revised Position of Sunrise Point	112
II-4.	Sunrise Position Coordinates	112
II-5.	Revised Position of Sunset Point	113
II-6.	Sunset Position Coordinates	113
II-7.	Possible Positions of Sunrise and Sunset on Great Circle Path	114
III-1.	Loop Antenna	121
III-2.	Loop Geometry	121
III-3.	Phasor Diagram	122
IV-1.	Cardioid Geometry	124
IV-2.	Loop Phasor Diagram	125
IV-3.	Cardioid Adjustment	125
IV-4.	Cardioid Phasor Diagram	126
IV-5.	Angular Relationships	127
IV-6.	Loop Phasors ($180^{o} < \alpha < 360^{o}$)	129
IV-7.	Cardioid Phasors ($180^{o} < \alpha < 360^{o}$)	129

1. Introduction

Certain characteristics of the Very Low Frequency portion of the electromagnetic spectrum make feasible many important applications, some relatively new and others not so new. One striking application is the transmission of radio waves to submerged submarines which have not even an antenna above the surface. Another is the transmission of messages to mobile units operating halfway around the world.

The application which inspired this paper, however, is that of a VLF relative navigation system. Such a system, using VLF transmitting stations already broadcasting for other purposes, has been tested and found feasible for both ships and aircraft operating at long distances from the transmitting stations. The system makes use of the fact that, at any given point on the earth, phase delay of a received VLF signal is highly stable and predictable. As the receiver is physically moved, phase delay changes linearly with distance from the transmitting station, so that by keeping track of the phase delay of the received signal from several VLF stations, one may keep an accurate plot of geographical location.

This paper attempts to resolve one particular problem associated with the relative navigation system application. This problem is the result of interference noted from the reception of a VLF signal which has travelled along a great circle path more than halfway around the circumference of the earth, i.e., interference of the so-called long path signal with the short path signal. Section 2 is a study of aspects of propagation peculiar to the VLF spectrum, while Section 3 discusses in detail the VLF relative navigation system. Sections 4 and 5 provide information on VLF receivers and frequency standards

applicable to the navigation system.

Discrimination against the long path signal is desirable to minimize navigational errors; this may be accomplished easily aboard ship by the use of an antenna system having a cardioid-type radiation pattern. VLF antennas are discussed in Section 6, with emphasis on the use of a loop in conjunction with a whip antenna to provide the desired cardioid pattern.

Sections 7 and 8 provide a detailed discussion of the prediction of attenuation and phase delay of VLF waves. These predictions are necessary if one is to calculate in advance the effect of the long path signal on the observed resultant phase delay at any given geographical location. Section 9 provides an example of just such a calculation. Observed data on long path signals could not be obtained locally, since there were no VLF stations at a sufficient distance from Monterey, California, to provide a measurable long path signal. It was thought that station GBR, transmitting on 16.0 Khz from Rugby, England, would provide this data; however, this station was off the air during the period available for experimental investigation (July-November 1966).

2. Characteristics of Very Low Frequency Radio Propagation

The characteristics of VLF propagation which make these frequencies useful for long distance communication and highly accurate (to within a few parts in 10^{11}) frequency comparison are a relatively low path attenuation which is stable with time and a phase shift which is very constant, and predictable, over long periods of time. VLF also overcomes (to a large extent) the two major disadvantages of HF transmissions, unreliability during ionospheric disturbances and fairly rapid and deep fading [28].

The major disadvantages of VLF transmissions are the very narrow (20-150 Hz) bandwidths available and the large transmitting installations that are necessary. The narrow bandwidths available are due to the small spectrum (10-30 kHz) and, mainly, to the high Q of VLF antenna systems. Since these antennas are very short with respect to a wavelength their input impedance consists of a large reactance and a very small radiation resistance. To obtain maximum efficiency, therefore, it is mandatory that all losses in the antenna, loading coils, and ground be kept to a minimum. The resulting low resistance coupled with high reactance gives these systems an inherent high Q and consequent narrow bandwidth.

The high powered transmitters are required to obtain large areas of coverage and because of the high level of atmospheric noise present at VLF. This atmospheric noise is due mainly to lightning discharges which are centered in frequency at about 11 kHz. A typical discharge will radiate approximately 10^5 joules and have a 3db bandwidth of about 12 kHz [6].

Theory of VLF Propagation

The two theories that have been predominantly used to explain the

characteristics of VLF propagation are the ray theory and the waveguide mode theory. It has been stated [28] that the mode and ray theories are related and, if all modes and all rays were taken into account with appropriate corrections for losses, both methods would yield the same results. However, at long distances the mode theory is simpler to use because only one mode need be considered but many individual rays must be taken into consideration. At short distances many modes are present making the mode theory calculations complicated, but only a few rays need be considered since the higher order rays are incident on the ionosphere at much smaller angles where the reflection coefficient is small. In this paper the only distances which will be considered are those for which the mode theory calculations may be assumed valid with only one mode present (i.e., greater than 4000 km from the transmitter).

From observed measurements of the electric field within the earth-ionosphere waveguide it has been found that the model shown in Figure 2-1 can be used to approximate the actual physical case. The mode of principal interest at long distances is the TM_1, shown in the left side of Figure 2-1, the TM_2 and higher order modes being small enough in amplitude beyond 4 Mm to be neglected. From Watt and Croghan [18], for distances greater than 1 Mm the vertical electric field can be represented as the sum of a very few waveguide modes:

$$E_z = \sum_{n=1}^{n=1 \text{ to } 3} E_{z,n} \qquad d > 1 \text{ Mm}$$

Here $E_{z,n}$ is the electric field strength for each particular mode (in db relative to 1 v/m)

$$E_{z,n} \text{ [db, v/m]} = 10 \text{ Log } P_r + K_n' - 10 \text{ Log } f$$

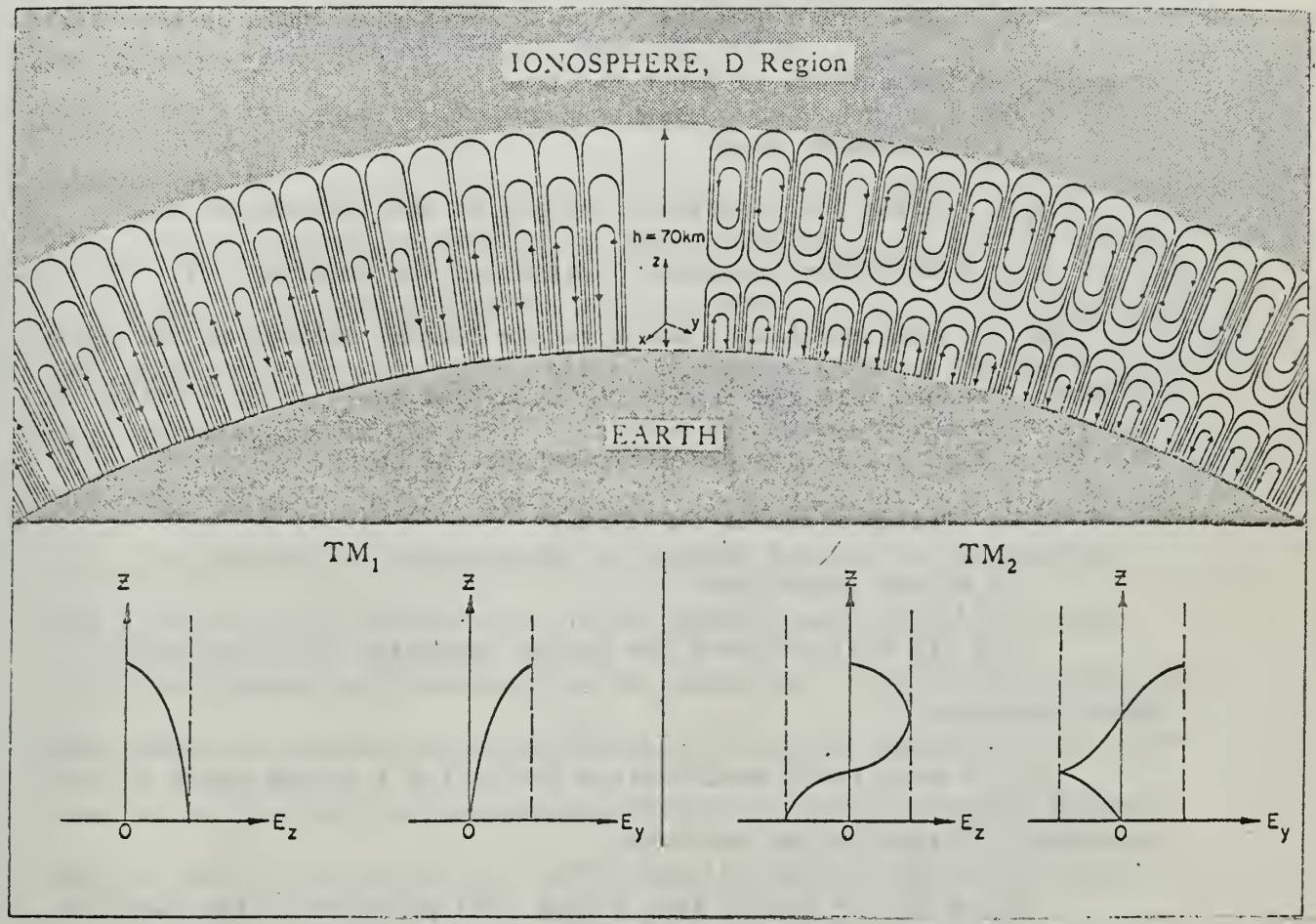

Figure 2-1.

Electrical field structure for waveguide modes.

(Wait [11])

$$- 10 \text{ Log } h_{i,t} + 10 \text{ Log} \Lambda_{n,t}$$

$$- 10 \text{ Log } (a \sin d/a) - 10 \text{ Log } h_{i,r}$$

$$+ 10 \text{ Log} \Lambda_{n,r} + 20 \text{ Log } G_{h,n}$$

$$- L_{d,n} - \alpha d/10^6$$

where

P_r = power radiated into the half space above the earth (watts).

K_n' = 104.3 db for modes 1,2, --- a constant which relates field strengths at the surface to power radiated.

f = frequency (Hz)

$h_{i,t}$ = effective ionospheric height at the transmitter (m).

$h_{i,r}$ = effective ionospheric height at the receiver (m).

$\Lambda_{n,t}$ = mode excitation modification factor, defined as the ratio of power launched into the concentric spherical shell guide relative to that for a flat guide with perfectly conducting earth.

a = earth's radius ($\approx$ 6.4 Mm)

d = path length (m)

(a sin d/a) accounts for energy spreading in the spherical guide structure.

$\Lambda_{n,r}$ = mode field modification factor for a curved earth at the ionospheric height at the receiver.

20 Log $G_{h,n}$ = height gain factor (db) relative to the field at the surface.

$L_{d,n}$ = loss due to discontinuities along the path (db).

α = effective attenuation rate in db/Mm (different for each mode).

These factors are discussed at some length by Watt and Croghan and will not be commented on further in this paper, with the exception of the

attenuation factor.

For paths with uniform boundary surfaces, the attenuation factor is given by

$$\alpha = M(\phi)\alpha_i + \alpha_g$$

where

$M(\phi)$ = earth's magnetic field factor

$$= \frac{\text{attenuation with magnetic field}}{\text{attenuation without magnetic field}}$$

ϕ = direction of propagation with respect to the earth's magnetic field

α_i = attenuation constant of the ionosphere

α_g = attenuation constant of the ground.

α_i and α_g are related to the reflection coefficients of the earth and the ionosphere which are in turn related to the conductivities of these two media.

The attenuation curves shown in Figures 2-2 and 2-3 are derived for $M(\phi) = 1$, i.e. independent of the earth's magnetic field. Here ℓ is the conductivity gradient of the ionosphere. From these curves the difference in attenuation of the first two modes is apparent. At 15 kHz and for a 4 Mm path the smallest difference in signal strength between the two modes is about 13 db, justifying the earlier assumption that only the first mode need be considered at these distances. Figures 2-4, 2-5, and 2-6 are shown for comparison and while there are some differences in the attenuation curves for n = 1, the n = 2 curves show the same larger attenuation rates (with respect to the n = 1 curves). Figure 2-7, while not a set of calculated curves, shows very vividly the effect of the earth's magnetic field on the attenuation factor.

The phase velocity of a certain mode for a fixed set of conditions can be determined from a solution of the mode equation. This is done by Wait [11] and Wait & Spies [23] resulting in the curves shown in Figures 2-8 through 2-11. The effect on phase velocity of several factors can be seen here. Assuming a constant frequency, it can be seen that the height of the ionosphere has a large effect on the phase velocity, lowering it with increasing height. This is the cause of the familiar diurnal shift of phase delay of a received VLF signal. At night the D layer of the ionosphere (the lowest layer) dissipates and the effective height of the ionosphere is increased by about 20 km. The resultant decrease in phase velocity causes an increase in the phase delay of the received signal as compared with a local standard. After sunrise the sun's rays ionize the lower portions of the ionosphere, the D layer returns, and the process repeats itself.

Comparing Figures 2-8 and 2-9 will show that an imperfectly reflecting ionosphere (e.g., an exponential variation of ion density) will increase the phase velocity slightly. The effect of finite ground conductivity is seen in Figure 2-10, indicating that the phase velocity will be slightly lower over land (as compared to sea). From Figure 2-11 it appears that the effect of the earth's magnetic field on phase velocity is small in comparison to the other factors. (The effect is much more pronounced for the n = 2 mode; however, that mode is being considered negligible in amplitude here). Wait and Spies have many more curves of phase velocity, attenuation factors, excitation factors, etc., which would be of interest to anyone planning a more detailed study of VLF propagation.

Experimentally Obtained Data

Figures 2-12 through 2-14 along with the experimental curves in Figures 2-2, 2-3 and 2-7, are examples of the vast amount of experimental data taken on the attenuation rates and phase velocities of VLF radio waves. The agreement of this data with calculated curves in certain cases (e.g., Figures 2-13 and 2-14) is remarkable and provides a basis for using the calculated curves to predict phase velocities and attenuation rates.

Figure 2-12 shows the many factors that must be taken into account in predicting attenuation rates: time of day, direction of propagation, frequency, and ground conductivity. In the 10-30 kHz frequency range, the range of attenuation rates is about 4 db/Mm (minimum to maximum) indicating that for long distances a considerable difference in signal strength could be expected depending on the path traveled.

In this paper the experimental data will be used wherever possible and the calculated curves will be used as a check and to fill in the gaps not covered by experimental evidence (e.g., attenuation of the $n = 2$ mode).

Summary

The one characteristic of VLF radio transmissions of interest in this paper is the good phase stability of the signals over long periods of time and the predictability of this phase. Because of this phase stability frequency comparisons over long distances are possible with an accuracy on the order of one part in 10^{11}. The amplitude and phase of these signals can be predicted fairly accurately at distances greater than one megameter from the transmitter by using the mode theory of propagation. The actual solution of the mode theory equations is a

rather complex problem; however, the solutions of Wait and others have been published and show a very good agreement with experimental evidence in some cases.

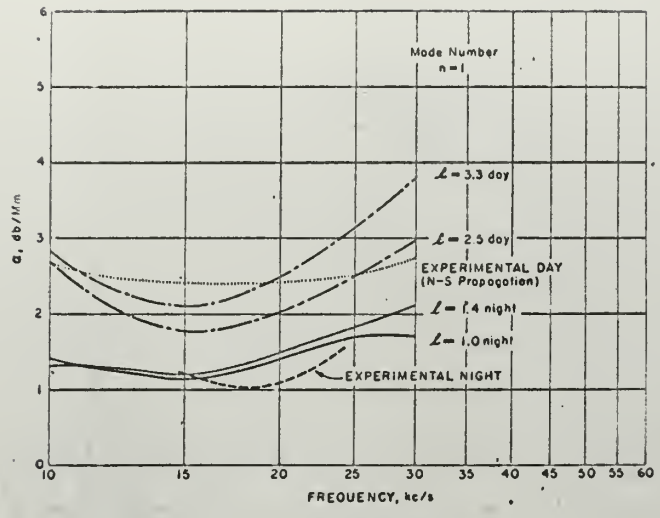

Figure 2-2

Attenuation rates over predominantly sea water paths for n=1 (experimental and theoretical).

(Watt & Croghan [18])

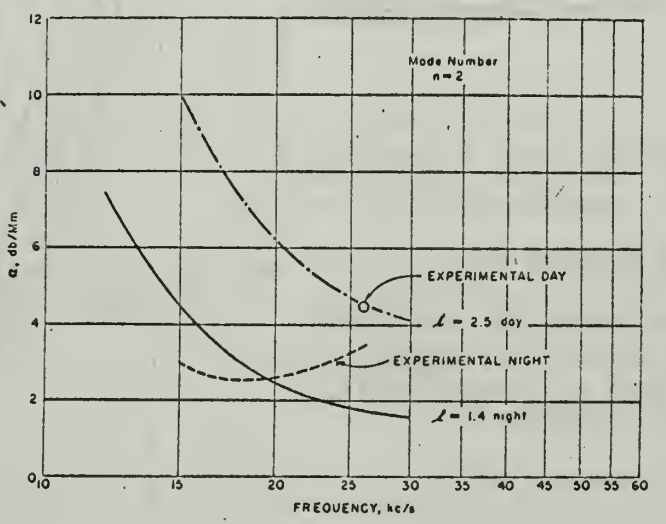

Figure 2-3

Attenuation rates over predominantly sea water paths for n=2 (experimental and theoretical).

(Watt & Croghan [18])

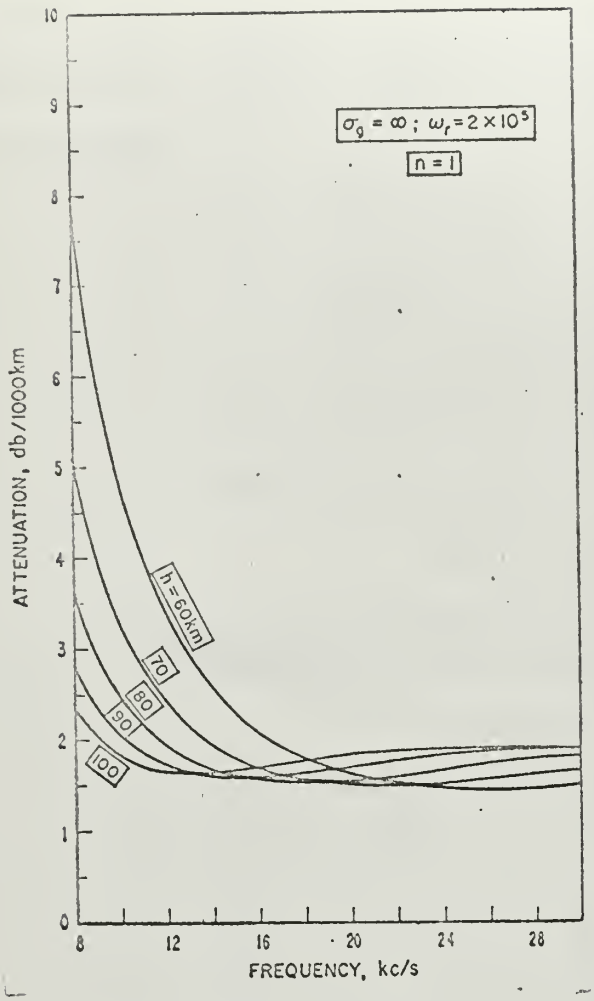

Figure 2-4

Attenuation rate of the first mode for a perfectly conducting earth and an imperfectly reflecting ionosphere.

(Wait [11])

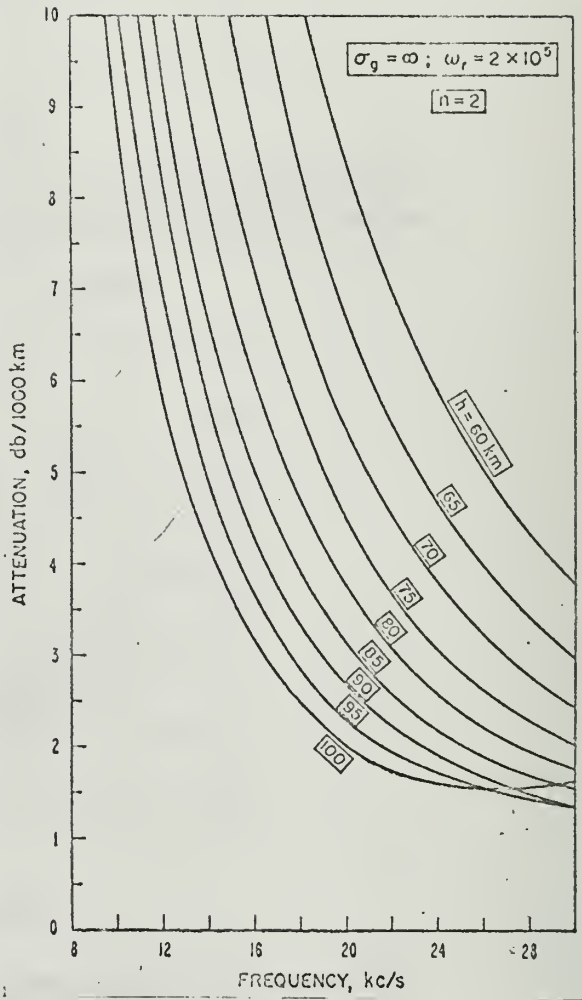

Figure 2-5

Attenuation rate of the second mode for a perfectly conducting earth and an imperfectly reflecting ionosphere.

(Wait [11])

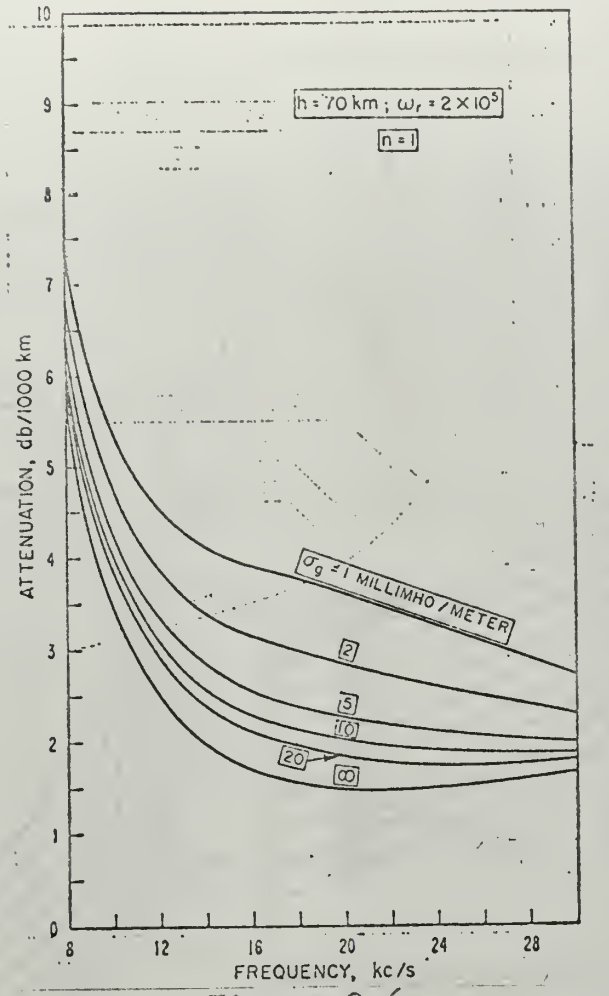

Figure 2-6

Attenuation rate of the first mode for an imperfectly conducting earth and an imperfectly reflecting ionosphere.

(Wait [11])

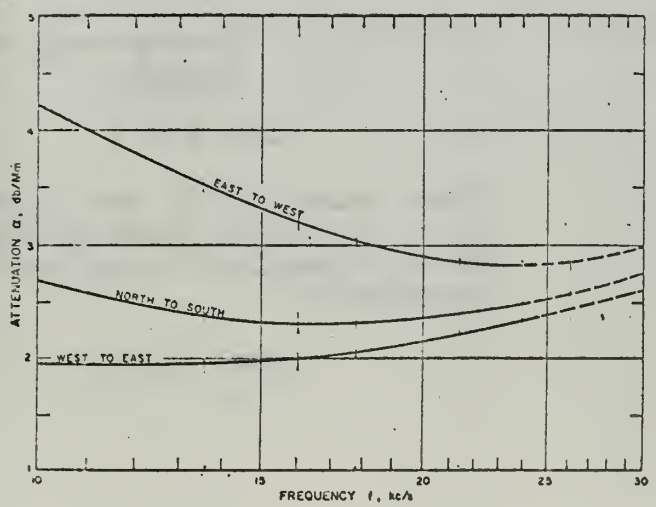

Figure 2-7

Attenuation rates for predominantly sea water paths for moderate and low sunspot numbers (experimental).

(Watt & Croghan [18])

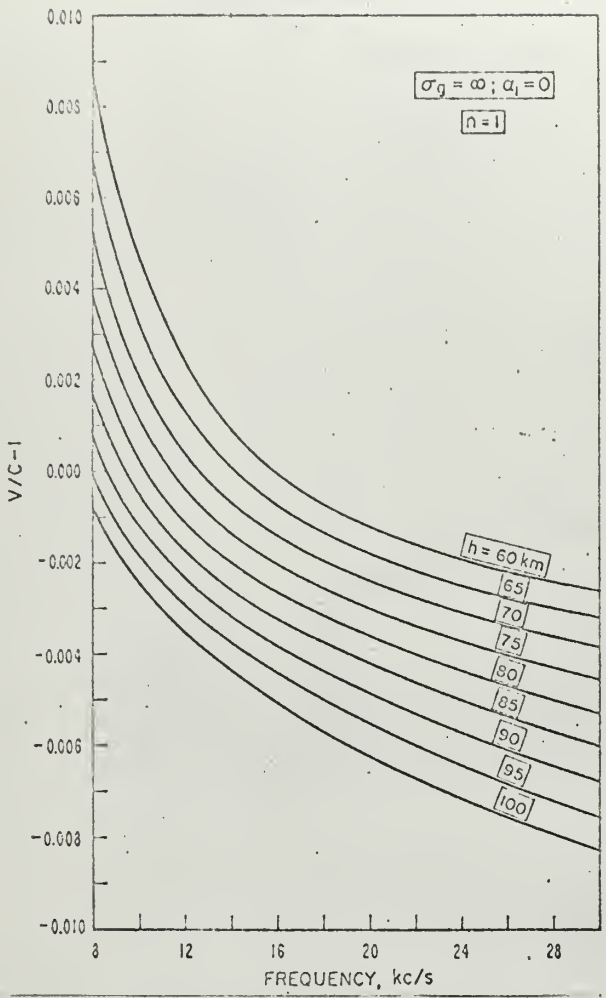

Figure 2-8

Phase velocity of the first or dominant mode for a perfectly conducting earth and a perfectly reflecting ionosphere.

(Wait [11])

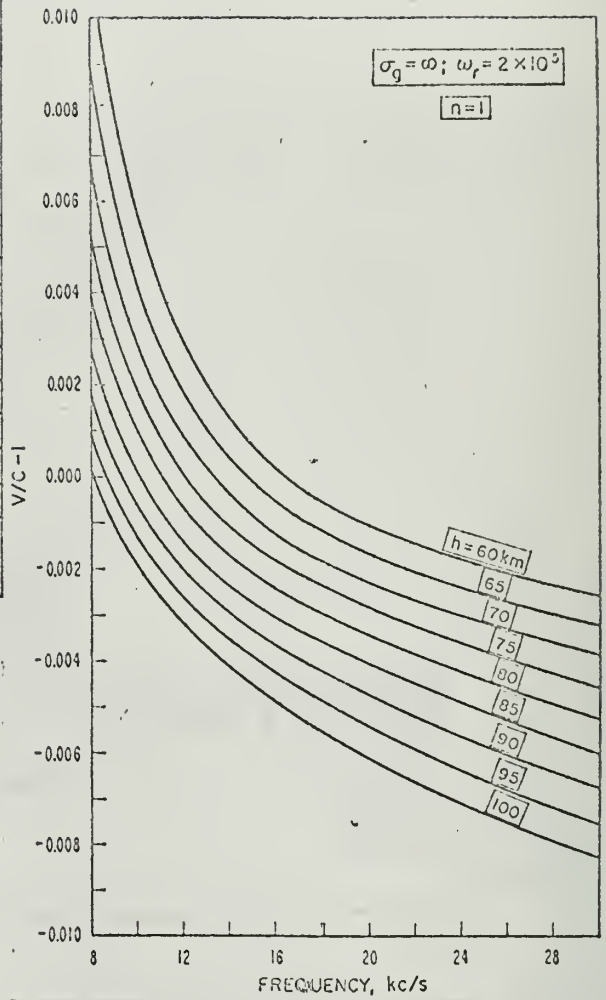

Figure 2-9

Phase velocity of the first mode for a perfectly conducting earth and an imperfectly reflecting ionosphere.

(Wait [11])

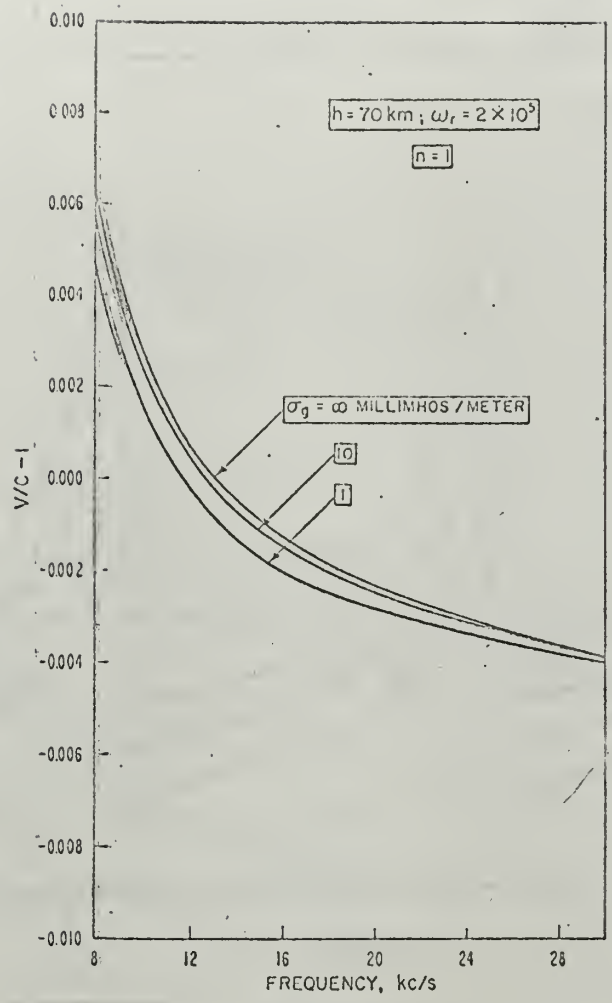

Figure 2-10

Phase velocity of the first mode for an imperfectly conducting earth an an imperfectly reflecting ionosphere.

(Wait [11])

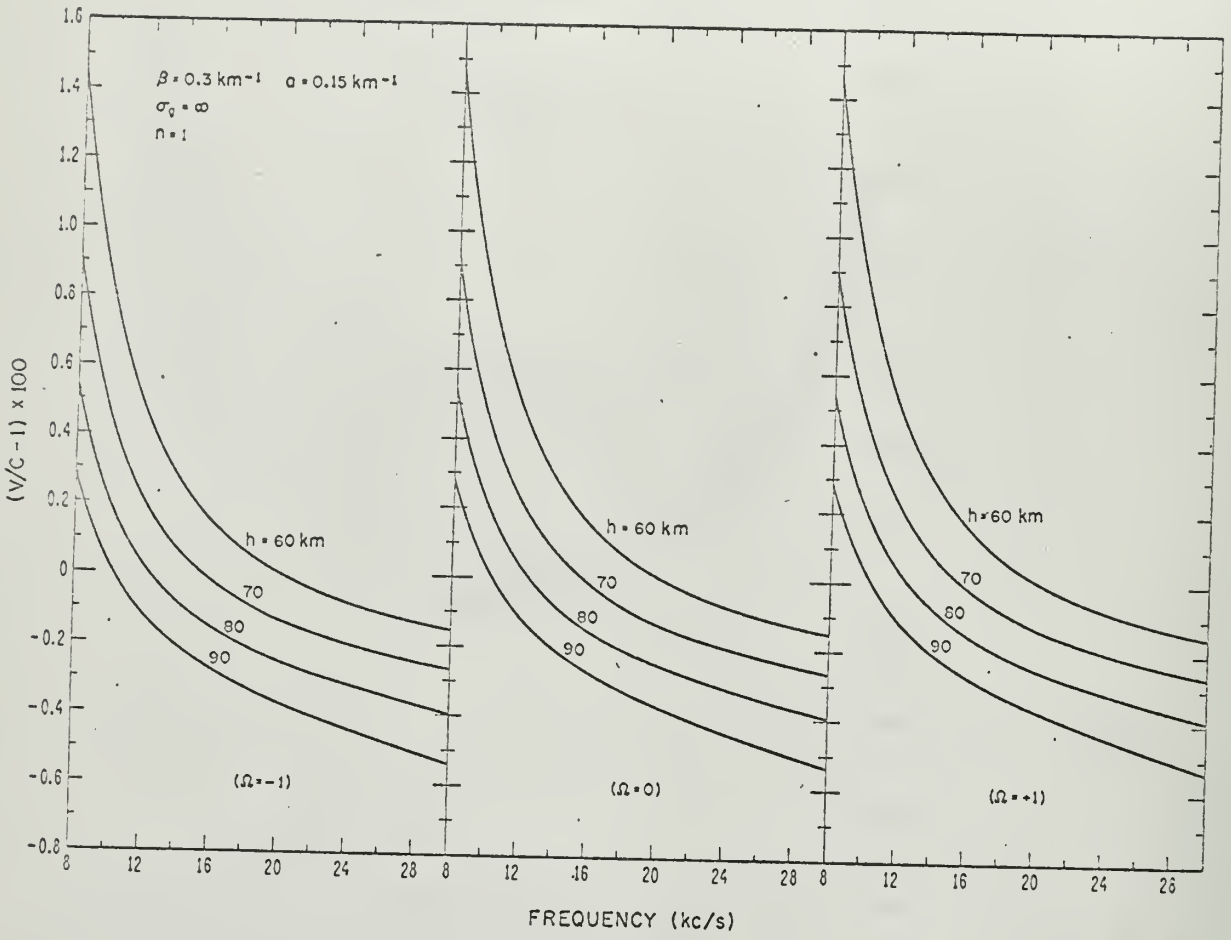

Figure 2-11

Phase velocity as a function of frequency showing effect of reflecting height and magnetic field.

(Wait & Spies [23])

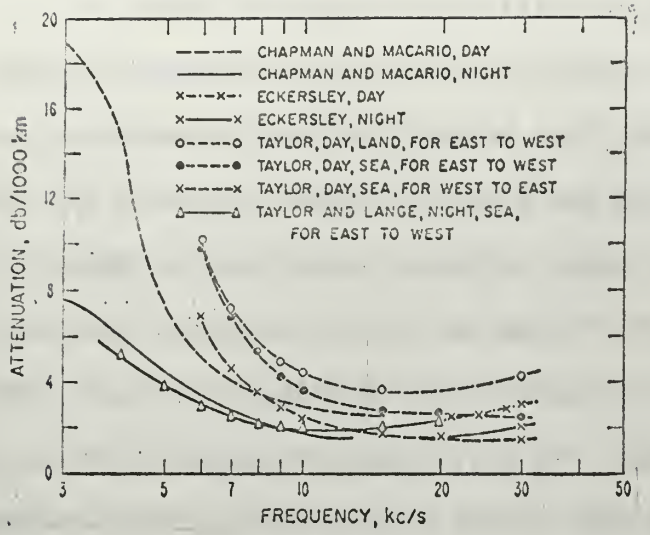

Figure 2-12

Attenuation rates deduced from various experimental data

(Wait [11])

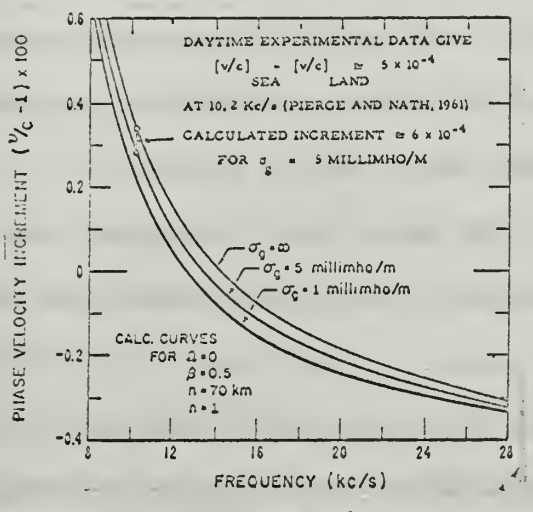

Figure 2-13

Experimental phase velocities with pertinent theoretical data.

(Wait & Spies [23])

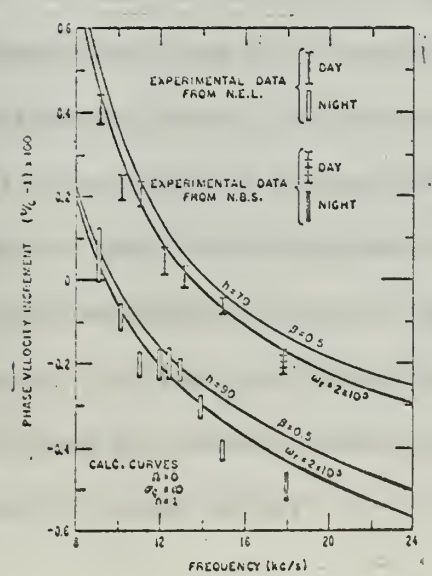

Figure 2-14

Experimental phase velocities with pertinent theoretical data.

(Wait & Spies [23])

3. A Proposed Very Low Frequency Relative Navigation System

The proposed very low frequency (VLF) relative navigation system has been outlined by Stanbrough and Keilly [16], and presented in detail by Lake [25]. The system has many advantages, providing (1) relative simplicity; (2) a long range, accurate system with worldwide coverage; (3) the capability of using VLF phase-stabilized stations already on the air, with no requirement for additional stations; and (4) reliable 24-hour coverage. The only required equipment for shipboard use of this system are one or more phase tracking receivers and, preferably, a directional antenna system such as a loop used in conjunction with a sense antenna (whip). The latter is discussed elsewhere in this paper. One recorder channel to provide a continuous record of phase for each tracking receiver used would also be helpful.

The extreme phase stability of VLF radio waves propagated over great distances, plus or minus one microsecond under normal conditions, is the foundation of this navigation system. An oscillator at the distant VLF transmitter provides the station with phase-stabilized emissions, while a stable oscillator aboard ship at the same frequency provides the local reference. This local oscillator is used in conjunction with a phase tracking receiver to provide an indication of relative phase of the VLF wave at the receiver. A high-quality quartz crystal oscillator would be suitable for use aboard ship and a typical unit in use at the U.S. Naval Postgraduate School provides a frequency drift (due to crystal aging) of about 2.5 parts in 10^{11} per day. This drift would be determined for the particular oscillator in use aboard ship and its frequency would then be corrected on a regular basis, perhaps daily, to keep it within some specified frequency offset. At the time of taking a fix,

the phase variation due to the frequency offset of the oscillator would then be known and a compensation could be made.

Assuming a nominal value of 3×10^8 m/sec for the phase velocity of a VLF wave, the number of microseconds required for the wave to travel one nautical mile is found to be 6.18. In view of this, it is clear that for each increase in phase delay of 6.18 μsec, the ship has moved one nautical mile farther from the transmitter.

The VLF relative navigation system makes use of the foregoing; by keeping track of the phase of two or more stations as the ship moves away from an initial known point, an indication of the ship's geographical position is available at all times. By programming a computer to make the calculations and necessary corrections, one could even obtain a continuous track of the ship's movement. It is, however, necessary to use VLF stations far enough away that mode interference is not experienced, and only the first waveguide mode is involved (greater than 4000 km).

One problem complicating the navigation system is that of the diurnal phase variation experienced with VLF waves. Fortunately, however, this variation is predictable and the shipboard navigator can be provided with tables to correct for the phenomenon. Figure 3-1 illustrates the diurnal variation, and is an actual plot of the phase of the 13.6 kHz signal from the Omega Navigation System transmitter located at Haiku, Hawaii, referred to a rubidium vapor frequency standard at the U.S. Naval Postgraduate School.

A first approximation to a solution of the problem of diurnal phase change may be made by assuming a trapezoidal pattern, or trapezium, as shown in Figure 3-2. A comparison with Figure 3-1 shows the similar-

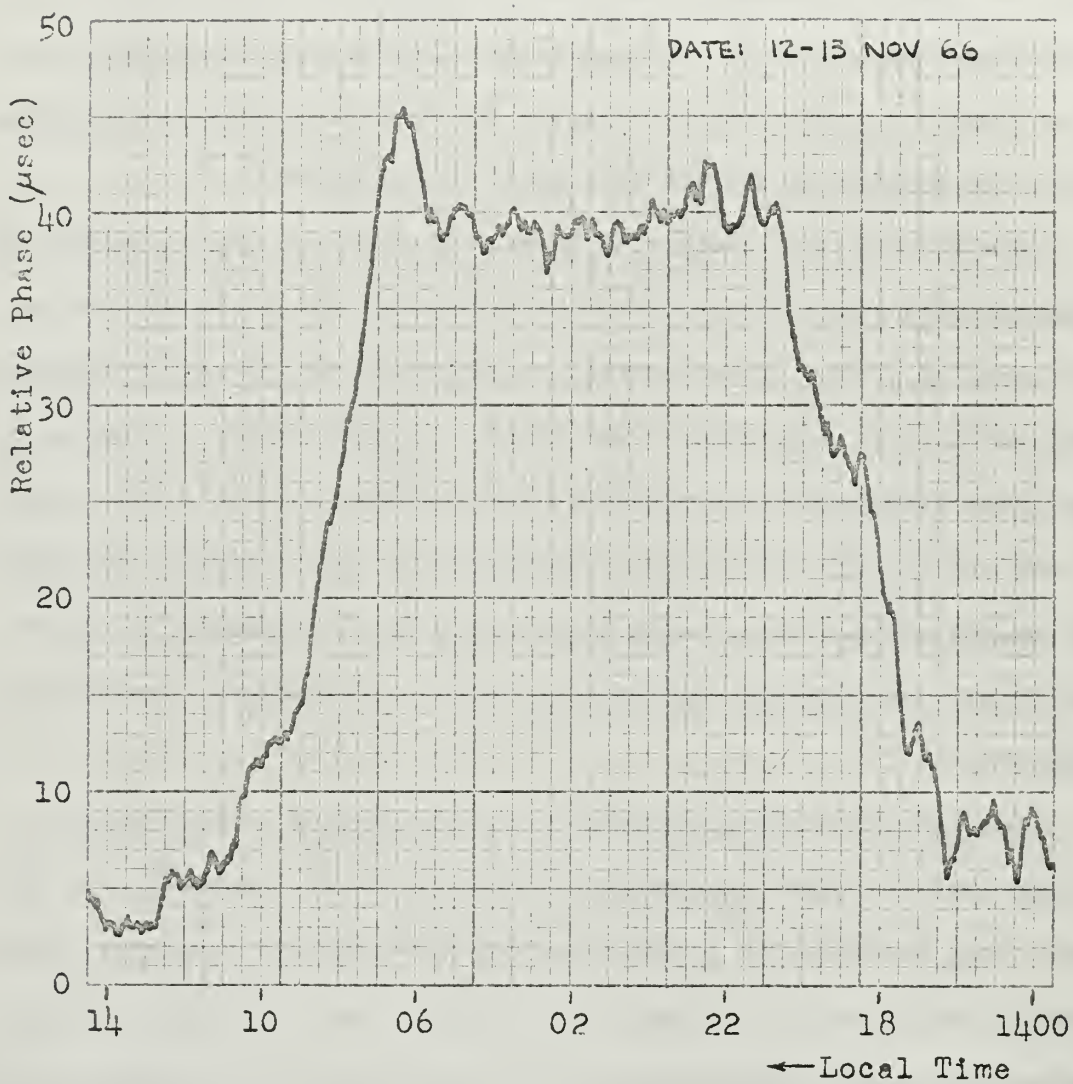

Figure 3-1. Relative Phase of Haiku Omega Station, 13.6 kHz, as Received at Monterey

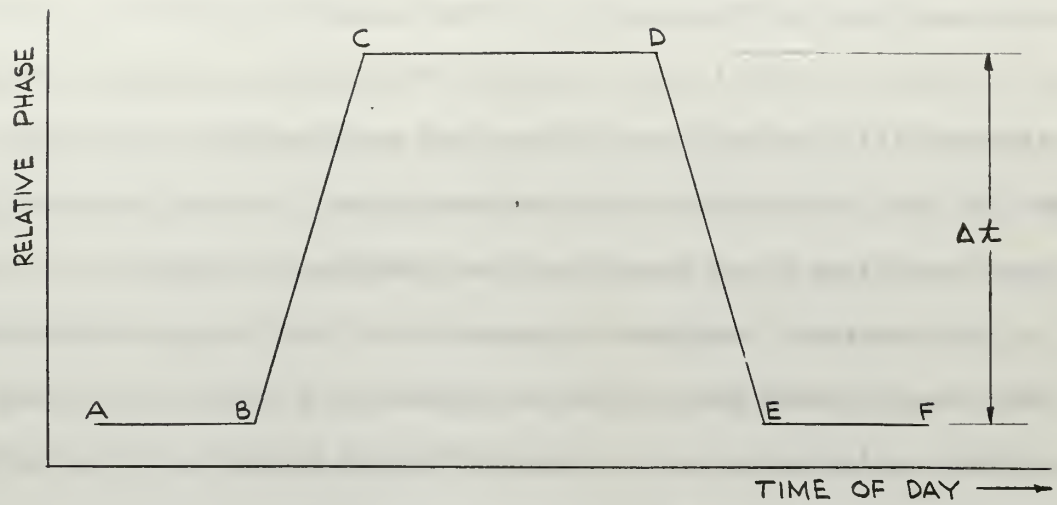

Figure 3-2. Trapezium Approximation of Diurnal Shift.

ity of the two patterns. Time intervals AB and EF have the same values of relative phase and represent the period of time during which the entire propagation path is in sunlight. Assuming the transmitter location west of the receiver, point B is the time of local (receiver) sunset, point C indicates sunset at the transmitter, point D local sunrise, and point E sunrise at the transmitter. It has been found that correction of sunrise and sunset times to those viewed from the effective height of the lower boundary of the D layer of the ionosphere (about 70 km during the day and 90 km at night) provides better correlation with the observed discontinuities in the phase plot.

The diurnal shift (Δt in Figure 3-2) varies with distance from the transmitter, since it is caused by the fact that the phase velocity of a VLF wave has one value during the day and a lower value at night. As discussed elsewhere in this paper, these phase velocities may be predicted for given paths, allowing the calculation of the diurnal shift at any given geographical position.

Other, more precise, models of the phase plot may be determined

(as shown later in this paper). Whichever model is used, the procedure to be used in navigation is to predict the deviation of phase from the reference (all-daylight path) value, for the particular time of the desired fix, and subtract from indicated phase. As mentioned earlier, these deviations could be prepared and published in advance.

An electronic navigation system such as that being considered is known as a circular grid system, as opposed to a hyperbolic system such as LORAN, which makes use of phase difference between a master and a slave station. In the VLF relative system, navigational charts may be overprinted with circles representing lines of constant time delay drawn about each VLF station as a center. These would be constructed using the 6.18 μsec/mile discussed earlier. (It should be noted that use of these charts introduces a small error since the phase velocity of a VLF wave is not exactly equal to the velocity of light; hence, actual phase delay differs slightly from 6.18 μsec/mile.)

In order to use such an overprinted chart, one would first need to plot the ship's position from other information, which would then be used as a reference for future fixes obtained by the VLF relative system. The phase indicated by the tracking receivers for each VLF station being tracked would also be noted at the time the reference fix was obtained. At the time the VLF fix is desired, the phase readings on each VLF station would again be noted. For those stations whose propagation paths are all in daylight, the phase difference could then be transferred directly to the chart. This would be in the form of a time difference for each station which would indicate the distance travelled away from or toward the station. A short segment of a circle for each station would be interpolated on the chart between those segments already over-

printed. The intersection of these circular segments would then be the ship's position.

For those stations whose propagation paths are partially or totally in darkness, the correction for diurnal shift corresponding to the ship's approximate position and time of day would have to be applied. There would be a correction for the time of the reference position and one for the time of the new position. The corrections would be subtracted in both cases, since phase delay is greater at night. After the diurnal correction has been applied, the phase information is used as described in the last paragraph.

It is important to note that, since stations being used for navigation will be at least 4000 km distant, the circles of constant phase will appear as straight lines in small areas. In fact, if overprinted charts are not available, straight-line approximations of the circular segments may be used if the true bearings are known from the ship to the transmitting stations. These could be obtained from a previously-prepared table. The straight-line approximations will be adequate if the ship's position is known within about 50 miles of its actual position [25].

A very complete example of a navigational fix obtained by this method, and using the trapezoidal approximation of diurnal phase shift, is given by Lake [25].

There are certain problems associated with the VLF relative navigation method, some of which are (1) cycle-slipping, (2) interference from the long path (around the world) signal, (3) inexactness of the trapezoidal model of diurnal phase change, (4) transmitter outages, (5) frequency offset of the transmitter master oscillator, and (6)

sudden ionospheric disturbances (SID's).

Cycle-slipping is a phenomenon in which the tracking receiver indicates and tracks one or more full cycles ahead or behind the true relative phase of the VLF wave. This often occurs near sunrise or sunset when relative phase is changing rapidly. Frequently the diurnal phase shift will be more than one cycle, so that cycle-slipping is especially likely to occur. Cycle-slipping may also be caused by interference from waveguide modes higher than the first order, and by interference from the long path signal [27].

The long path signal may be thought of as a phasor, having some magnitude and phase relative to the short path signal. Together, the two signals form a resultant which constitutes the composite signal received by an omnidirectional antenna. Figure 3-3 shows the phasor addition of the two signals, with $\tilde{E}_1 = |E_1| \angle 0^\circ$ representing the short path signal (taken with phase = 0° for convenience), $\tilde{E}_2 = |E_2| \angle \theta^\circ$ the long path signal, and $\tilde{E}_R = |E_R| \angle \varphi^\circ$ the resultant. The notation $\tilde{E}$ is used to indicate a phasor quantity. Since the long path signal may travel

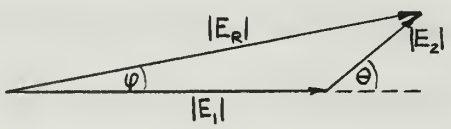

Figure 3-3. Phasor Diagram

hundreds or thousands of miles farther than the short path signal, the angle θ may take on any value between 0° and 360°. It is clear, then, that for any value of $|E_2|$ which is an appreciable fraction of $|E_1|$, the resultant will vary considerably from the short path signal. Since such

a condition will occur under favorable circumstances, the need for a directional antenna which will discriminate against the long path signal is evident. The long path signal is particularly likely to be appreciable near the antipode of the transmitter, as well as at other locations where the short path signal for any reason undergoes high attenuation concurrent with low attenuation of the long path signal.

The trapezoidal model of diurnal phase change, discussed earlier in this section, is a good approximation in many cases; however, there are also frequent instances in which it introduces excessive error. A more refined model of diurnal phase change, useful in all cases, is presented in a later section.

Transmitter outages may occur on a scheduled basis for maintenance, in addition to those unscheduled outages due to equipment failure which invariably occur. During the interval of a transmitter outage, the indicated phase of a tracking receiver remains constant. Since the transmitter master oscillator normally continues running during the outage, the receiver will resume tracking on the correct cycle when VLF transmissions resume, if the receiver has remained geographically stationary. If, however, the ship has moved a distance on the order of some multiple of a wavelength, the receiver will track the incorrect cycle (the same one as if it had remained stationary). The problem of determining the correct cycle is known as lane identification, and is minimized in other systems by utilizing lower frequency (longer wavelength) signals. Additional information, such as the ship's dead reckoning track or positional information from other means, is necessary to identify the correct lane, or cycle.

Frequency offset of the transmitter master oscillator of a VLF

station is occasionally made, for example to bring the transmitted frequency into coincidence with the United States Frequency Standard. These frequency corrections would occur infrequently and advance notice thereof could be given to users of a VLF relative navigation system. With such advance notice, the navigator would have no difficulty applying a correction for the offset.

Sudden ionospheric disturbances are caused by three phenomena: solar flares, magnetic storms, and high altitude nuclear bursts. While these disturbances occur infrequently, they cause phase disturbances on VLF circuits over wide areas of the earth, causing errors in VLF navigation in the case of severe disturbances. Chilton, Steele, and Crombie [19] have pointed out that solar flares cause a depression in the effective height of the ionosphere, which in turn causes increased phase velocity, resulting in a lower value of relative phase at the receiving point. A typical flare has an onset time of one to 30 minutes and requires from one to two or three hours to return to normal. A typical phase change caused by the flare might be 10 microseconds, but varies with path length, frequency, and amount of ionosphere height change.

4. VLF Receivers.

The receiver used to obtain experimental data on phase and amplitude of various VLF stations for this paper was a Tracor Model 599G VLF phase tracking receiver. A simplified block diagram showing the essential elements of such a tracking receiver is seen in Figure 4-1. The output of the block marked VLF Receiver is at an intermediate frequency of 1 kHz with a certain phase ϕ_{VLF}, and is one input of the phase comparator. The other input of the phase comparator, a 1 kHz signal of phase ϕ_A, is derived from the external frequency standard. The output of the phase comparator provides the electronic phase shifter with an error signal $\Delta\phi$, which tells the phase shifter how much to shift the phase of the external standard to maintain phase tracking. The output of the phase shifter then goes to the frequency synthesizer which provides the reference signal ϕ_A. The condition for phase tracking is $\Delta\phi = \phi_{VLF} - \phi_A = 0$.

The phase tracking servo and long integration time of the receiver provide the capability of tracking with an input signal-to-noise ratio of -50 db. The rated sensitivity is 0.01 microvolts of signal at the antenna terminals to provide phase tracking. Using a loop antenna made by Tracor especially for this receiver (Model 599-600), this corresponds to a signal strength of 0.3 microvolts/meter. With a 150 sec servo time constant (front panel switch provides time constants of 5, 15, 50, and 150 sec) the equivalent noise bandwidth is 0.002 Hz. A front-panel switch on the receiver allows selection of either a broadband RF filter or any one of five narrowband ones. The narrowband filters provide an RF bandwidth of 500 Hz, while the IF bandwidth is 50 Hz. The receiver is tunable from 8.0 to 31.9 kHz in 0.1 kHz steps.

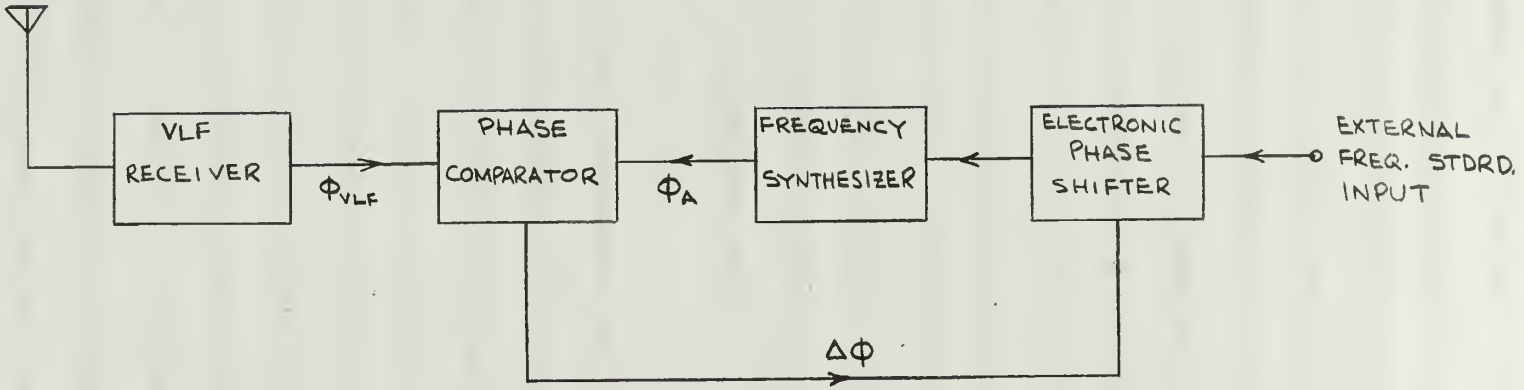

Figure 4-1. VLF Tracking Receiver

The receiver has available several outputs that proved useful in experimental work for this paper: (a) 100 μsec and 10 μsec full scale recorder outputs, (b) a front panel bi-directional digital counter for cumulative phase change, (c) a 100 kHz coherent output, and (d) an AGC-derived relative carrier level recorder output. The 100 μsec and 10 μsec full scale recorder outputs use the receiver's internal phase comparator to give a dc voltage level proportional to the phase difference between the external frequency standard and the received VLF signal. (Note: the phase comparator of the receiver does not actually operate at 1 kHz as indicated in the discussion of Figure 4-1. The receiver contains two linear phase comparators; one operates at 100 kHz to provide the 10 μsec full scale recorder output, while the other operates at 10 kHz for the 100 μsec full scale recorder output.) These recorder outputs were convenient and proved quite satisfactory for continuous monitoring of the phase of any phase-stable VLF station. Moseley Model 5100B strip chart recorders were used for monitoring these and the other receiver outputs, as desired.

The electronic phase shifter of the receiver actually operates at 10 MHz. One cycle of phase shift then corresponds to 0.1 μsec drift which feeds the front panel bi-directional phase counter. This digital counter provides a cumulative indication, so that by taking readings at two different times, one may determine by subtraction the exact phase drift that has occurred during the elapsed time.

The 100 kHz coherent output of the receiver provides a 100 kHz signal from the frequency synthesizer section shown in Figure 4-1. This signal thus has a phase corresponding to that of the received VLF signal. This output proved useful as an input to an external phase comparator,

allowing a check on the phase of any local frequency standard (the other input to the comparator) with respect to the received VLF signal. Both the rubidium vapor frequency standard and the quartz crystal oscillator in use at the Naval Postgraduate School have 100 kHz outputs suitable for this (see Frequency Standards section).

The relative carrier level output of the tracking receiver provides a dc level proportional to the AGC voltage developed in the receiver and is thus a relative indication of received signal strength of the VLF station. The AGC has a range of approximately 40 db, and peaks at about 40 db above the minimum signal necessary for tracking.

One problem occasionally encountered in experimental work was the very long integration time of the receiver. For example, a cardioid antenna system must be adjusted for proper phase and amplitude of the whip antenna when changing to a new frequency. To get a good indication of phase and amplitude, it was usually necessary to wait five to 10 minutes after each adjustment of the whip. Since several adjustments are normally required, the process can be quite time-consuming.

Adjustments are particularly time-consuming if one is receiving one of the Omega stations. Each of these stations transmits only about one second out of 10, so the long integration time problem is compounded. At the time of the experimental work for this paper, there were four Omega stations in operation (there are planned ultimately to be eight). Each station operates on a time-shared basis on two frequencies, 10.2 and 13.6 kHz. They transmit an unmodulated waveform in a prescribed sequence for a prescribed length of time (e.g., 0.9 sec, 1.1 sec, etc.) to facilitate identification. Still in the planning stage for the system are the addition of 11.33 kHz by all stations on the time-shared

basis, as well as transmissions of 12.00 and 12.75 kHz (not on a time-shared basis) by some of the stations. In order to obtain phase and amplitude information on an individual station, it is necessary to clamp the AGC and blank the receiver during the time the desired station is not transmitting. In the laboratory at the Naval Postgraduate School, this was accomplished by a Tracor Omega Gating Unit. This unit may be used with four tracking receivers simultaneously, and a modification for the receiver is provided which allows switching between normal receiver operation and Omega operation. The unit proved highly satisfactory and much valuable data was obtained using Omega stations.

It was useful in the experimental work to have an auxiliary VLF receiver available which could conveniently be tuned from station to station for quick audio identification. The receiver used was a model AN/SRR-11, and a similar type would no doubt be useful for auxiliary purposes in the shipboard VLF relative navigation system.

5. Frequency Standards

A good frequency standard must be used at both the phase-stabilized VLF station and the ship using the VLF relative navigation system; hence it is a vital part of the system. Its use in the system aboard ship is shown in Figure 4-1.

There are two basic types of precise frequency standards: the quartz crystal oscillator and the atomic frequency standard. The former is characterized by a predictable frequency drift as the crystal ages, while the latter has either an extremely small drift or none at all.

The past twenty years have seen great achievements in the field of precise frequency control; today, time difference or frequency may be measured more precisely than any other physical quantity. Using an atomic hydrogen maser, a frequency stability (RMS deviation from the mean) of 2 parts in 10^{14}, over a one-day averaging period, may now be obtained [30]. One problem which has arisen in the growth of technology of frequency standards is a lack of standardization of the definitions of certain terms. Two of these are short-term stability and long-term stability. The former refers to average frequency deviation measured over a time interval sufficiently short that long-term effects may be neglected. Since the averaging period is not standardized, it must be specified; it varies from a fraction of a second to perhaps one minute. Long-term stability refers to slow changes in average frequency, and is usually specified for crystal oscillators by stating fractional frequency deviation per day, e.g., 5 parts in 10^{11} per day. Since atomic frequency standards have little or no systematic drift, specifications for them will often be given in terms of standard deviation or RMS deviation from the mean over a specified time interval such as one

day.

Quartz Crystal Oscillators

There are many factors which affect the frequency of quartz crystal oscillators, which must be taken into account or compensated for. In particular, frequency stability is a function of: (a) temperature; (b) time (aging); (c) stress, vibration, and acceleration; (d) drive level, and (e) nuclear effects. These effects are discussed by Gerber and Sykes [29].

Ambient temperature changes account for the principal frequency change effects in most crystal units. Current practice in precision oscillators is the use of a double proportional oven to control the temperature of the crystal unit. This provides a method of removing heat from around the crystal at the same rate it is generated. A simpler, but less desirable, method uses a thermostatically-controlled oven. In this method, temperature varies between a lower and an upper limit, whereas it is maintained constant when using proportional control.

The effect of time (aging) in a quartz crystal oscillator is easily observed by the variation in frequency deviation from day to day. According to Gerber and Sykes [29], aging of thickness shear crystals is caused by four factors: (a) temperature gradient effects lasting several minutes to several hours after a thermal disturbance, (b) stress relief effects, (c) change of mass effects, and (d) structural changes due to imperfections in the crystal lattice. In all crystal oscillators there seems to exist an initial stabilization period, normally lasting a few weeks, in which the oscillator has not yet attained its ultimate frequency stability.

The effects on frequency stability of stress, vibration, acceleration, etc., may be reduced by careful design of mounting structures. Austin [24] has made an experimental study of the effects of vibration, shock, and swinging motion on frequency stability of several commercial crystal oscillator units. He concluded that stability of these units was degraded negligibly under conditions similar to those which might be encountered in a shipboard environment.

Another factor affecting crystal stability is drive level, or amplitude of vibration. A typical 2.5-MHz crystal unit might exhibit a change in frequency deviation of from 1 part in 10^9 to about 8 parts in 10^7 with a change in drive level from 3 to 1000 microwatts [29]. For this reason, automatic gain control is used in precision crystal oscillators.

Nuclear radiation also has an effect on the frequency of crystal oscillators; the extent of this effect is discussed in the literature [13], [15], and [26].

Figure 5-1, from Gerber and Sykes [29], shows a schematic diagram of a modern precision crystal oscillator. The double oven is shown, and proportional control would be used. To maintain a constant drive level, a large amount of negative feedback would be used in the amplifier, in addition to the AGC.

The Sulzer Model D2.5 is a crystal oscillator of the type shown in Figure 5-1 and was in use at the Naval Postgraduate School for the experimental work of this paper. Its drift rate was determined to be about 2.5 parts in 10^{11} per day. Other units of this general type often have drift rates of about 1 part in 10^{11} per day, while similar units used to stabilize transmissions of some U.S. Navy VLF transmitters have average daily drift rates as low as a few parts in 10^{13} [29]. This

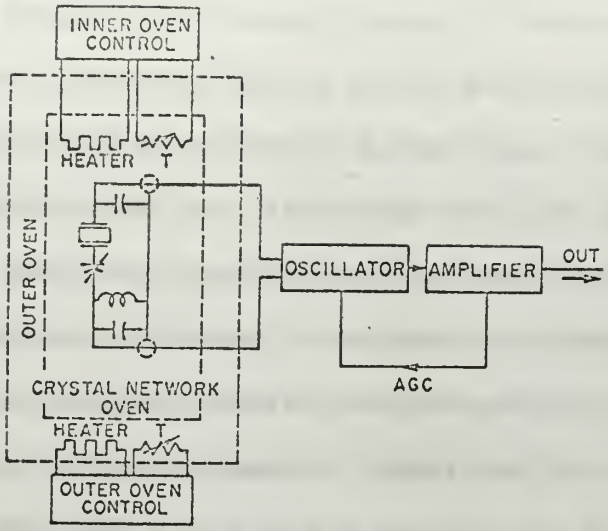

Figure 5-1. Precision Crystal Oscillator

general type of oscillator should be well suited for shipboard use in a VLF relative navigation system.

Atomic Frequency Standards

It is interesting at this point to note the difference between a primary and a secondary frequency standard. The former is a self-calibrating device which is intrinsically accurate. The latter, however, requires calibration against a known precise frequency before it can be considered a standard. A quartz crystal oscillator may thus be classified only as a secondary frequency standard. There are several types of atomic frequency standards, including the hydrogen maser, the cesium beam standard, and the rubidium vapor standard. The latter, considered a secondary frequency standard since its frequency initially must be compared with some other standard, was used at the Naval Postgraduate School as an adjunct to the preparation of this paper. The hydrogen maser and the cesium beam standard are both primary frequency standards. All three of these atomic standards are now commercially available.

Atomic standards in general derive their precise frequencies from frequencies corresponding to the energy involved in the transition of electrons between energy states in particular types of atoms, such as hydrogen, cesium 133, and rubidium 87. The cesium and rubidium standards operate on the same basic principles; both have found wide use in VLF applications as well as other uses. Space does not permit detailed descriptions, but since the rubidium standard was used in some of the experimental work for this paper, its basic operation will be described.

The heart of the rubidium standard is a high-quality quartz oscillator, whose frequency is stabilized by a passive resonance cell filled with rubidium and an inert buffer gas. The operation of the resonance cell is based on an optical pumping principle. The rubidium vapor in the cell is illuminated by filtered light from a rubidium lamp. A microwave signal is applied to a microwave cavity surrounding the resonance cell. This signal is obtained by multiplying the frequency of the quartz oscillator. When the frequency corresponds to atomic resonance, energy transitions are induced in the rubidium atoms and a photo detector observes these transitions through changes in the amount of light absorbed as a function of applied microwave frequency. A servo loop connects the detector output and oscillator, locking the oscillator to a frequency corresponding to the center of the resonance line. Since the resonance frequency is influenced to some extent by the pressure of the buffer gas in the resonance cell, this pressure must be properly adjusted when the standard is manufactured. The cell in then sealed and the unit is ready to serve as a frequency standard.

Rubidium vapor frequency standards have been designed for U.S. Army tactical applications and for guided missiles and aircraft. They should

also be readily adaptable to a shipboard environment. State-of-the-art characteristics for these standards, according to McCoubrey [30], include an RMS deviation from the mean of 5 parts in 10^{12} for a one-day averaging period and a systematic drift of less than 3×10^{-11} per month.

Cesium beam frequency standards are presently being used as the United States Frequency Standard (maintained by the National Bureau of Standards, Boulder, Colorado) and to stabilize the VLF transmitters of the Omega navigation system stations. While the short-term stability of cesium beam standards is not as good as that of rubidium standards, their principal advantages are excellent long-term stability and high intrinsic reproducibility. McCoubrey [30] gives the state-of-the-art long-term stability as 2×10^{-13} per day (RMS deviation from the mean). Stations of the Omega navigation system effect an intercomparison of their cesium beam standards periodically (currently every four hours), and are thus able to control their stability to better than 1×10^{-11} per day [32].

The Varian Model V-4700 is the rubidium vapor standard that was used at the Naval Postgraduate School for the authors' experimental work. Over a period of about four months, this unit exhibited an RMS deviation from the mean of 1.36×10^{-11}, using an averaging period of one day.

6. Antennas

As mentioned in Section 3, the long path signal at times can introduce serious error in the VLF relative navigation system. For this reason, it is desirable to use some means of discriminating against this component of a received VLF signal. The cardioid antenna system, which has been widely used in radio direction finding and radio compass applications, provides a ready solution to the problem. The basic theory of this system has been described by Terman [3] and others, and will be reiterated and elaborated upon in this section. The loop antenna, basic to a cardioid set-up, will first be discussed, then the cardioid system itself, and finally the results of measurements on antennas at the Naval Postgraduate School will be presented.

The Loop Antenna

The loop antenna, in various forms, has been used for many years. One of its earliest applications was reception of stations in the broadcast band when this service was in its infancy. Loops used for VLF work, as well as most other applications, have a diameter which is small compared to a wavelength. A loop may be circular, rectangular, triangular, diamond-shaped, or some other similar configuration. Kraus [2] states that far fields of loop antennas of different shapes are the same if the areas enclosed by the loops are the same.

A vertical loop antenna produces a polar radiation pattern in the familiar figure-eight shape, as shown below in Figure 6-1. The xy-plane is parallel to the surface of the earth. Maximum response, of course, occurs when the plane of the loop is oriented parallel to the direction of arrival of the electromagnetic wave.

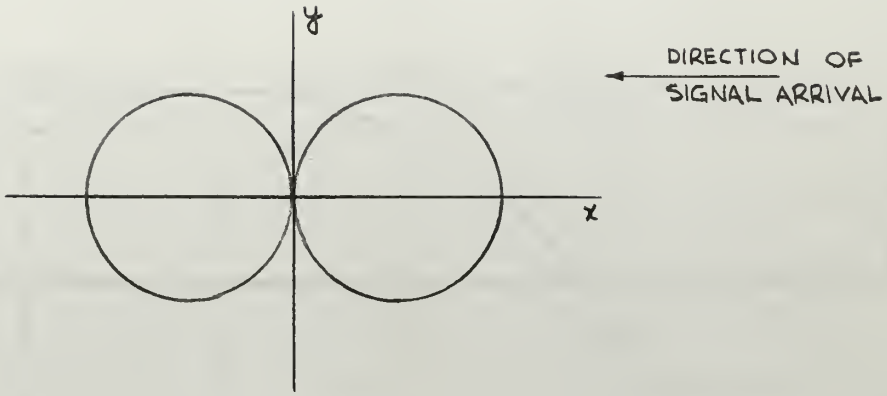

Figure 6-1. Loop Radiation Pattern

Appendix III describes the theory of operation of the loop antenna. Equations are derived there for the relative response and phase shift as the antenna is rotated from 0^o clockwise to 360^o. Figures 6-2 and 6-3 show plots of these equations for 0^o to 180^o. The frequency is taken to be 20 kHz, and the loop is assumed square, with the length of a side equal to 1.635 m. (This length was chosen because it was the measured length of a loop available for experimental work.) The loop is assumed parallel to the y-axis of Figure 6-1 and direction of arrival is from right to left along the x-axis as shown. The angle of rotation α is taken as the angle between the normal to the loop and the positive x-axis (this is shown in Figure III-2), so that $\alpha = 0^o$ and 180^o corresponds to zero response, while $\alpha = 90^o$ and 270^o are the points of maximum response.

The graph of Figure 6-2 was arbitrarily terminated at -35 db for convenience, since output theoretically goes to $-\infty$ db at $\alpha = 0^o$ and 180^o. For rotation from 180^o to 360^o, the amplitude pattern is exactly the same as for the first 180^o of rotation (this is obvious from inspection of Figure 6-1).

For the phase pattern, the second 180^o was not plotted in order to show greater detail. At $\alpha = 180^o$ and $\alpha = 360^o$, there is a discon-

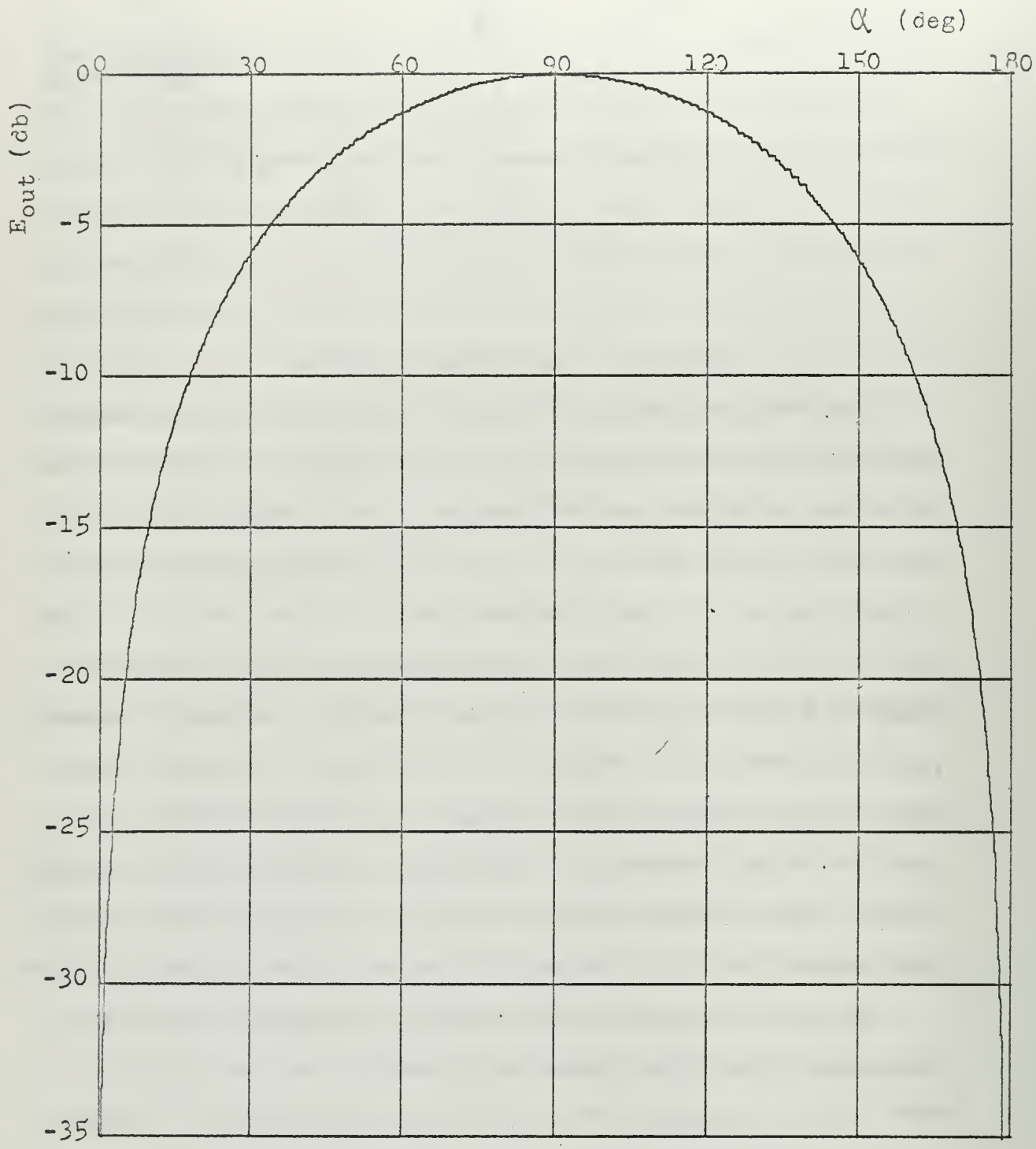

Figure 6-2. Loop Relative Output

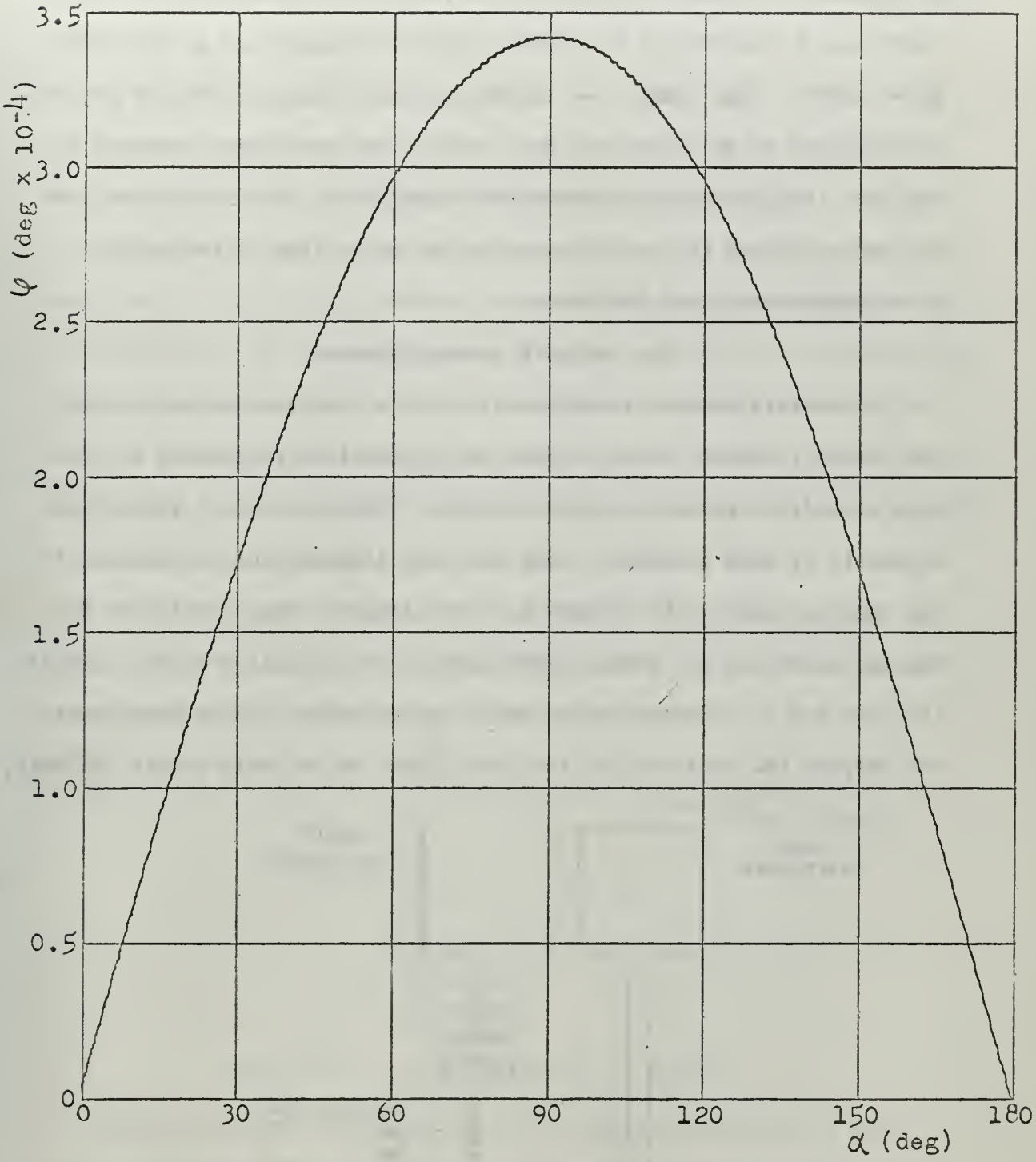

Figure 6-3. Loop Relative Phase Shift

tinuity of 180°. The pattern for α = 180° to α = 360° looks the same as Figure 6-3, except it appears inverted, i.e., at α = 180°, $\varphi \rightarrow$ -180°; at α = -270°, φ = -(180° + 3.4 x 10^{-4} deg); and at α = 360°, $\varphi \rightarrow$ -180°. (The symbol $\rightarrow$ is used to imply the existence of the discontinuities at α = 180° and α = 360°.) The 180° phase reversal on the back side of the loop antenna is significant, for one must be careful not to rotate the loop antenna to the wrong side of the null if phase measurements are important.

The Cardioid Antenna System

A cardioid antenna system consists of a loop antenna and a whip (or "sense") antenna whose outputs are appropriately combined to produce a cardioid-shaped radiation pattern. Figure 6-4 is a simplified schematic of such a system. Both the loop diameter and the height of the whip are small with respect to a wavelength. Some provisions for tuning, which are not shown, would normally be installed at the base of the loop and at the base of the whip. There would also be provisions for varying the amplitude of the loop signal or the whip signal, or both,

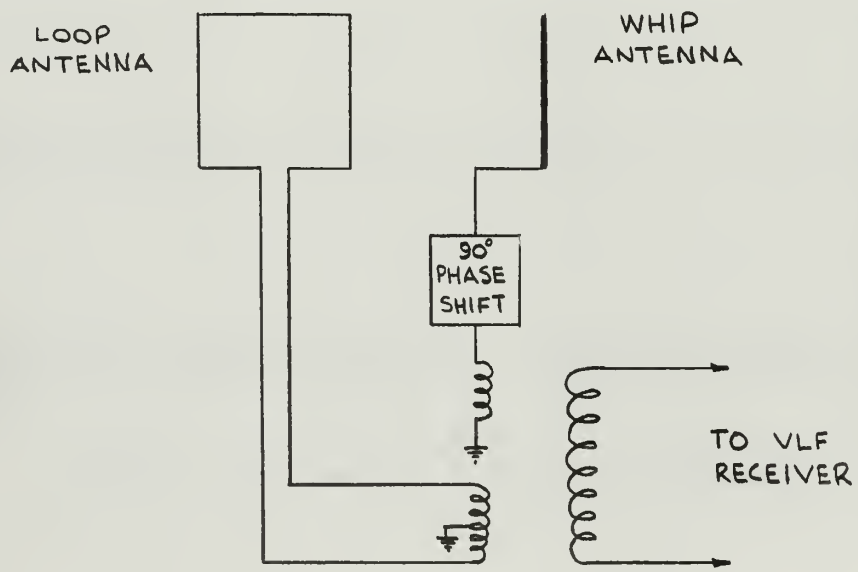

Figure 6-4. Cardioid System Schematic

as well as provisions for varying the whip phase a small amount above and below the 90° phase shift shown. These provisions are necessary to allow adjustment to obtain the cardioid pattern. The adjustment consists of making the whip antenna component of the VLF signal equal in magnitude and phase to the loop contribution, for the case in which the plane of the loop is oriented toward the distant transmitting station.

Appendix IV contains the equations necessary to plot the phase and magnitude of the cardioid antenna system as the loop is rotated about a vertical axis. The necessary phasor diagrams are shown, and Figure IV-3 shows the phasor diagram for proper cardioid adjustment, with the loop oriented toward the station. Proper operation of the cardioid system is independent of the location of the whip with respect to the loop, so long as it is not an appreciable fraction of a wavelength away.

The radiation pattern of a properly-adjusted cardioid antenna system is sketched in Figure 6-5. Maximum response occurs with the plane of the loop antenna oriented parallel to the x-axis.

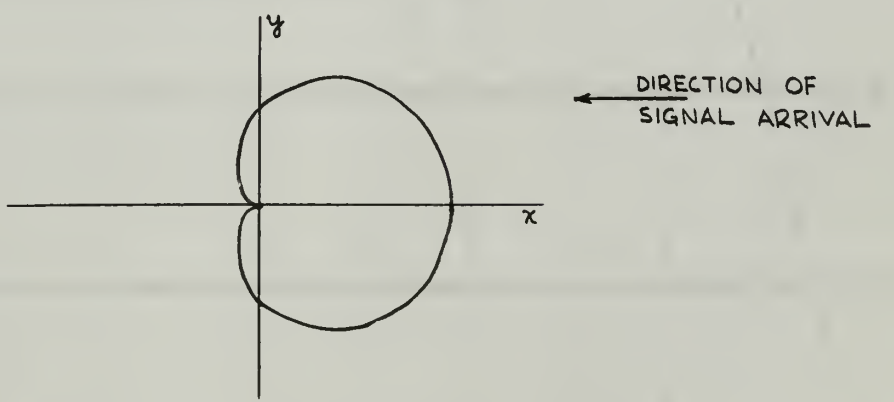

Figure 6-5. Cardioid Radiation Pattern

Figures 6-6 and 6-7 are plots of the radiation pattern in Cartesian coordinates, using equations derived in Appendix IV. The plot is for a frequency of 20 kHz and a square loop 1.635 m on a side. Rotation angle α is the angle between the normal to the loop and the

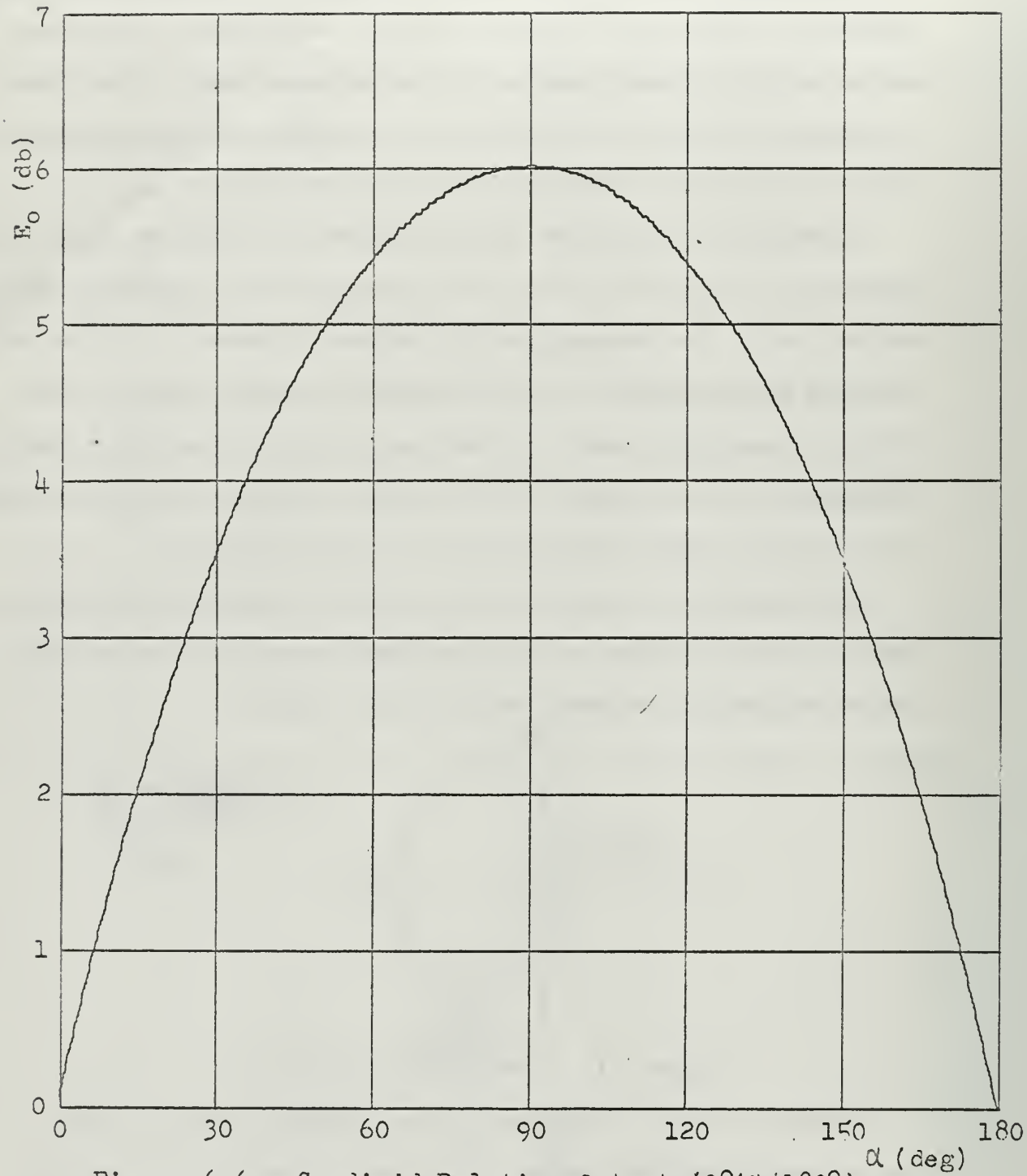

Figure 6-6. Cardioid Relative Output ($0° < \alpha < 180°$)

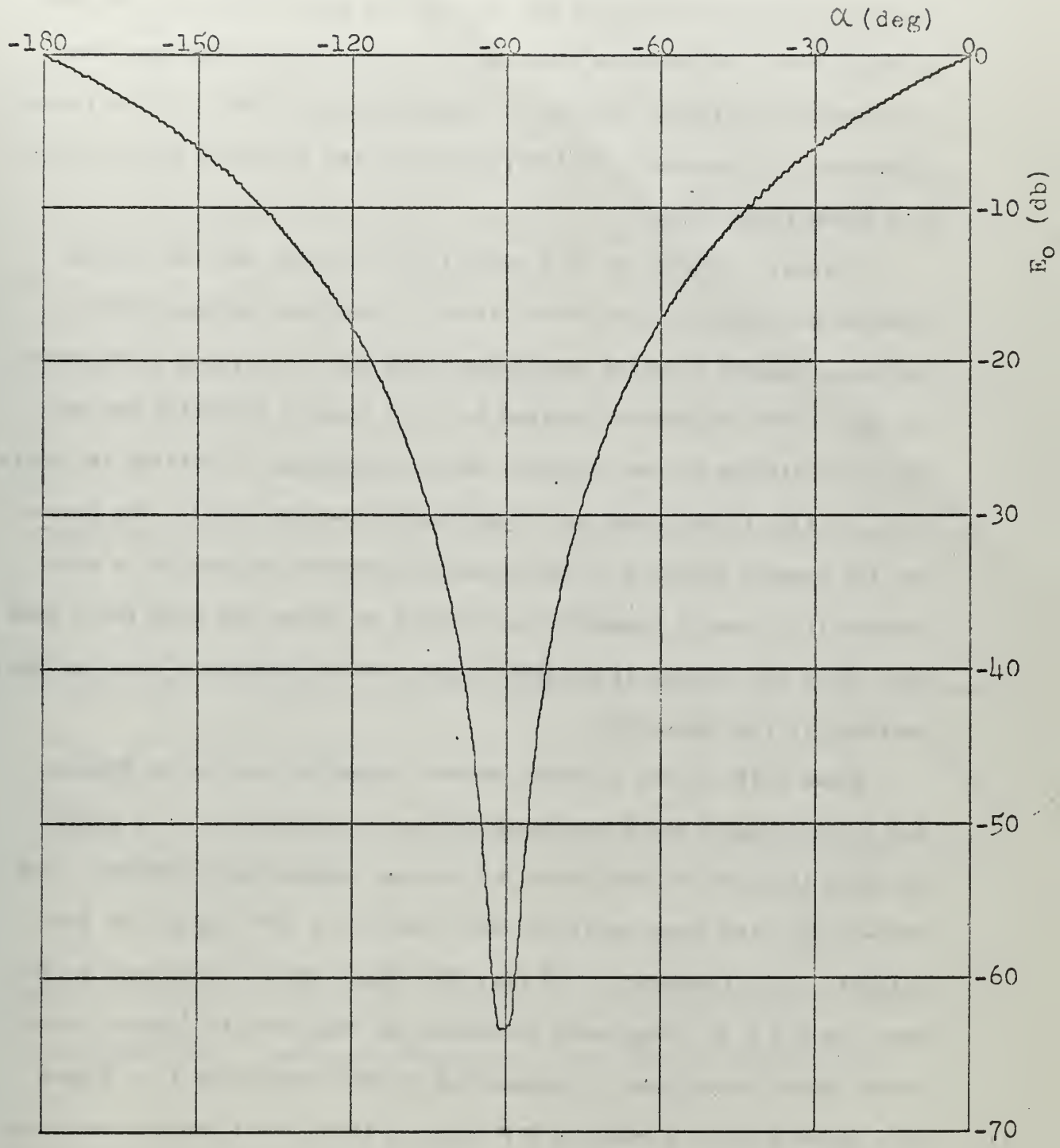

Figure 6-7. Cardioid Relative Output ($-180° < \alpha < 0°$)

positive x-axis. The maximum response is 6 db, which merely indicates that the voltage delivered to the receiver is twice that from the loop or whip alone. The minimum response, with the loop pointed away from the direction of signal arrival, is approximately -63 db. In the forward direction, 6 db beamwidth is 180^{o}, providing the desirable characteristic of a broad front lobe.

It should be noted at this point that -63 db is not the minimum response obtainable on the "back" side of a cardioid antenna system. The ideal minimum response approaches $-\infty$db when the system is adjusted for this. The adjustment required for this entails adjusting the whip phase for minimum system response, which corresponds to setting the angle of $\tilde{E}_s$ to $+\varphi_o$ rather than $-\varphi_o$ (see Figures IV-4 and IV-7). The reason for the present approach to the adjustment problem is that for a weak station it is nearly impossible accurately to adjust the whip for a good null while the antenna is pointed in the reverse direction; this has been verified in the laboratory.

Phase shift of the cardioid antenna system is plotted in Figures 6-8 and 6-9, again using equations derived in Appendix IV. It should be noted that the Υ-axis scales of the two figures are different. For $0^{o} < \alpha < 180^{o}$, the phase shifts no more than 0.3×10^{-2} deg as the loop rotates. At a frequency of 20 kHz, 360^{o} phase shift corresponds to 50 μsec, so 0.3×10^{-2} deg would correspond to less than 10^{-3} μsec; since normal phase variations of propagation produce changes of 1 or 2 μsec on a phase plot of a received VLF station, these small changes would not be noticeable.

An interesting aspect of Figure 6-9 is the phase change of -90^{o} in the vicinity of $\alpha = -90^{o}$. At 20 kHz, this would correspond to a phase

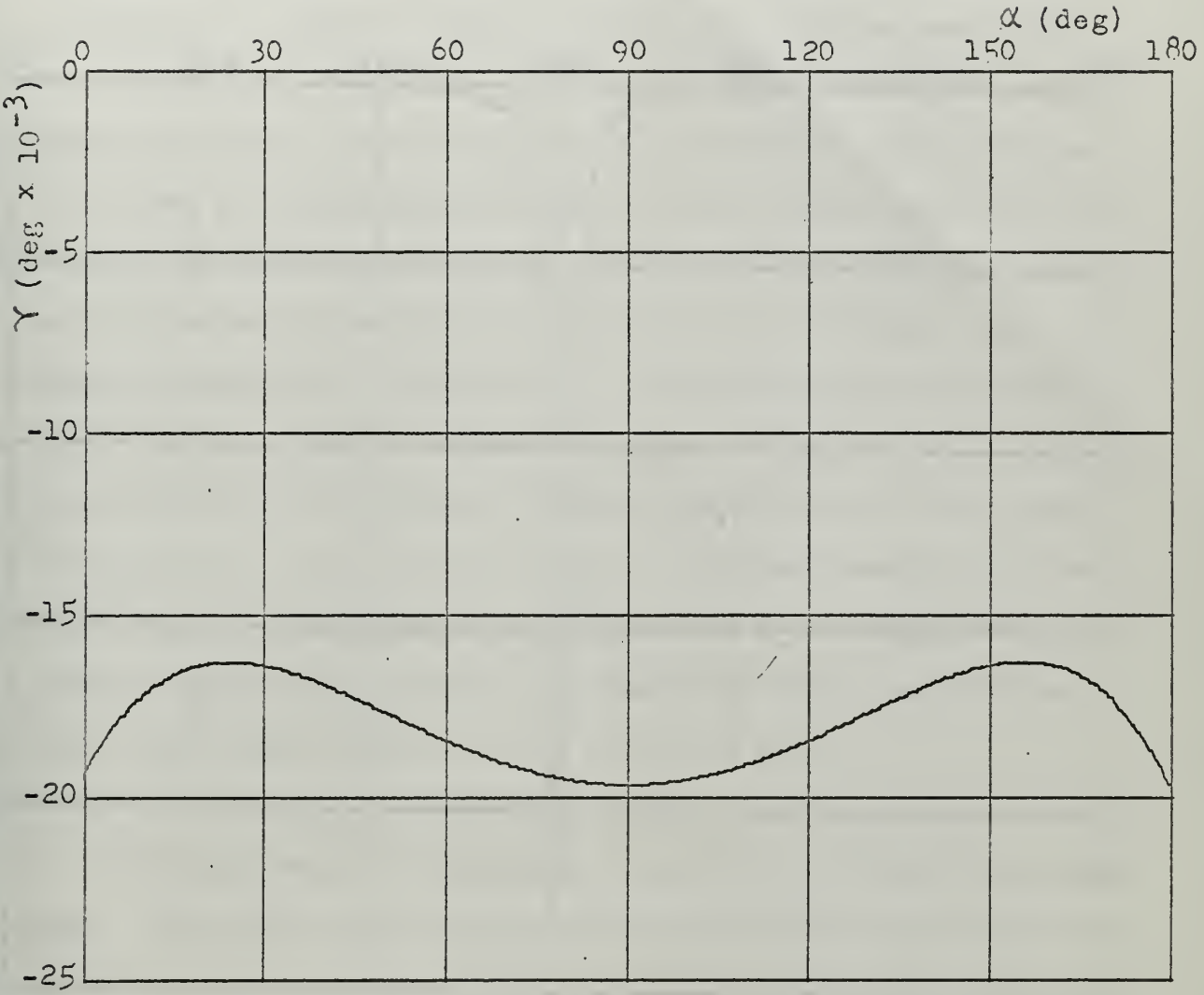

Figure 6-8. Cardioid Relative Phase Shift ($0° < \alpha < 180°$)

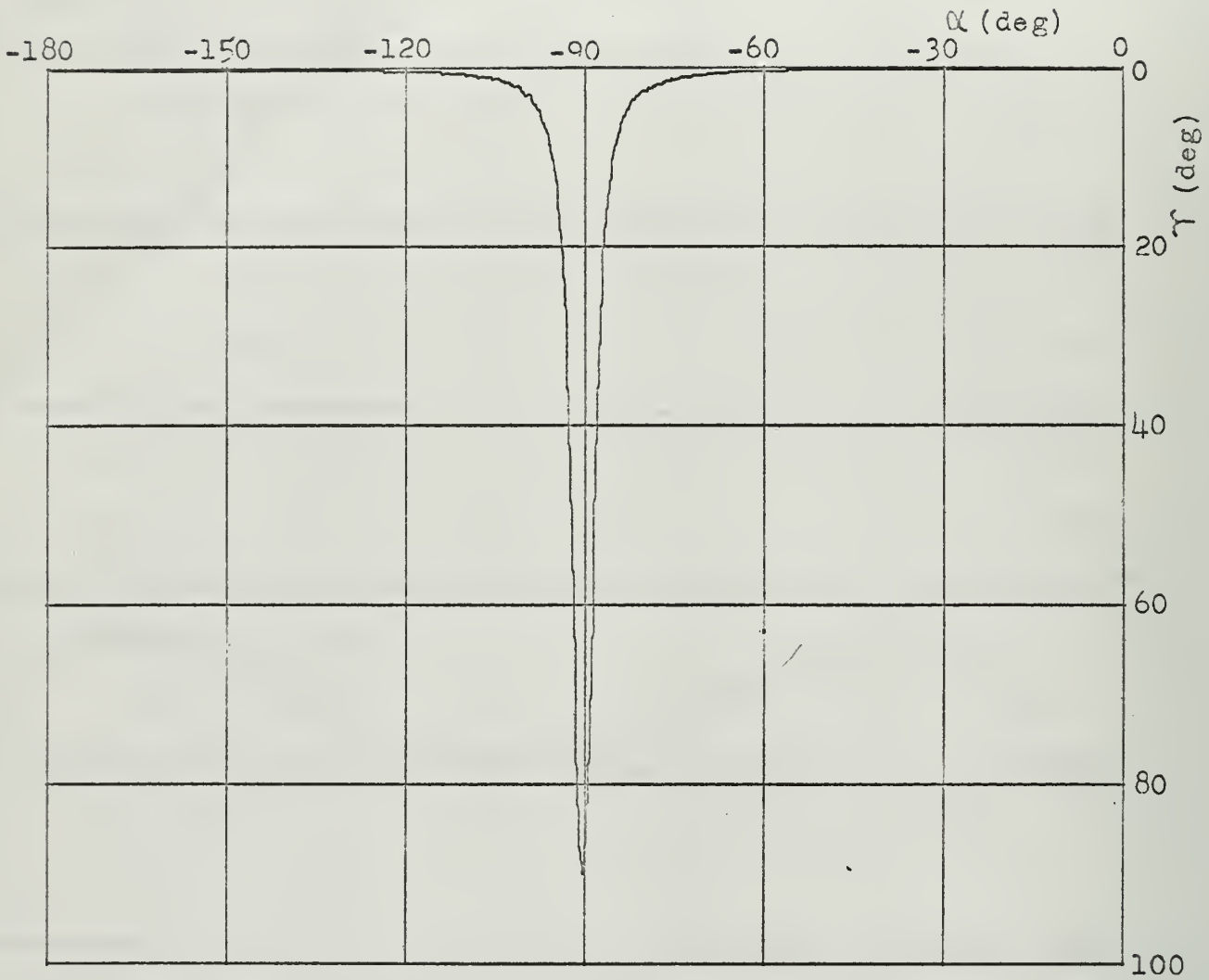

Figure 6-9. Cardioid Relative Phase Shift ($-180° < \alpha < 0°$)

change of 12.5 μsec. It should also be noted that, while there may appear to be a discontinuity at $\alpha = 0^{o}$ and $\alpha = \pm 180^{o}$, due to the difference in Υ-axis scales on Figures 6-8 and 6-9 this is not in fact the case.

Since it is proposed that a cardioid antenna system be used aboard ship in the VLF relative navigation system, there has been some concern that the sharp phase change in the vicinity of the cardioid null might cause difficulties. It is believed by the authors that this will cause no problems for the following reasons: (a) the relative broadness of the null, and (b) experimental evidence that the 90° phase shift in a typical cardioid system does not occur so abruptly as the theoretical curve of Figure 6-9 indicates. The latter will be discussed later in this section. The former is seen by examining Figure 6-7: if the loop is rotated 15° either side of the null, cardioid response is still down nearly 35 db from that of the forward direction. For these reasons, it is felt that no special measures would need to be taken aboard ship to keep the antenna aligned with the direction of the transmitting station, other than a simple servo system driven by the ship's gyro.

Experimental Work

The Tracor Model 611 Cardioid Unit was used at the Naval Postgraduate School. This unit has two inputs: one directly from a loop antenna, and the other from a whip antenna. Both antennas must be tuned as desired in the VLF band and matched to 50-ohm coaxial cable. The cardioid unit provides adjustable phase shift and amplification so that the cardioid pattern may be obtained at any frequency between about 9 kHz and 30 kHz. The output of the unit is switchable between cardioid, loop only, and whip only. Although the cardioid unit is specified to be usable with only particular types of Tracor antennas, it was found to be usable with

an 18-foot whip antenna that happened to be on hand and a tuning network designed for 20 kHz. The complete cardioid system manufactured by Tracor comes with a remotely-tuned rotatable loop antenna and a whip antenna with fixed tuning. This system was used to obtain data presented below.

Radiation patterns for the cardioid system were obtained using WWVL at 20 kHz. The length of a side of the square loop was 1.635 m, so data is directly comparable with the theoretical patterns of Figures 6-6, 6-7, 6-8, and 6-9. The system was adjusted by setting whip amplitude and phase equal to that of the loop with the loop oriented toward Ft. Collins, Colorado (the location of WWVL). It would have been preferable to set up a nearby low-powered (milli-watt or micro-watt) phase-stabilized transmitter to assure steady signal levels while the antenna was rotated, but this was not practicable.

The amplitude data obtained is shown in Figure 6-10. Azimuth of 0^{o} corresponds approximately to orientation toward the transmitting station. The numbers in parentheses below the abscissa correspond to angle of rotation α. Due to difficulty in reading the rotator unit, relative azimuth accuracy is probably $\pm 3^{o}$. Relative amplitude is accurate to better than ± 1 db. The two major sources of error here are variations in the received carrier level of WWVL and calibration of the receiver carrier level recorder output.

It is interesting to compare Figure 6-10 with Figures 6-6 and 6-7. Considering that real antennas never perform quite so well as ideal ones, the similarity is striking. Overall, the null is somewhat broader than the theoretical; for example, the output is 35 db down at about 22^{o} either side of the null. The 6 db beamwidth is 181^{o}, which is the same as the

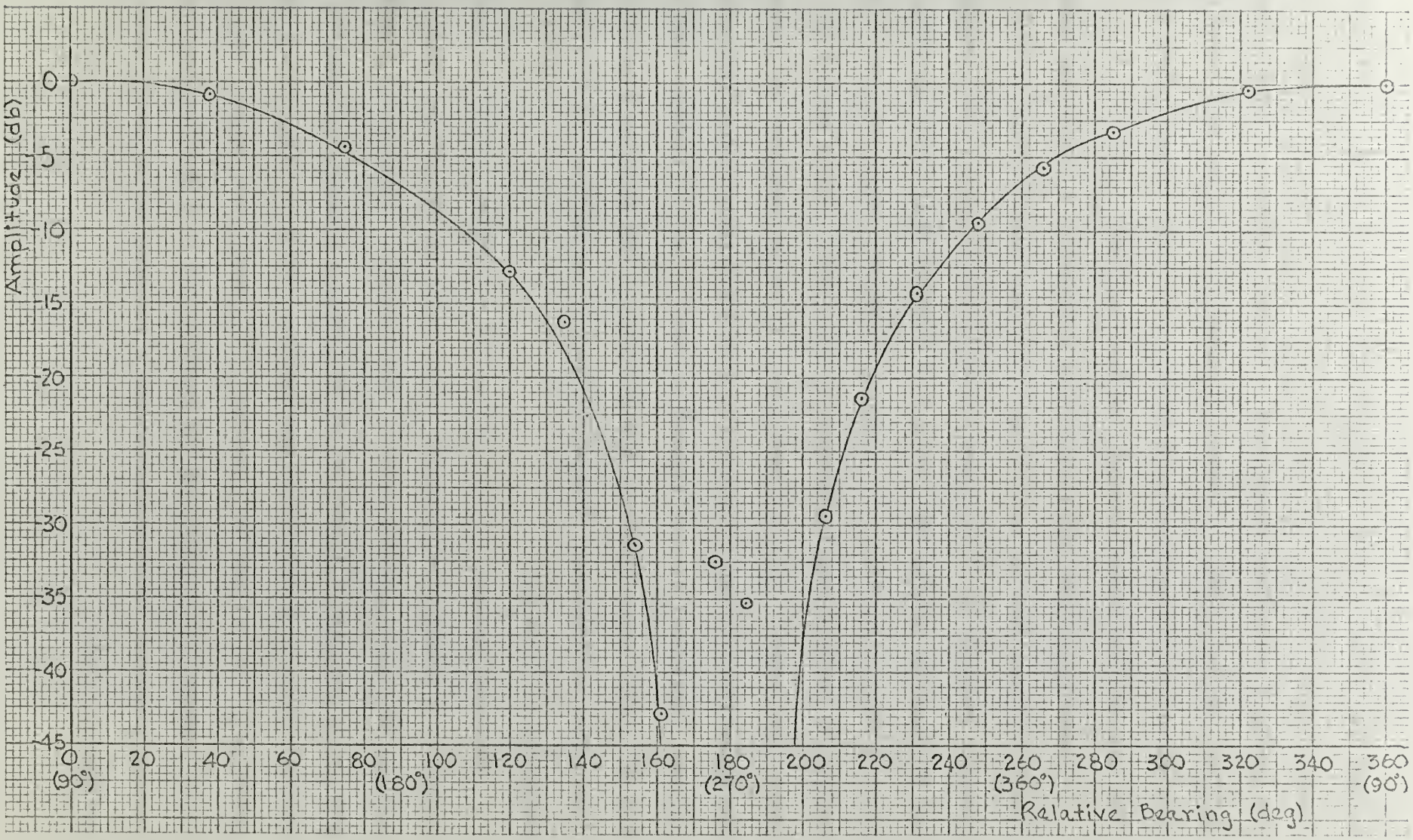

Figure 6-10. Cardioid Amplitude

theoretical value, within the experimental error. The two points appearing within the null at amplitudes of -32.5 db and -35.4 db indicate that the cardioid system was misadjusted, with whip amplitude slightly greater than loop amplitude. A careful examination of Figure IV-7 shows that this would also cause phase excursion to be slightly greater than $\lambda/4$. This was verified experimentally, as seen in Figure 6-11.

Figure 6-11 shows phase shift data obtained as the loop was rotated. The τ = 0 μsec line is an arbitrary reference level. Phase data is probably accurate to $\pm$1 or 2 μsec, considering accuracy of the receiver and propagation changes that could have occurred while data was being taken. The smaller figure is probably acceptable, since data was taken during the daytime when the ionosphere was stable, over a period of about three hours. Angle of rotation α is again indicated in parentheses below the abscissa. The most notable difference between this curve and the theoretical data of Figures 6-8 and 6-9 is the broader width of the 90^{o} ($\lambda/4$) phase change in the vicinity of the null, as noted earlier. The rubidium vapor frequency standard was used as the local phase reference for this data.

There are various problems associated with using a cardioid antenna system in a shipboard environment. One is the problem of re-radiators located near the loop-whip system. This presents a problem in a receiving system because of distortion of the antenna pattern, principally by resonant lengths of metal near the antenna. Unfortunately, it was not possible to investigate this problem at the Naval Postgraduate School. It is, however, the opinion of the authors that this problem would not seriously degrade the cardioid antenna's performance in the VLF relative navigation system.

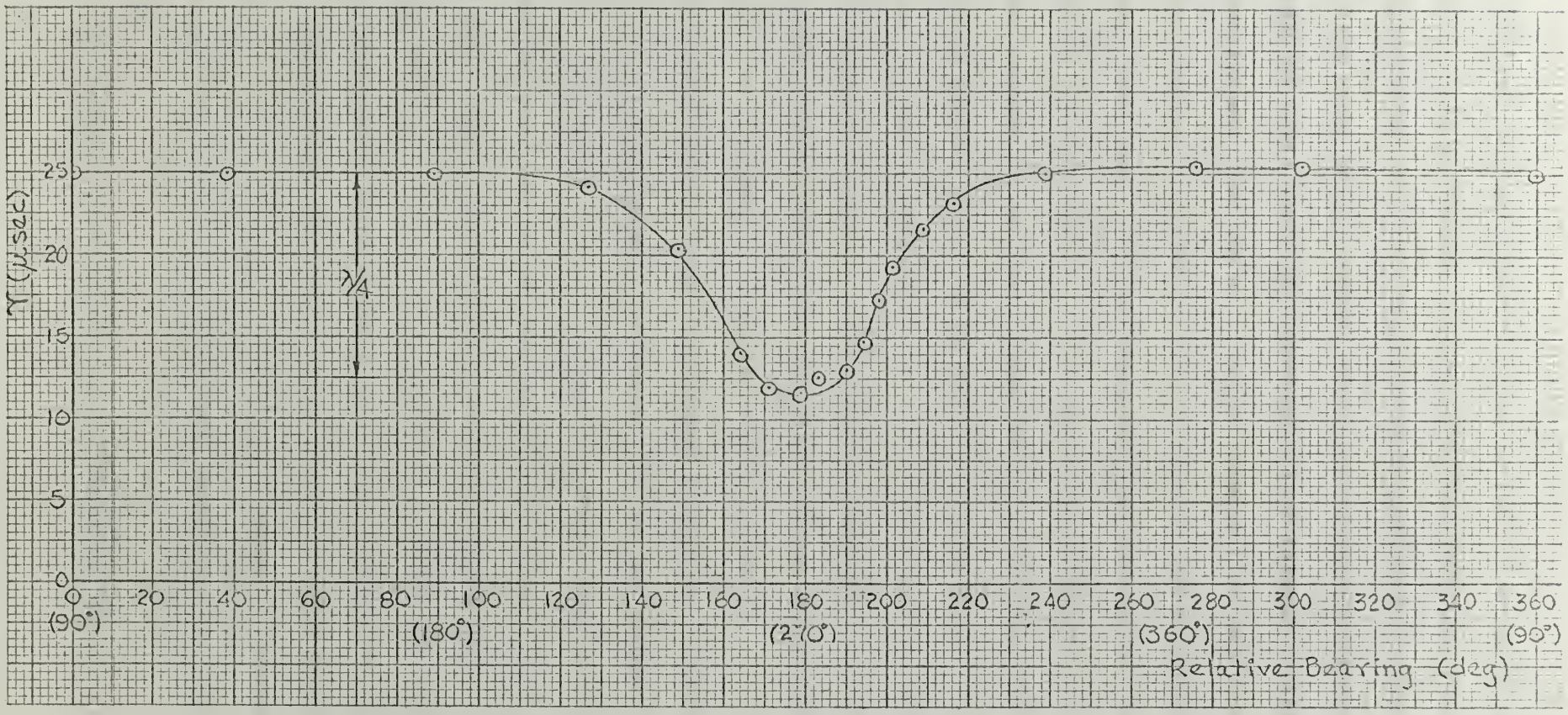

Figure 6-11. Cardioid Phase

Another problem is that of properly adjusting the cardioid unit. Whip phase and amplitude must be carefully matched to that of the loop at each frequency used, in order to obtain a true cardioid pattern. This may be difficult for distant stations whose long and short path signals are comparable. Careful attention should be given these adjustments, since depth of the null depends directly on how well the system is adjusted.

7. Determination of Signal Strengths

In this section values will be calculated for the relative strengths of signals received via the long and short great circle paths as a function of the time of day and day of the year. This, along with the phase of both signals, is necessary in order to calculate the phase of the resultant signal.

The relative strengths of the two signals can be found at any point on earth if the total attenuation on each path is known. The relative strength of the two signals is then just the difference of the short and long path attenuations. Upon reexamination of the electric field strength equation in Section 2 it will be seen that an assumption is being made here that all terms except the last two in this equation are identical for both propagation paths. It seems only reasonable to assume that most VLF stations have a symmetrical radiation pattern and that the amount of excitation in two opposite directions will be equal.

Attenuation rates at VLF, mentioned in Section 2, vary from about one to five db/Mm depending on the time of day and propagation path conditions. References 5, 8, 9, 18, and 28 contain many of the curves of attenuation rates versus frequency which have been derived from experimental data. These curves will be used extensively here.

The procedure used to obtain expected attenuation rates at any particular frequency consists simply of sifting through the data present in these references and extracting the attenuation rates given for different conditions at this frequency. From this information estimates of the attenuation rates for all possible path conditions and times of day can be made.

As an example, at 13.6 kHz the following values are given in the

references stated.

α (db/Mm)	conditions	reference
3.6	land, day, east to west	Taylor [9] pg. 1933
2.8	sea, day, east to west	Taylor [9] pg. 1933
2.6	day	Chapman and Macario [5] pg. 930
2.0	sea, night, east to west	Taylor and Lange [8] pg. 609
1.8	day, sea, west to east	Taylor [9] pg. 1933
1.6	night	Chapman and Macario [5] pg. 930
3.5	sea, day, east to west	Watt and Croghan [18]
2.35	sea, day, north to south	Watt and Croghan [18]
1.95	sea, day, west to east	Watt and Croghan [18]
1.3	night, sea	Watt and Croghan [18]
1.0	sea, night, west to east, 15-20 kHz	Davies [28] pg. 425
$\Delta\alpha$ = 1.0 to 1.5	sea to land change, 15-20 kHz	Davies [28] pg. 425
$\Delta\alpha$ = 1.0	night to day change, 15-20 kHz	Davies [28] pg. 425
$\Delta\alpha$ = 1.0	W-E to E-W change, 15-20 kHz	Davies [28] pg. 425

From these attenuation rates (and changes in attenuation rates) and other discussions of attenuation rates such as those by Crombie [7] and Westfall [21] reasonable estimates of attenuation rates for 13.6 kHz can be made. These will be in the form of one basic attenuation rate plus additional factors which depend on the direction of propagation, amount of daylight on the path and amount of land on the path.

The values chosen are:

α_b = 1.0 db/Mm		basic rate (night, sea, W-E)
$\Delta\alpha_{n-d}$ = 1.0 db/Mm		night to day change
$\Delta\alpha_{s-l}$ = 0.8 db/Mm		sea to land change (average land)
$\Delta\alpha_{dN-S}$ = 0.4 db/Mm		W-E to N-S direction change
$\Delta\alpha_{dE-W}$ = 1.55 db/Mm		W-E to E-W direction change

The change in attenuation rate as a function of direction can be approximated by:

$$\Delta\alpha_d(\phi) = \left(\frac{1.26\,\phi}{180^o}\right)^2$$

where ϕ is the direction of propagation with respect to 090° true ($0 \leq \phi \leq 180^o$). For north to south propagation $\phi = 90^o$ and for east to west propagation $\phi = 180^o$.

The attenuation rate over any path can be calculated from the following equation:

$$\alpha = \alpha_b + P_D\Delta\alpha_{n-d} + P_L\Delta\alpha_{s-l} + \Delta\alpha_d(\phi)$$

where P_D = fraction of the path which is in daylight

P_L = fraction of the path which is over land.

A typical plot of attenuation for a 24 hour period is shown in Figure 7-1. The path here is Trinidad to Monterey (short path); ϕ = 145°, P_L = 0.6 and P_D is obtained from the computer program described in Appendix II. The total attenuation is found by multiplying α by the path length obtained from the geodesic program (Appendix I). The calculated attenuation rates vary from 2.48 db/Mm for the entire path in darkness to 3.48 db/Mm for the all-daylight path.

Figure 7-2 shows a comparison of the long and short path attenuation from Trinidad to Monterey. The long path here is considered to be in the opposite direction at the receiver and transmitter from the short

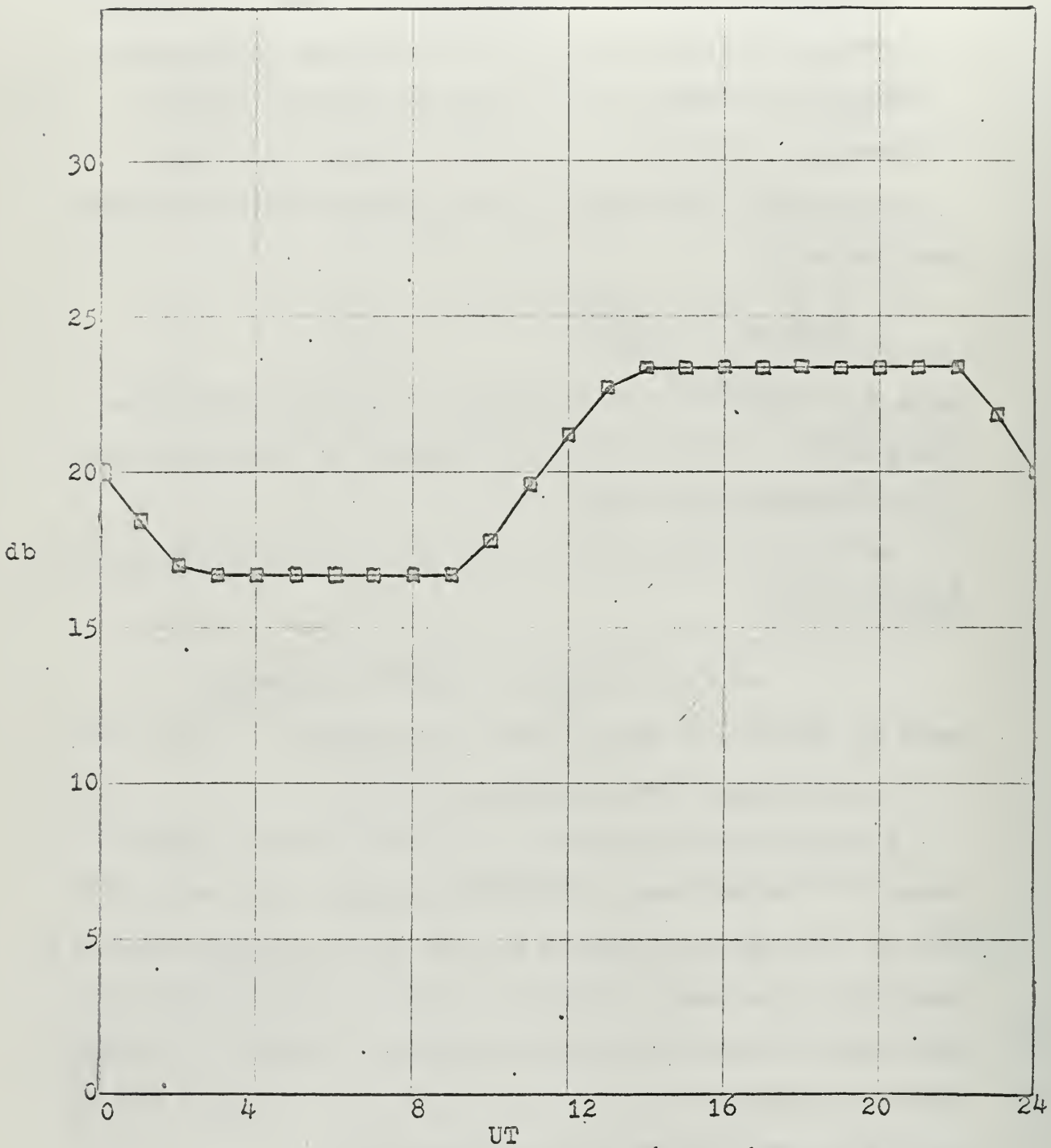

Figure 7-1. Calculated attenuation of 13.6 kHz signal on Trinidad to Monterey short path for 1 Oct. 1966
Path length = 6658.85 km
Min. = 16.72 db
Max.=23.37 db

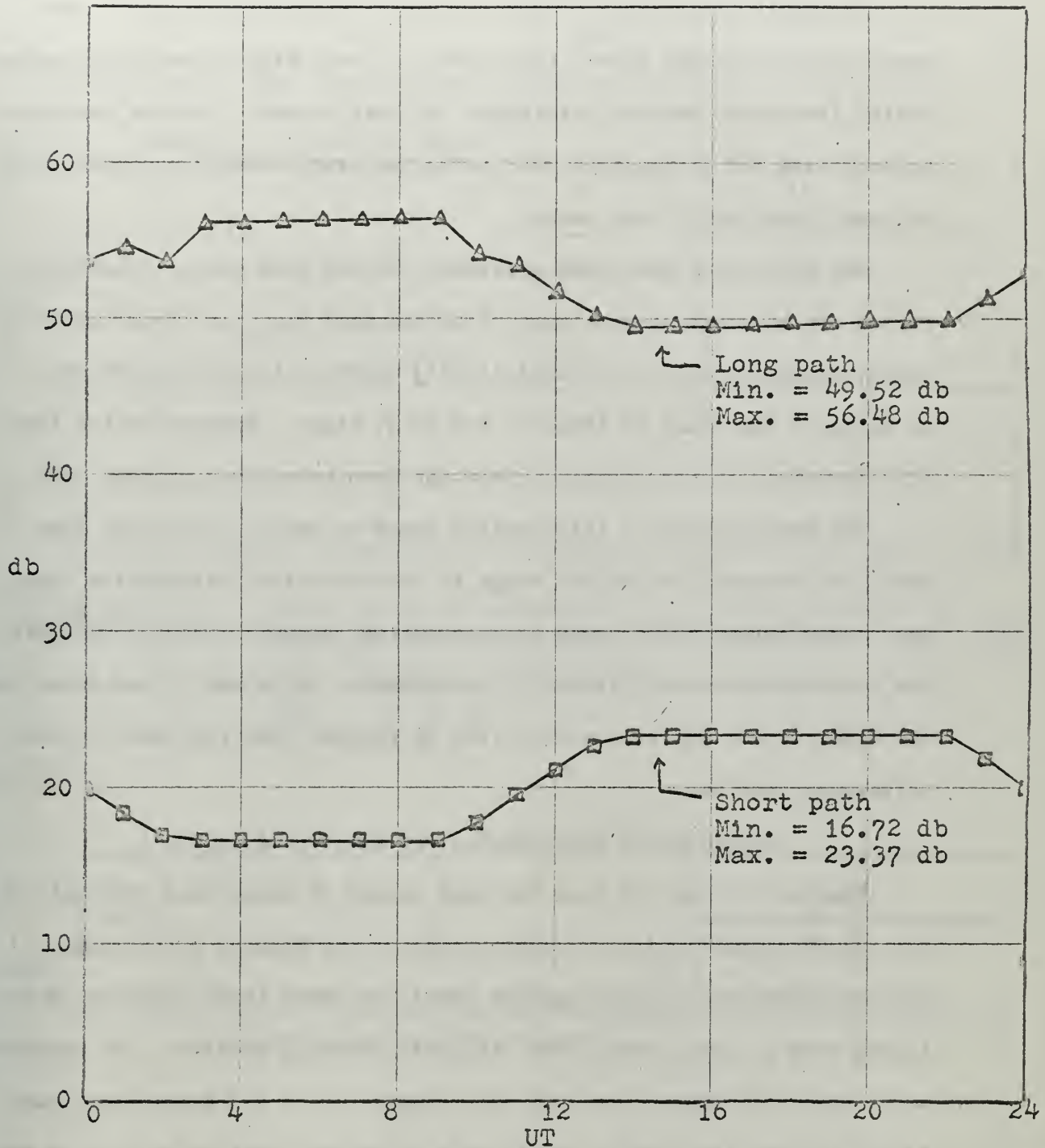

Figure 7-2. Calculated attenuation of 13.6 kHz signal on Trinidad to Monterey long and short paths for 1 Oct. 1966
Short path length = 6658.85 km
Long path length = 33391.48 km

path direction of propagation.

It should be noted that the attenuation rates used here for land paths are for average land. Large areas of very high or very low conductivity land would require alteration of these values. Similar care must be exercised for propagation over polar ice caps, where the conductivity is lower than that of sea water.

One factor not mentioned previously is the loss due to discontinuities of the earth conductivity along the path ($L_{d,n}$ in the electric field strength equation). Westfall [21] mentions this factor briefly as having a magnitude of three to six db at times. Because of the lack of information on this factor it has not been taken into account here.

The method shown in this section could be used at any other frequency of interest in the VLF range to obtain similar attenuation rates. Some complicating factors may be encountered, however, which could make the calculations more difficult. For example, at 16 kHz it was found that the night to day difference over land is greater than the night to day difference over sea.

Comparison of Experimental and Calculated Values

Figures 7-3 and 7-4 show two more curves of calculated attenuation for the Forestport and Haiku Omega stations and Figures 7-5 through 7-7 show the observed relative carrier levels of these three stations as obtained from a Tracor Model 599G VLF phase tracking receiver. No measurements were obtained on any long path signals or on the Aldra short path signal because the carrier levels were below the level of control of the receiver AGC, giving a reading of zero on the relative carrier level output.

Since no attempt was made to calculate the signal strength of the

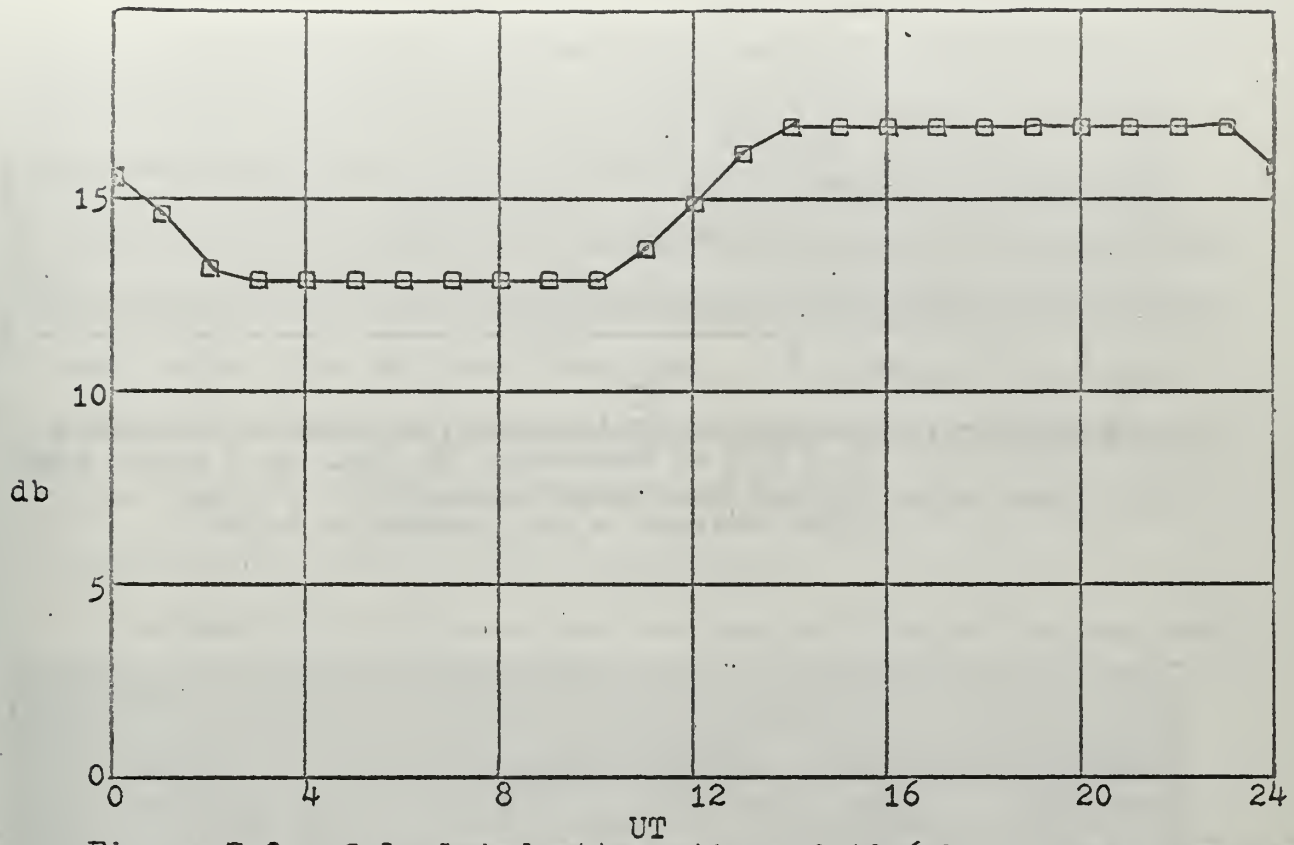

Figure 7-3. Calculated attenuation of 13.6 kHz signal on Forestport to Monterey short path for 1 Oct. 1966
Path length = 4011.74 km
Min. = 12.90 db
Max. = 16.91 db

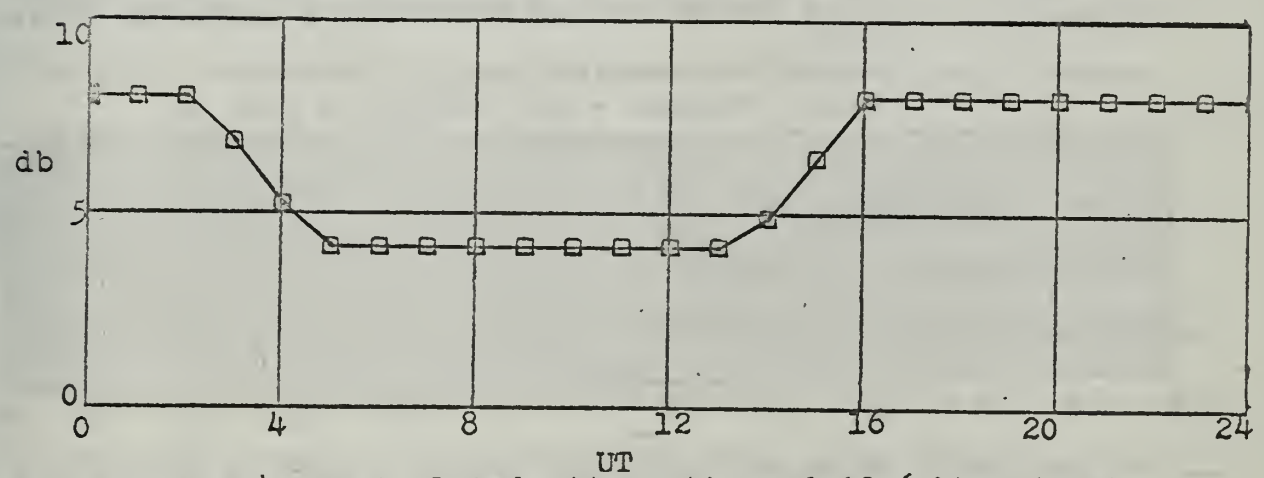

Figure 7-4. Calculated attenuation of 13.6 kHz signal on Haiku to Monterey short path for 1 Oct. 1966
Path length = 3856.50 km
Min. = 4.16 db
Max. = 8.02 db

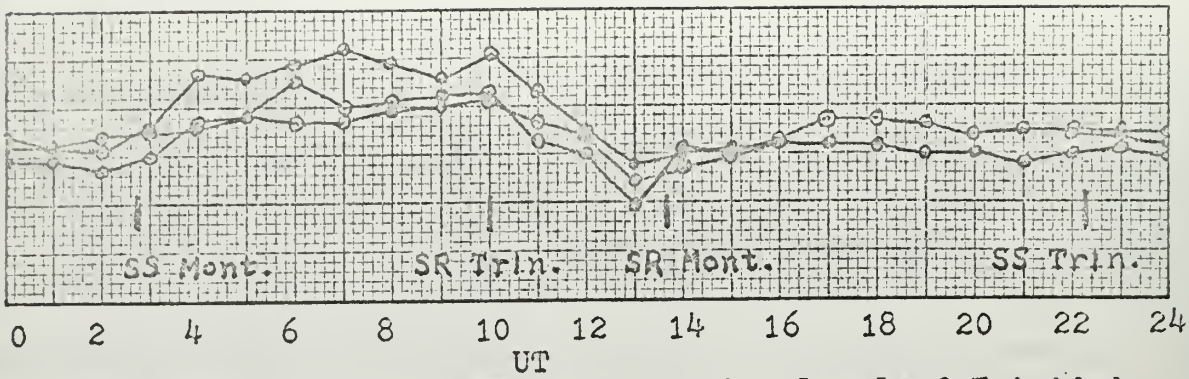

Figure 7-5. Observed relative carrier level of Trinidad 13.6 kHz at Monterey, 30 Aug. to 2 Sept. 1966
10 db/½ in. vertical scale
night average - day average = 4.04 db

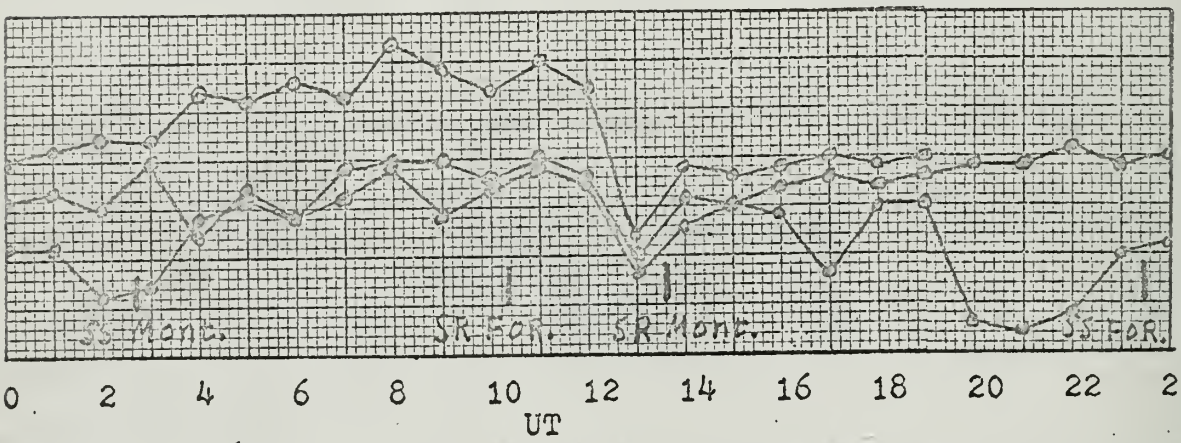

Figure 7-6. Observed relative carrier level of Forestport 13.6 kHz signal at Monterey, 5 Sept. to 8 Sept. 1966.
10 db/in. vertical scale
night average - day average = 2.47 db

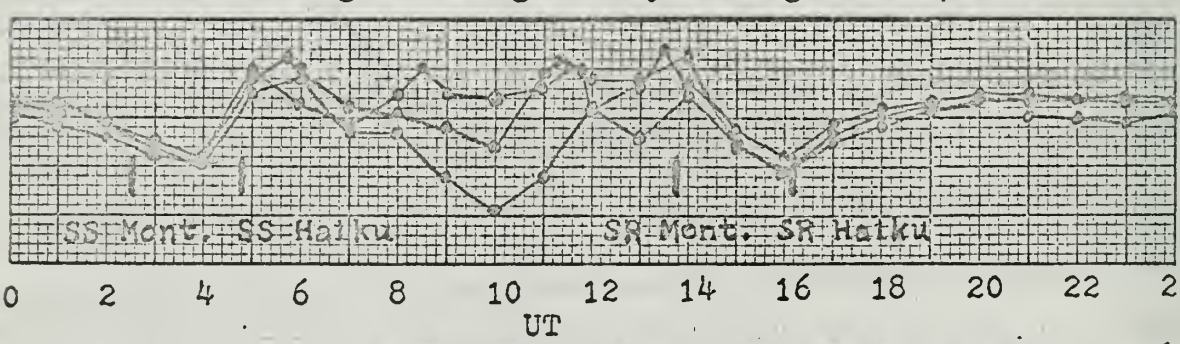

Figure 7-7. Observed relative carrier level of Haiku 13.6 kHz signal at Monterey, 2 Sept. to 5 Sept. 1966
10 db/½ in. vertical scale
night average - day average = 0.3 db

various stations and this information is not readily obtainable from the Tracor receivers, the only quantities that can be compared meaningfully are the difference between the carrier levels for the entire path in darkness and in daylight and the day-night attenuation difference. While the attenuation decreases at night and the carrier level increases during the same period the difference between the day and night values should be equal since they are complementary quantities. (This is easily seen in the electric field strength equation of Section 2 where $\alpha d/10^6$ is the attenuation and $E_{z,n}$ is the carrier level.)

A comparison of the calculated and observed values of the night-day difference is shown below.

Station	Calculated difference	Observed difference (a)	Observed difference (b)
Trinidad	6.65 db	4.04	6.4 db
Forestport	4.01 db	2.37	7.5 db
Haiku	3.86 db	0.3	4.5 db

The values listed under (a) were observed with the receiver servo time constant set at 150 seconds and those under (b) with a 15 second time constant. The lower differences observed with the 150 second time constant, corresponding to Figures 7-5 and 7-7 are apparently because of the erratic nature of nighttime phase.

Calibration of the signal level scale used on the recorder was very difficult, leading to some possible inaccuracies in these measurements. (Calibration was complicated by the short duty cycle of the transmitting stations; 10%.) Thus while these measurements do provide some measure of confidence in the calculated attenuation rates, it is believed that more comprehensive measurements of the carrier levels of these signals would be necessary if an accurate check of these attenuation rates was desired.

8. Calculation of VLF Phase Velocities

Figures 2-8 through 2-11 show several curves of calculated phase velocities for VLF signals for different conditions which could be used directly to obtain the desired phase velocities. However, it would be more convenient and accurate to make use of an equation for phase velocity which takes into account the frequency and conditions of the ionosphere and the earth. Such an equation is available in the Omega System book [31], page 3-20:

$$\frac{V_p}{V_o} = 1 - 0.36\,\frac{h_i}{a} + \left[(2\pi n - \varphi_g - \varphi_i)\,\frac{V_o}{4\pi\sqrt{2}\,f h_i}\right]^2$$

Here V_p = phase velocity of the VLF signal

V_o = free space velocity of the wave

= 3×10^8 m/sec

0.36 = a constant chosen to give a good fit in the 10-20 kHz frequency range

h_i = ionospheric height for which the conductivity (σ) = 10^{-6} mhos/m

a = radius of the earth = 6378.155 km

φ_g = phase shift upon reflection at the ground

φ_i = phase shift upon reflection at the ionosphere

n = mode number (= 1 for primary mode)

f = frequency

Some values are given for the phase shifts that can be expected; φ_i = -160° for daytime propagation, -165° at night, -165° for daytime propagation to the east, and -155° for daytime propagation to the west. Assuming that the -160° phase shift is for north-south propagation, which seems reasonable, the values for nighttime propagation to the east and west would then be -170° and -160° respectively. The ground phase shift

is zero for sea water and the values given for land are -0.09 radians during the day and -0.13 radians at night, for a ground conductivity of 10^{-2} mhos/m.

Using the given ionospheric heights of 68 km during the day and 86 km at night (derived from an exponential conductivity profile and taking the height for which $\sigma = 10^{-6}$ mhos/m) the phase velocity curves of Figure 8-1 were calculated. A comparison of these curves with similar curves in Section 2 (Figures 2-9, 2-10, 2-11) shows a very close correspondence. Several experimental phase velocities from Figure 2-14 are also plotted here for further comparison.

The phase velocity at any point along a path is:

$$V_p(x) = \frac{2\pi f}{d\theta/dx}$$

where θ is the phase in radians at the point x on the path. The total phase along the path is then:

$$\theta = 2\pi f \int_o^d \frac{dx}{V_p(x)}$$

If the phase velocity is constant this becomes:

$$\theta = \frac{2\pi fd}{V_p}$$

Using a method similar to that employed in determining the path attenuations of Section 7, an average phase velocity can be obtained for each path. It can be calculated by the following equation:

$$V_p = V_{pb} + \Delta V_{pd}(\phi) + P_D \Delta V_{pN-D} + P_S \Delta V_{pl-s}$$

where V_{pb} = basic phase velocity; phase velocity for night, land, W-E from Figure 8-1.

$\Delta V_{pd}(\phi)$ = increase in phase velocity due to direction of propagation.

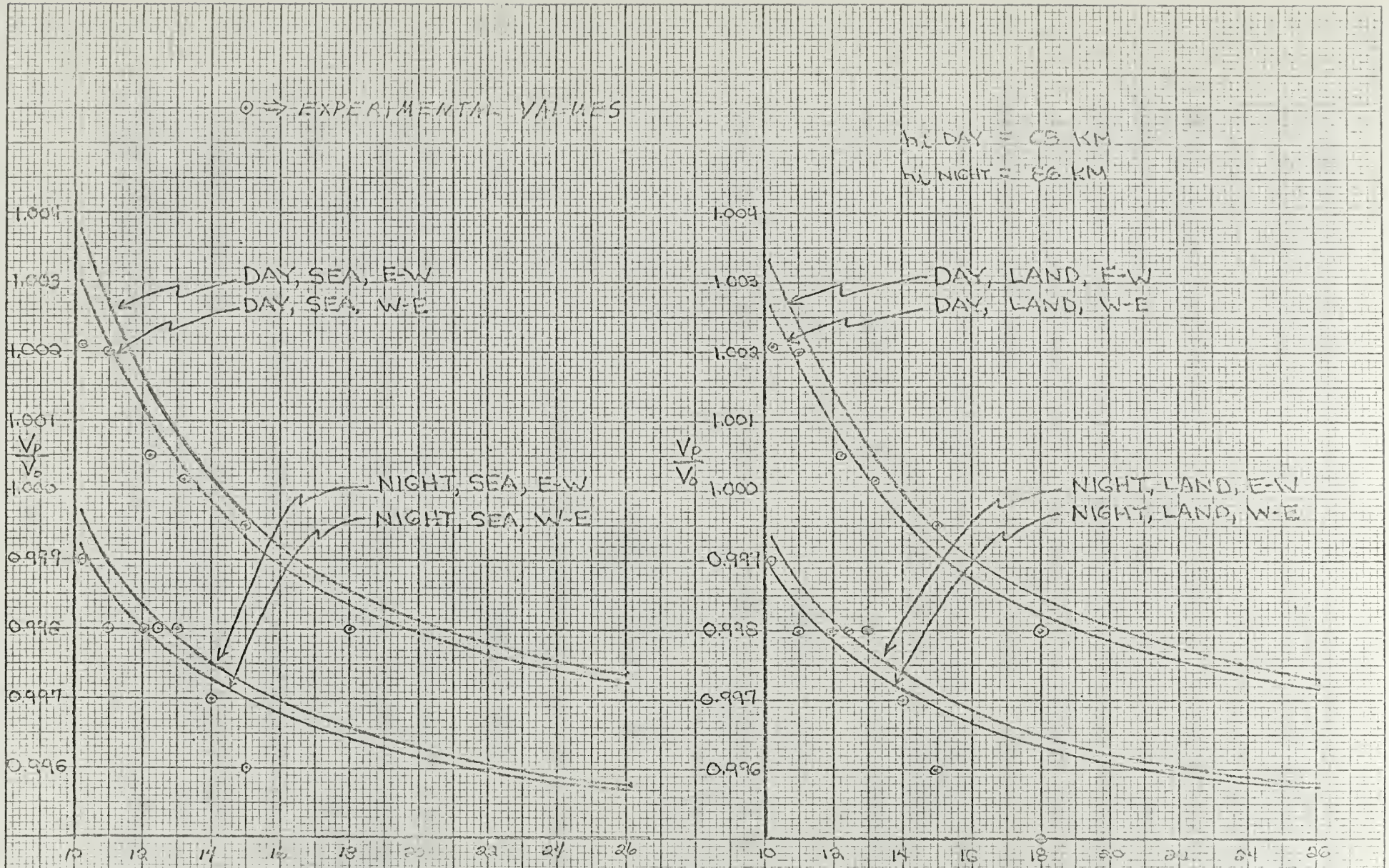

FIGURE 8-1. CALCULATED PHASE VELOCITY CURVES

P_D = proportion of path in daylight.

ΔV_{pN-D} = increase in phase velocity for daylight propagation.

P_S = proportion of path over sea.

ΔV_{pl-s} = increase in phase velocity for propagation over sea.

The increase in phase velocity with direction can be obtained from the following equation:

$$\Delta V_{pd}(\phi) = \Delta V_{pd} \frac{\phi}{180^o}$$

where ϕ is the direction of propagation, measured as in Section 7. From Figure 8-1, the differences between the phase velocities for E-W and W-E propagation are different for daytime and nighttime propagation. ΔV_{pd} for daytime can be approximated by the average daytime differences in phase velocity with direction and the nighttime value can be obtained similarly. This can be expressed by the following equations:

$$\Delta V_{pd} = \tfrac{1}{2}(V_{psDEW} - V_{psDWE} + V_{plDEW} - V_{plDWE}) \text{ daytime}$$

$$\Delta V_{pd} = \tfrac{1}{2}(V_{psNEW} - V_{psNWE} + V_{plNEW} - V_{plNWE}) \text{nighttime}$$

Here V_{psDEW} = phase velocity for sea, day, E-W

V_{plNWE} = phase velocity for land, night, W-E and so on.

Using reasoning similar to the above it is found that two values for ΔV_{pN-D} must be used (one for E-W propagation and one for W-E) and one value for ΔV_{pl-s} can be used. These are given by the following equations:

$$\Delta V_{pN-D} = \tfrac{1}{2}(V_{psDWE} - V_{psNWE} + V_{plDWE} - V_{plNWE}), \text{ W-E}$$

$$\Delta V_{pN-D} = \tfrac{1}{2}(V_{psDEW} - V_{psNEW} + V_{plDEW} - V_{plNEW}), \text{ E-W}$$

$$\Delta V_{pl-s} = \tfrac{1}{4}(V_{psDWE} - V_{plDWE} + V_{psDEW} - V_{plDEW}$$

$$+ V_{psNWE} - V_{plNWE} + V_{psNEW} - V_{plNEW})$$

The range of the phase velocity changes being averaged to obtain ΔV_{pl-s} is about $4 \times 10^{-5}\ V_p/V_o$. The range of phase velocity changes being averaged for ΔV_{pN-D} and ΔV_{pd} is smaller, indicating that the error in ΔV_{pl-s} is the largest that would be encountered.

The curve shown in Figure 8-2 is a typical 24 hour plot of phase delay calculated by the above method. This is for the Trinidad to Monterey short path with the same parameters as used in Section 7 (ϕ = 145°, P_s = 0.4, P_D from computer program of Appendix II). The 13.6 kHz phase velocities used to calculate this curve are listed below.

$$V_{psDWE} = 1.0000213V_o$$
$$V_{psDEW} = 1.0004273V_o$$
$$V_{psNWE} = 0.9974367V_o$$
$$V_{psNEW} = 0.9976842V_o$$
$$V_{plDWE} = 0.9998199V_o$$
$$V_{plDEW} = 1.0002154V_o$$
$$V_{plNWE} = 0.9972606V_o$$
$$V_{plNEW} = 0.9974986V_o$$

Comparison of Experimental and Calculated Phase Delays

Figures 8-3 through 8-6 show both calculated and observed 24 hour phase delay curves. The average of the observed daily curves is shown shifted by 1.5 inches (15 or 30 μsec) for convenience and ease of comparison with the calculated curves. The total phase delay of the signal from transmitter to receiver is not easily obtained experimentally; thus only the day-to-day changes in the phase delay are compared here.

Figures 8-5 and 8-6 show a very close correspondence between calcu-

lated and observed curves. It is interesting to note that there appears to be a time lag in the observed phase delay during periods of rapid change, which could be due to the long time constant used in the receiver (150 sec). The lag also seems more pronounced on stations with lower signal strengths at the receiver.

Figure 8-4 shows differences in the calculated and observed curves which seem to point towards some error in the calculations. The amplitude and shape of the observed diurnal shift are believed to be approximately correct.

Figure 8-3 is a good example of a diurnal shift that is not a trapezium. Propagation over a polar path, as is the case here, yields diurnal shifts similar to those shown in Figure 8-7, and are markedly different during different times of the year. The diurnal shift on polar paths is discussed more thoroughly by Blackband [12]. In Figure 8-3 the poor correlation of the calculated and observed curves may be partially due to the weak signal strength of the Aldra station at Monterey. The phase-tracking receiver did not seem to "lock on" to the received phase until a large change in phase delay occurred, such as encountered during sunset along the path. This can be seen during the initial portion of the readings, started at 1900 on 23 September.

Figure 8-8 shows a comparison of an experimental phase velocity curve, obtained by Thompson et al [14] in Sydney, Australia at 16 kHz, with a calculated curve. The data used for the calculated curve is approximate (position of the receiver, proportion of land on the path, etc.) and in view of this the close correspondence of these two curves is remarkable.

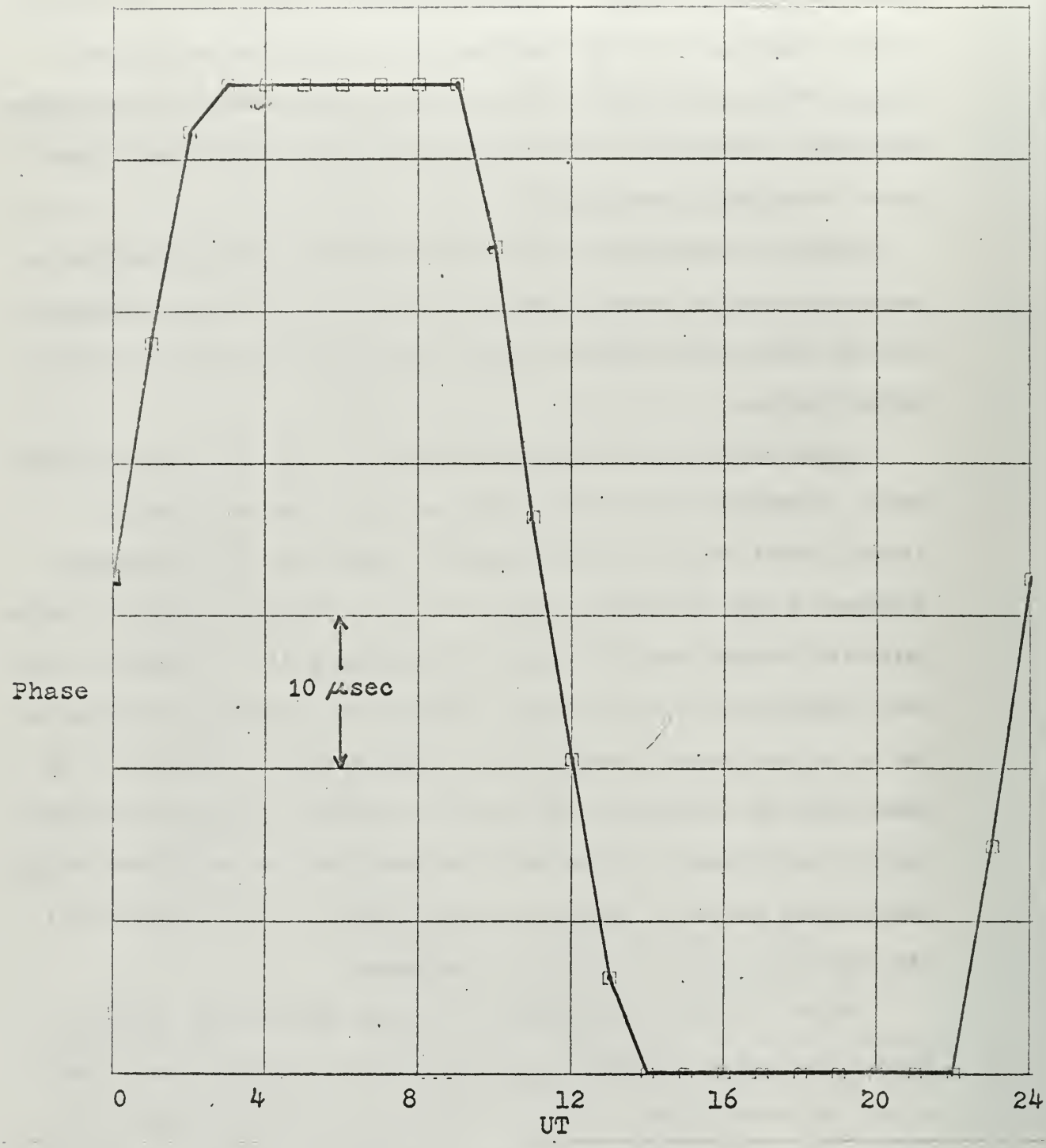

Figure 8-2. Calculated phase delay on Trinidad to Monterey short path at 13.6 kHz.
Minimum value is 22195.759 μsec delay
10μsec/inch vertical scale

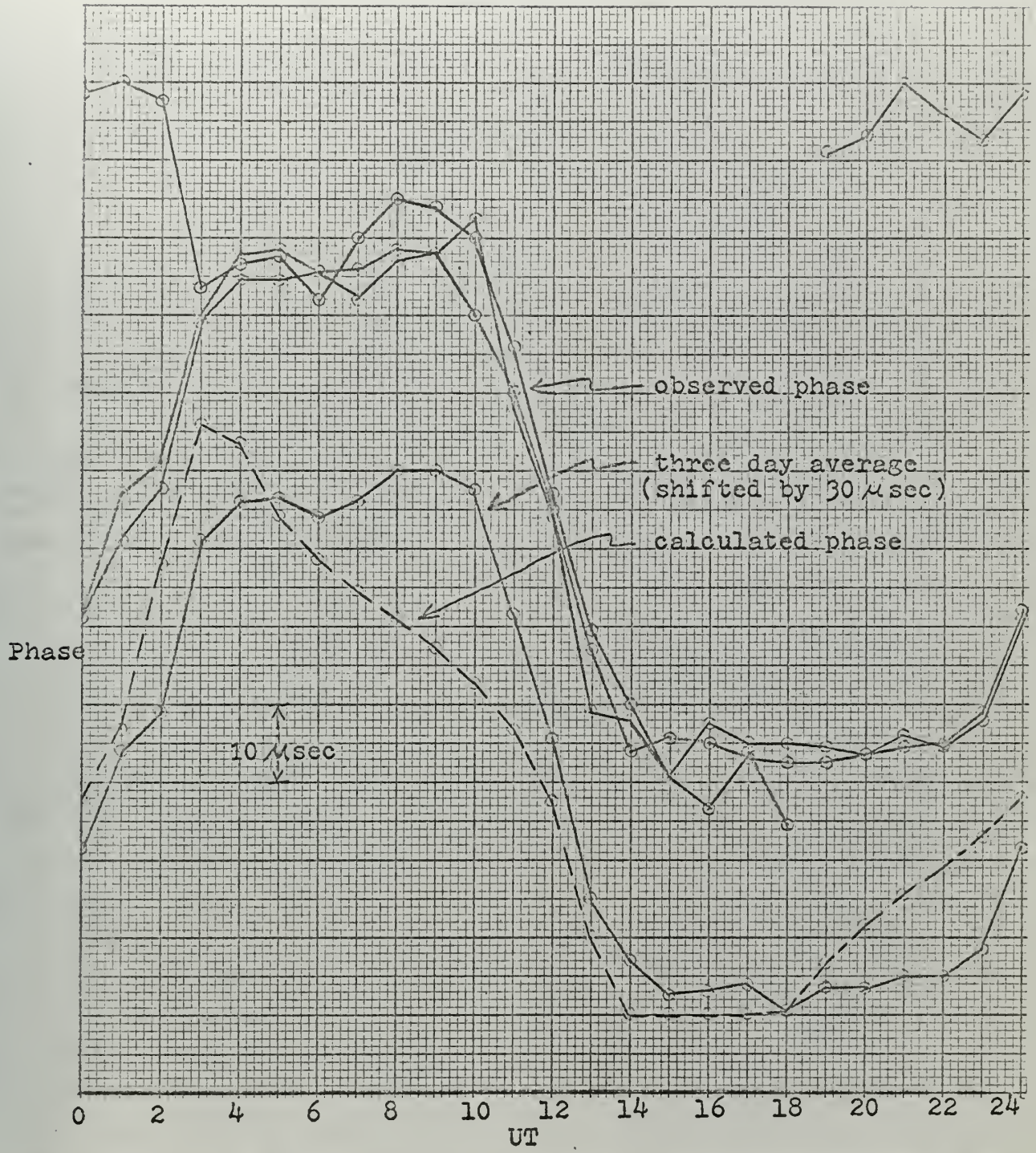

Figure 8-3. Aldra to Monterey phase delay, short path 13.6 kHz, 23-26 September, 1966.

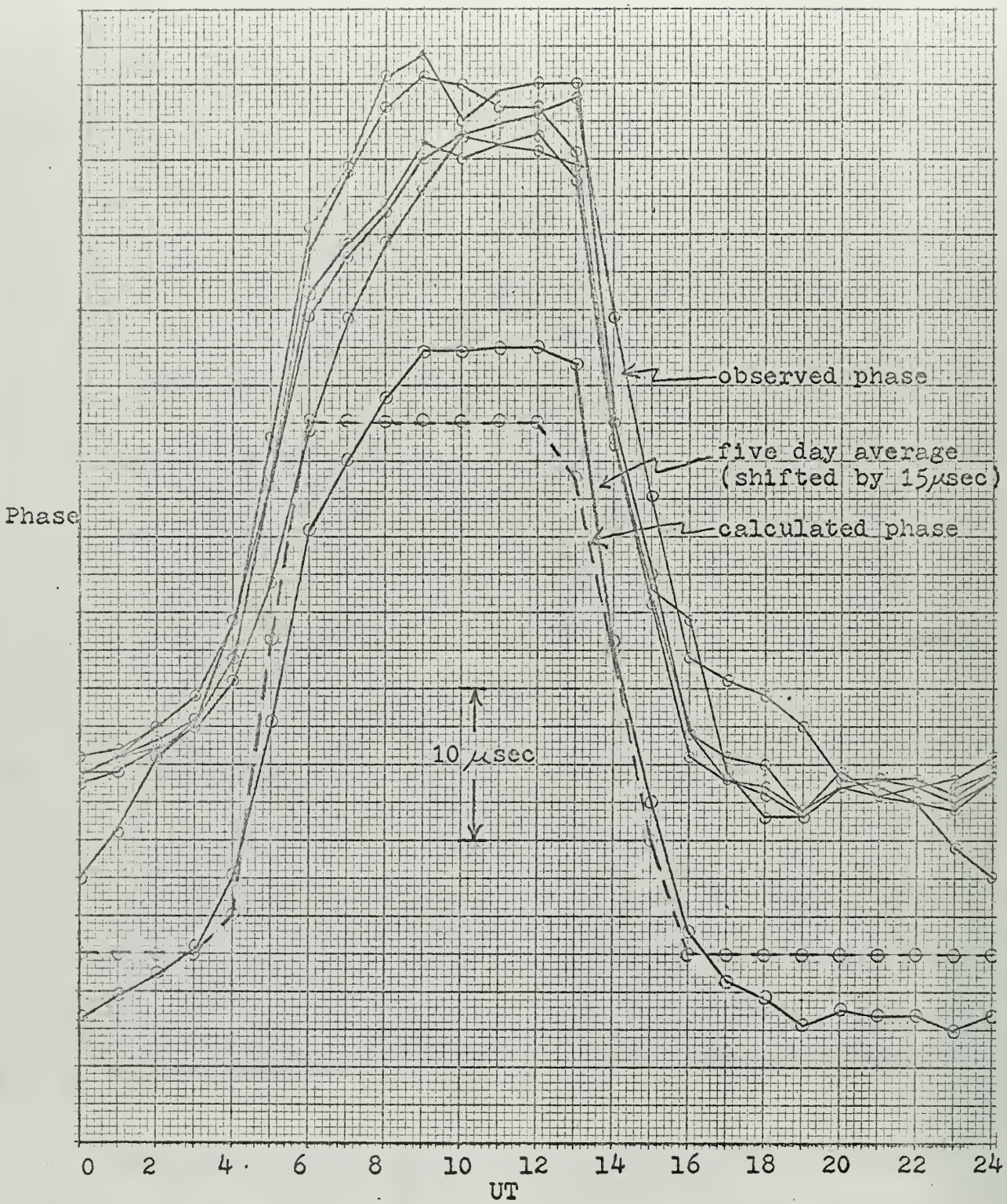

Figure 8-4. Haiku to Monterey phase delay, short path 13.6 kHz, 25 July-1 August, 1966.

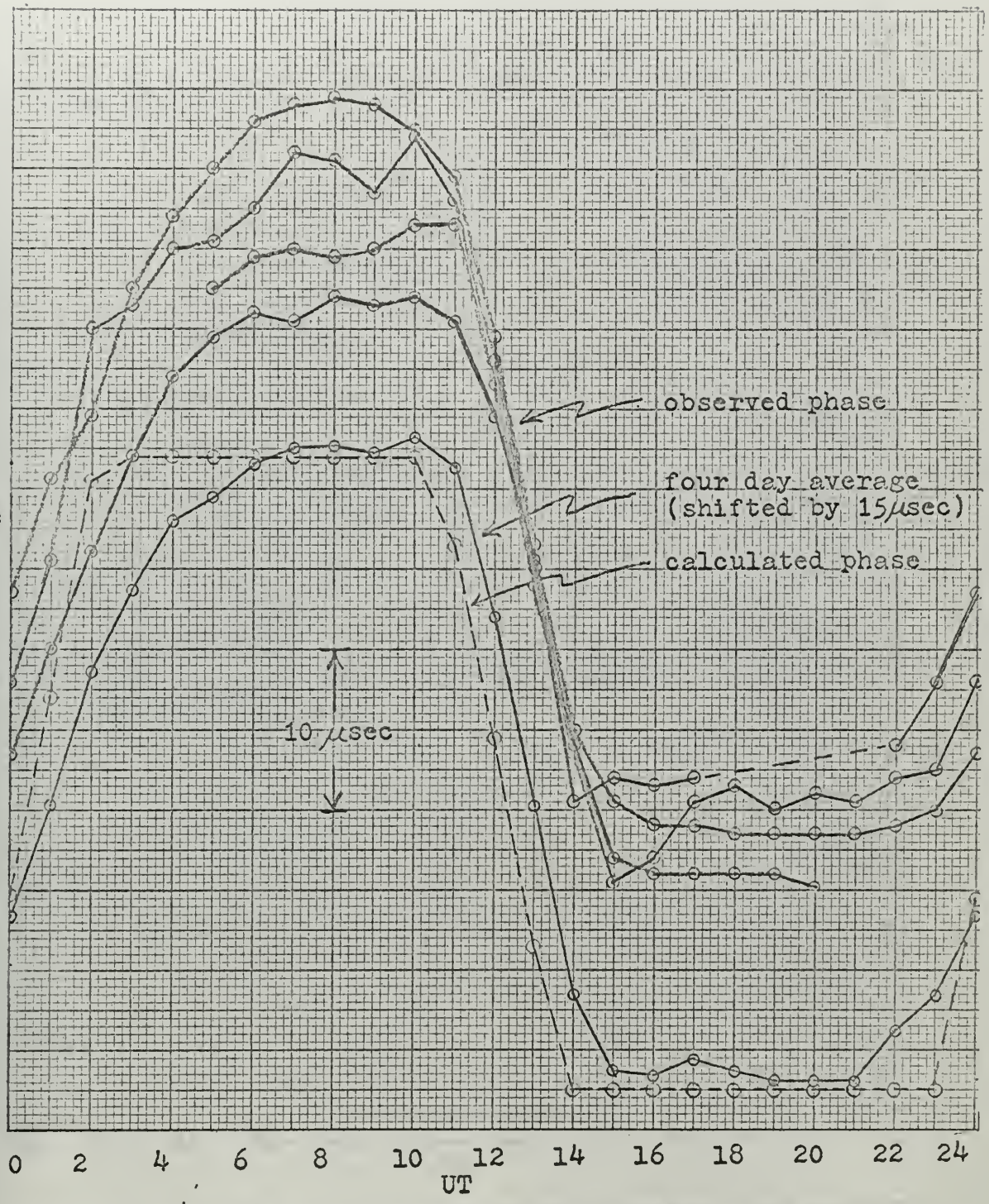

Figure 8-5. Forestport to Monterey phase delay, short path 13.6 kHz, 6-9 October, 1966

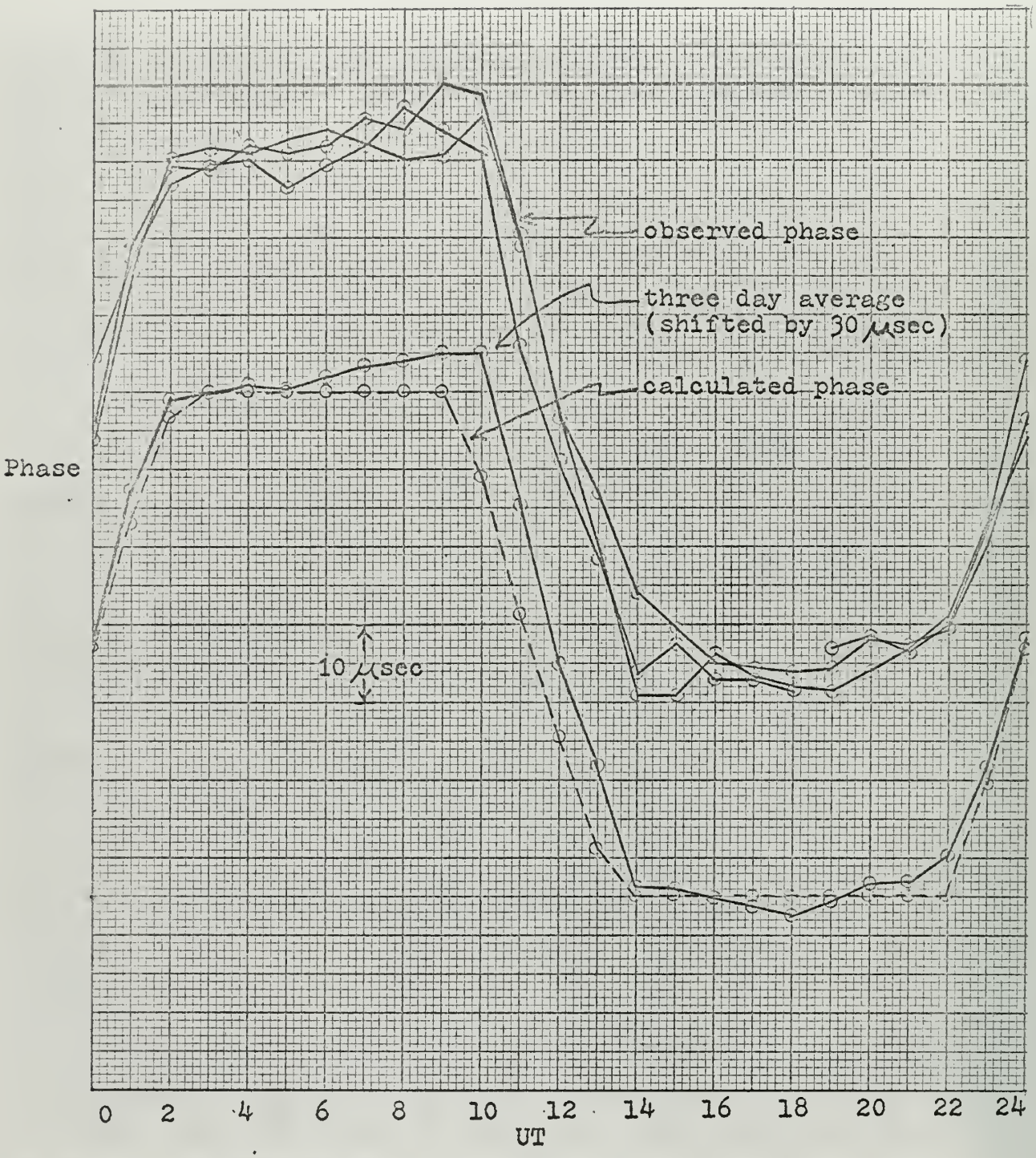

Figure 8-6. Trinidad to Monterey phase delay, short path 13.6 kHz, 11-14 October, 1966

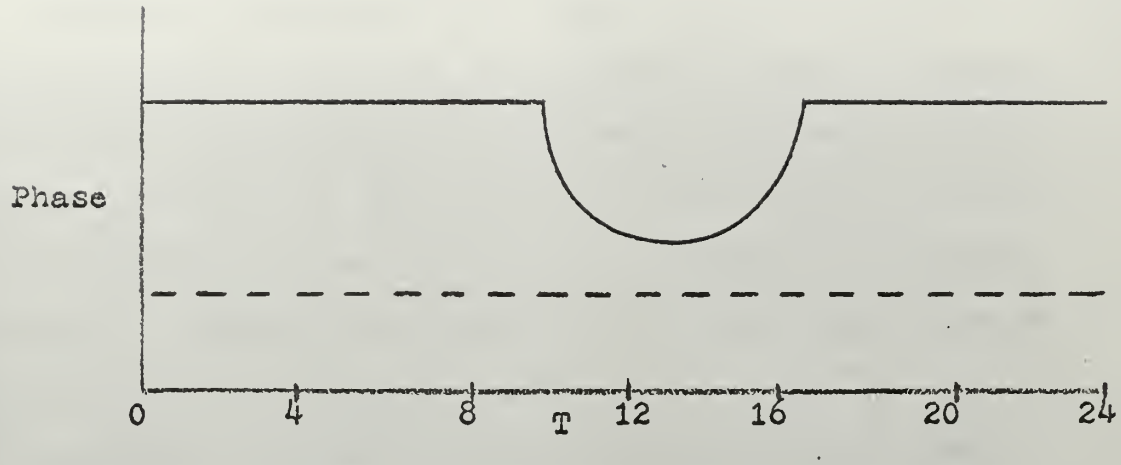

a) Winter

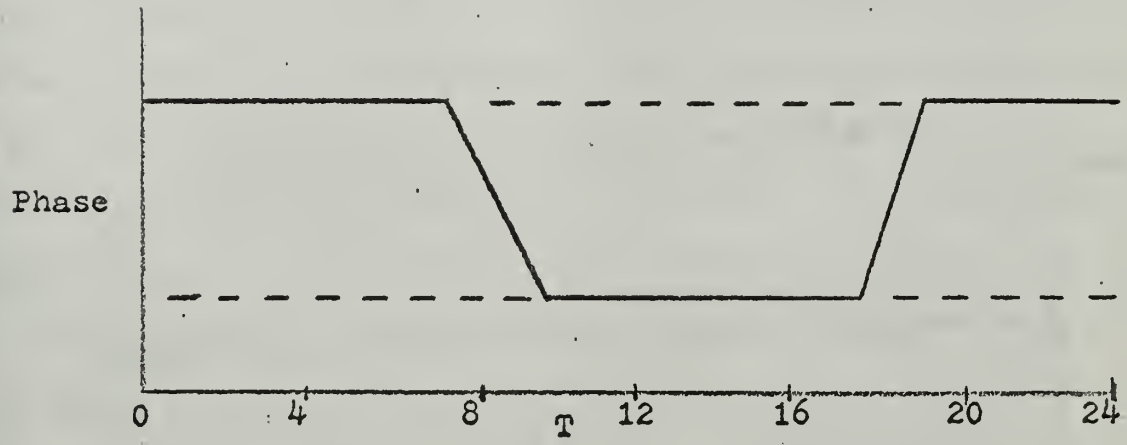

b) Spring and fall

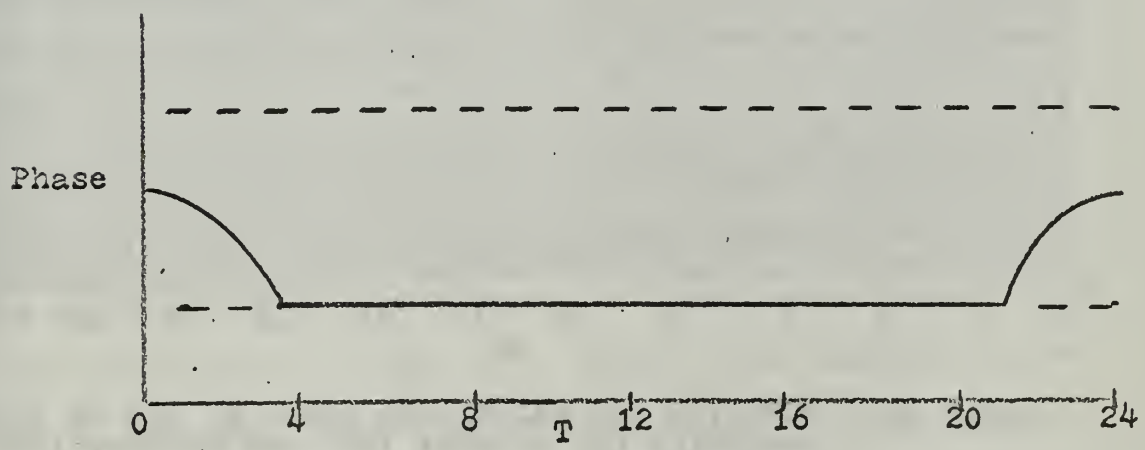

c) Summer

Figure 8-7. Typical diurnal shifts on a polar path.

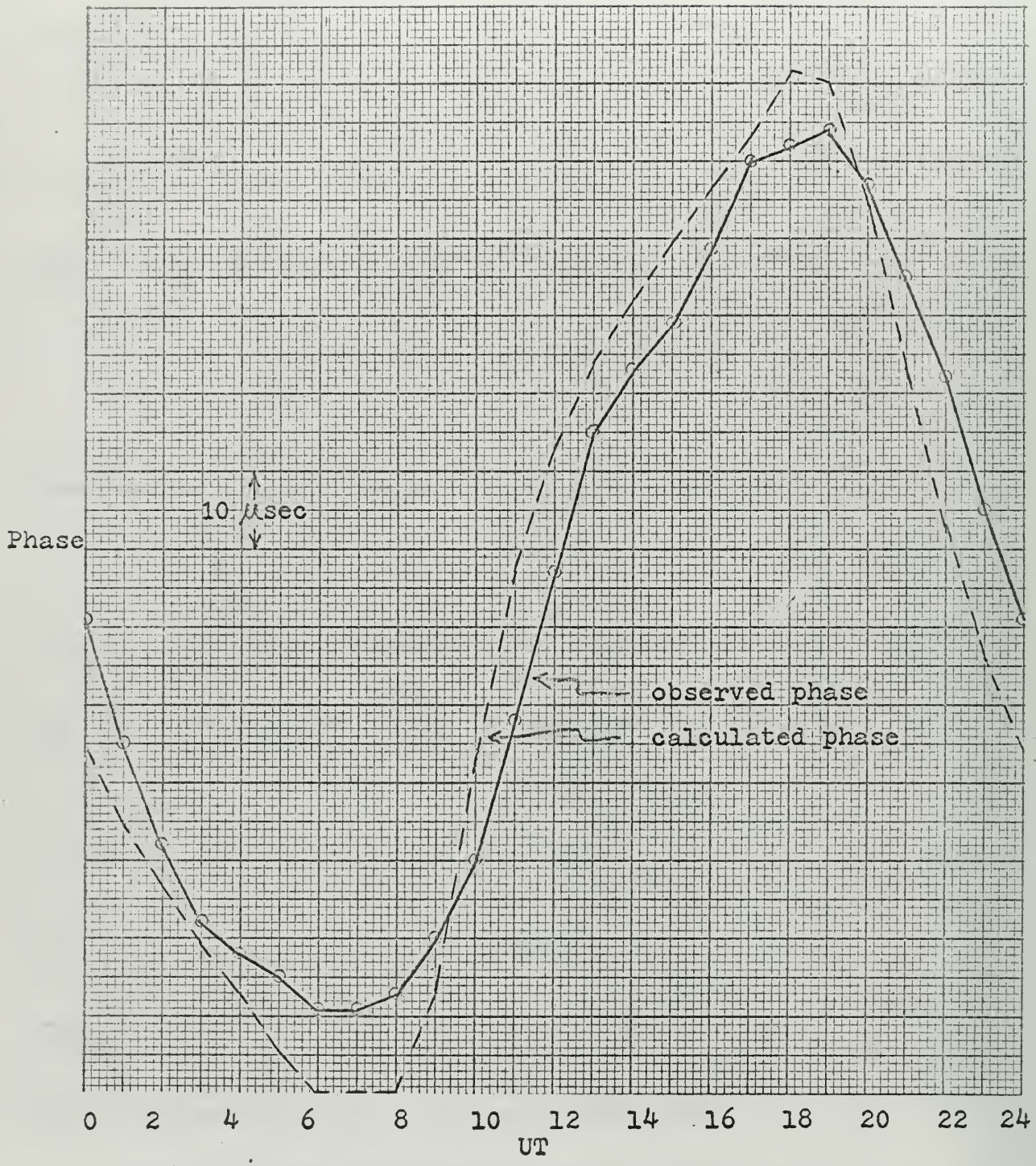

Figure 8-8. Observed and calculated phase of GBR at Sydney, Australia for October 1961 and October 1966 respectively.

9. Calculation of Resultant Signal Phase

As discussed in Section 3, the amplitude and phase of a signal consisting of long and short path components can be obtained by the addition of two phasors. In the navigation system proposed in this paper the phase of the resultant signal at a receiver is of primary interest. The amplitude of the signal is of interest only insofar as it is sufficient to allow phase tracking.

The phase of the resultant signal can be found from the phase of the long and short path signals and their relative amplitudes or attenuations. First take the magnitude of the phasor $\tilde{E}_1$ in Figure 3-3 to be unity, or zero db. Then the magnitude of $\tilde{E}_2$ is the relative attenuation of the short path signal with respect to the long path signal. It can reasonably be assumed that when $|E_2| < 0.1$ the phase of $\tilde{E}_1$ is not appreciably affected by $\tilde{E}_2$ (for $\tilde{E}_2 = 0.1 \angle 90^\circ$, $\phi = 5.7^\circ$ in Figure 3-3).

The relative attenuation for this case is given by the following equation:

$$A = 20 \log \frac{|E_2|}{|E_1|} = -20 \text{ db.}$$

Thus the long path signal must be taken into account whenever the strengths of the two signals are within approximately 20 db of each other.

To obtain the phase of the resultant signal, the phase delay in microseconds, calculated in Section 8, must be converted to an angle. This is easily done by converting to wavelengths, where one wavelength equals 1/f seconds (at 20 kHz, 1/f = 50μsec). One wavelength corresponds to 360° and θ is then the difference between the phase delays on the long and short paths. The angle $\emptyset$ is then given by the following equation:

$$\tan \phi = \frac{|E_2| \sin \theta}{1 + |E_2| \cos \theta}$$

This angle could also be found by adding graphically the phasors $\tilde{E}_1$ and $\tilde{E}_2$.

It must be remembered here that the total phase delay of the resultant signal is equal to ϕ plus the phase delay of the short path signal.

Figures 9-1 through 9-5 show the calculated curves of long and short path attenuation, and short path and resultant phase at Sydney, Australia, and Wellington, New Zealand. The transmitter station used was GBR at 16 kHz and the day was assumed to be 23 September 1966.

In Figure 9-2 the largest difference between the short path phase and the resultant phase is slightly less than one microsecond and the difference in attenuations at that time is 20 db. This verifies the earlier assumption that the resultant phase differs from the short path phase (by an appreciable amount) only when the strength of the long path signal is within 20 db of the short path signal.

Figure 9-4 shows a case where the resultant phase is considerably different from the short path phase. The largest difference here is 12.1 μsec (at 0300) or about 70 electrical degrees, and does not occur at the time when the long path signal is strongest (long path signal is 0.6 db weaker at 0300, 1.8 db stronger at 0500). From about 0800 to 1800 there is approximately 20 db of separation between the two signals and the resultant phase is very close to the short path phase as expected.

In Figure 9-5 the latitude of Wellington was changed by four minutes, lengthening the short path by about seven km and shortening the long path by the same amount. The total phase delay on the short path

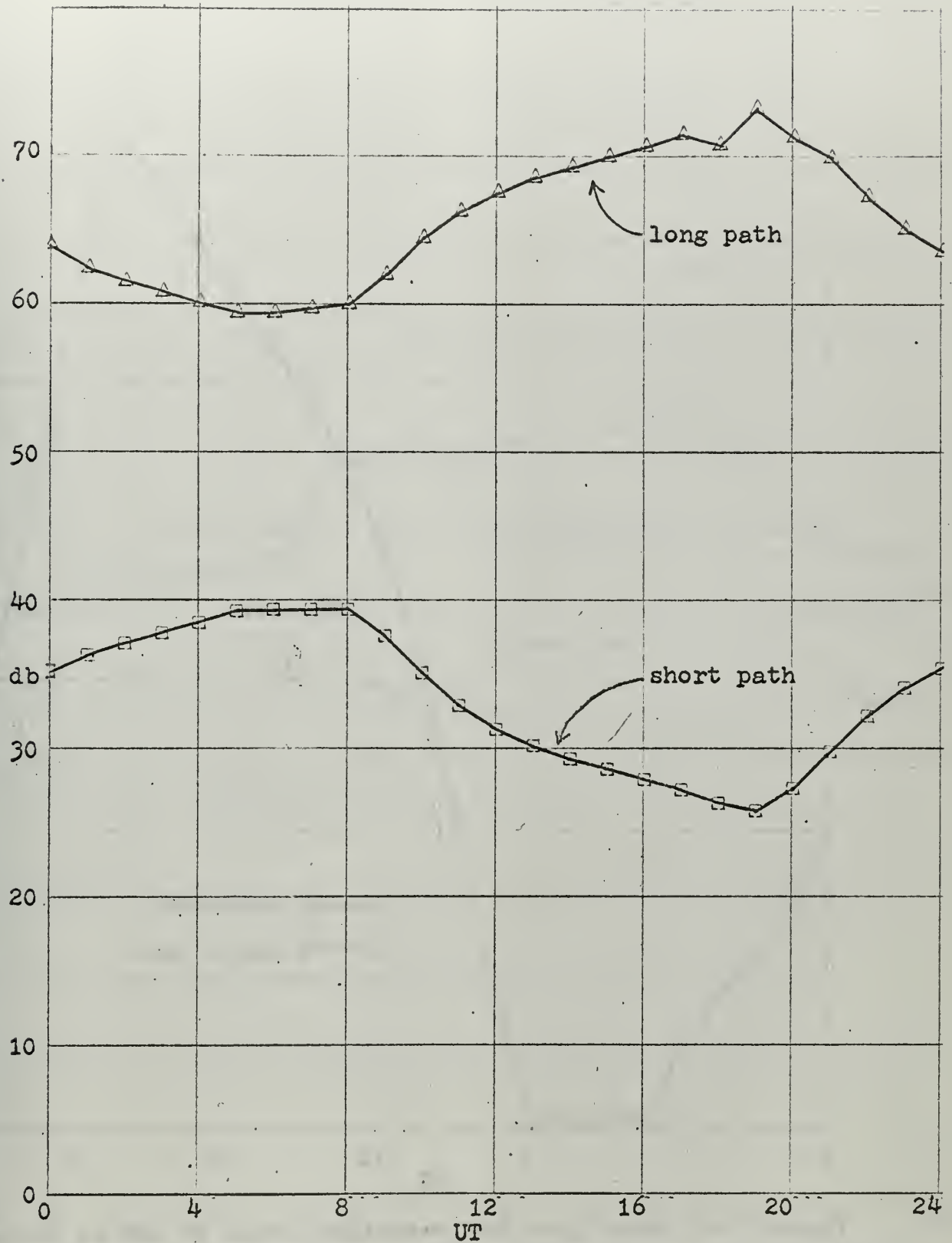

Figure 9-1. Attenuation on GBR to Sydney short and long paths at 16 kHz.

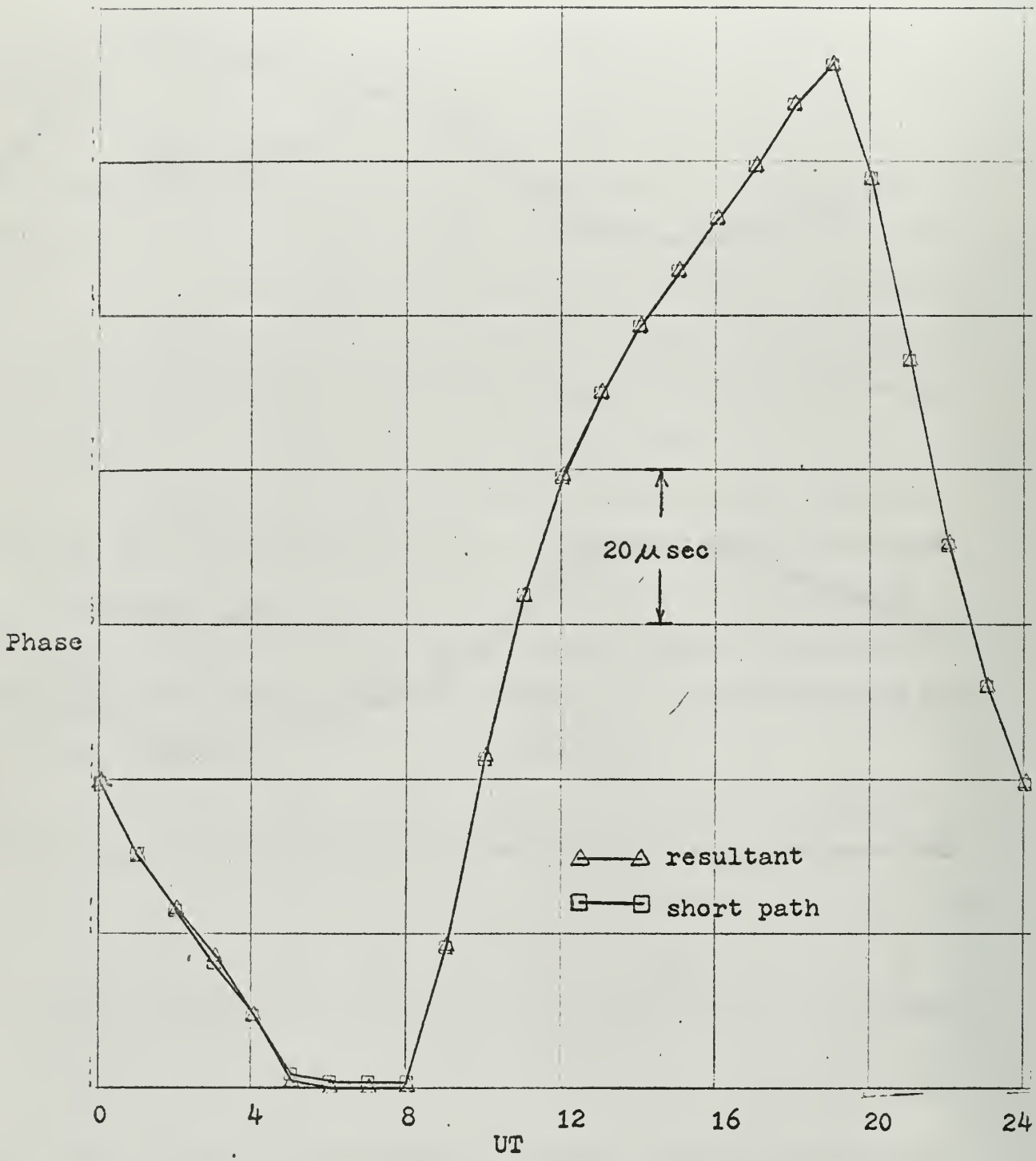

Figure 9-2. Short path and resultant phase of GBR at Sydney.

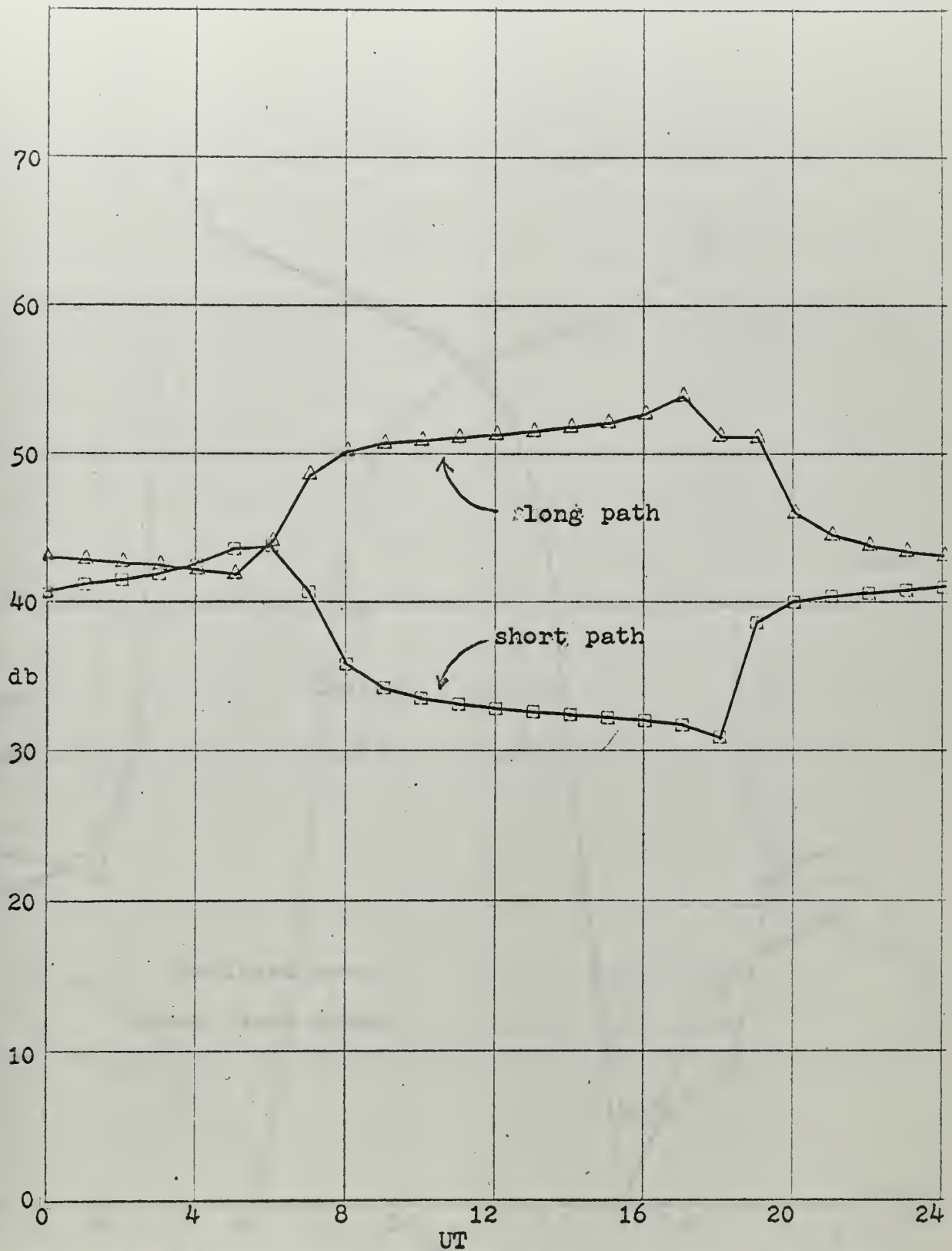

Figure 9-3. Attenuation on GBR to Wellington short and long paths at 16 kHz.

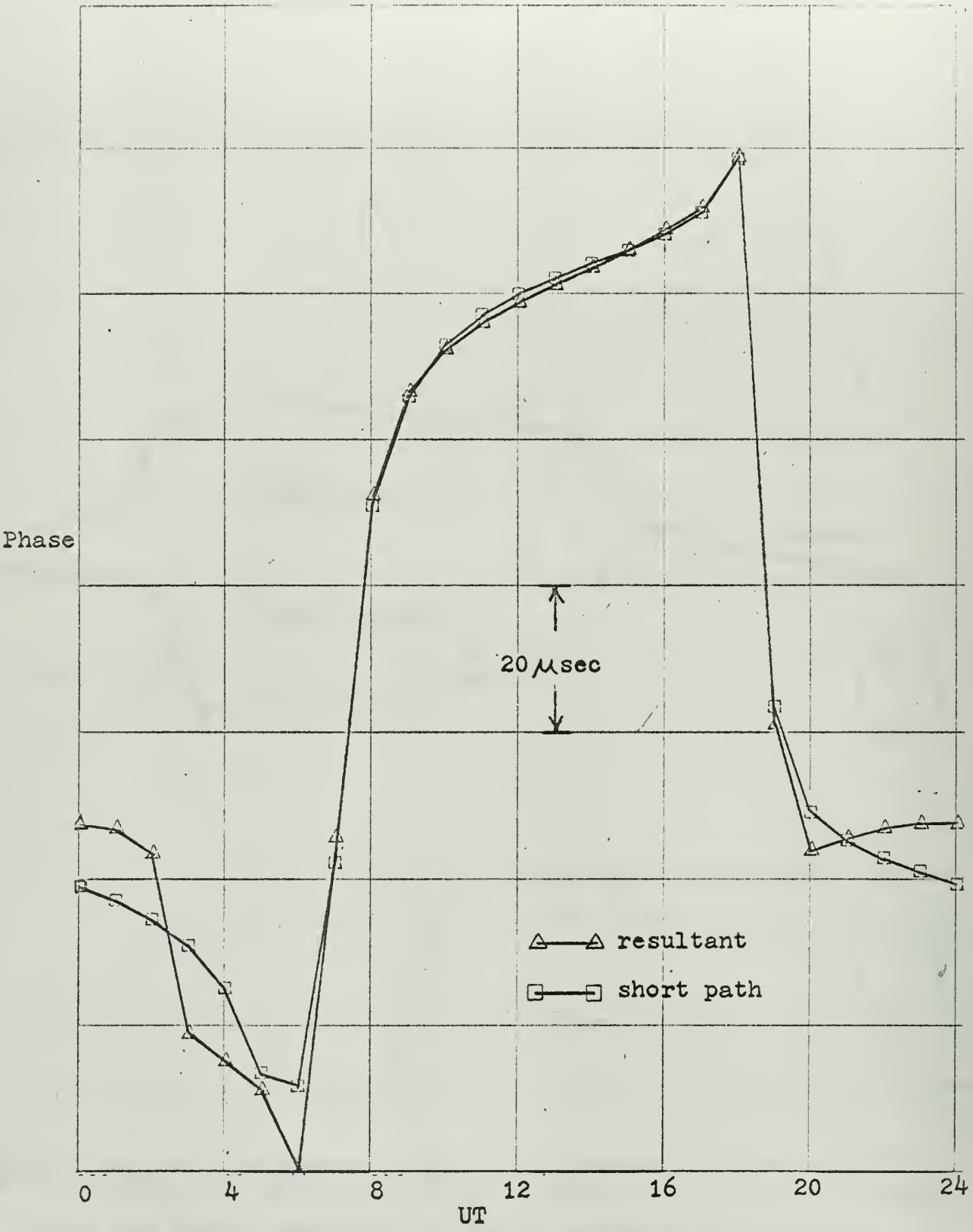

Figure 9-4. Short path and resultant phase of GBR at Wellington

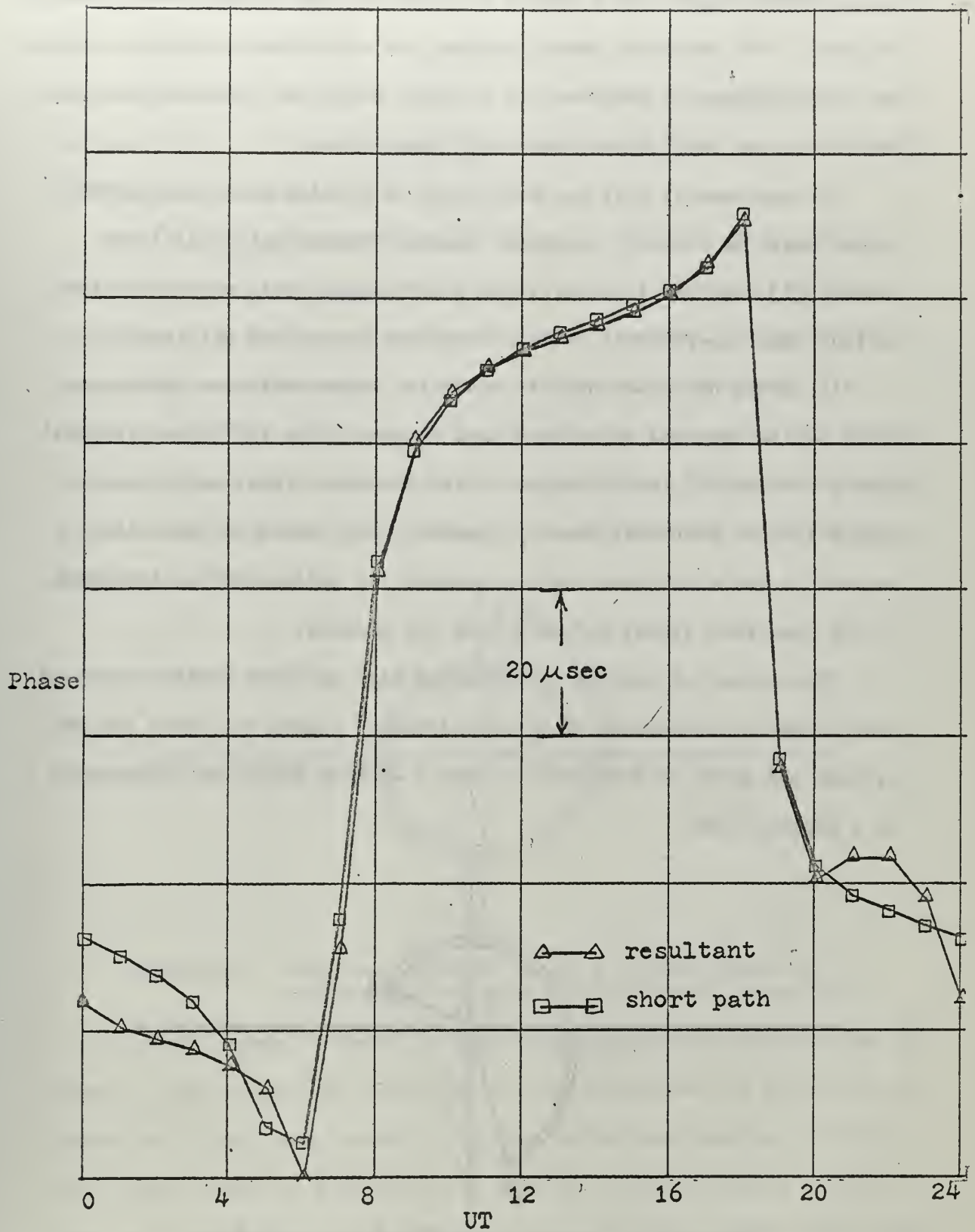

Figure 9-5. Short path and resultant phase of GBR at Wellington. (Short path 7 km longer)

is increased slightly as a result of this, but the diurnal shift remains the same. The resultant phase, however, is considerably different, showing that a change in position has a larger effect on the resultant phase than on either the long or short path phase alone.

No experimental data has been found with which these calculated curves could be directly compared; however, Thompson et al. [14] and Crombie [7] have published articles which discuss this phenomenon and include some experimental evidence taken at Sydney and Wellington.

It should be noted that the resultant phase curves as shown here could not be observed by using a loop antenna. The 180° phase reversal with a reversal of the direction of the incoming signal would cause some different resultant phase to appear. This could be taken into account in the calculated curves, however, by adding 180° to the phase of the long path signal before adding the phasors.

The concept of phasors as discussed here provides another means of describing the phenomenon of cycle-slipping. Figure 9-6 shows the amplitude and phase of some station over a 24-hour period as represented by a phasor trace.

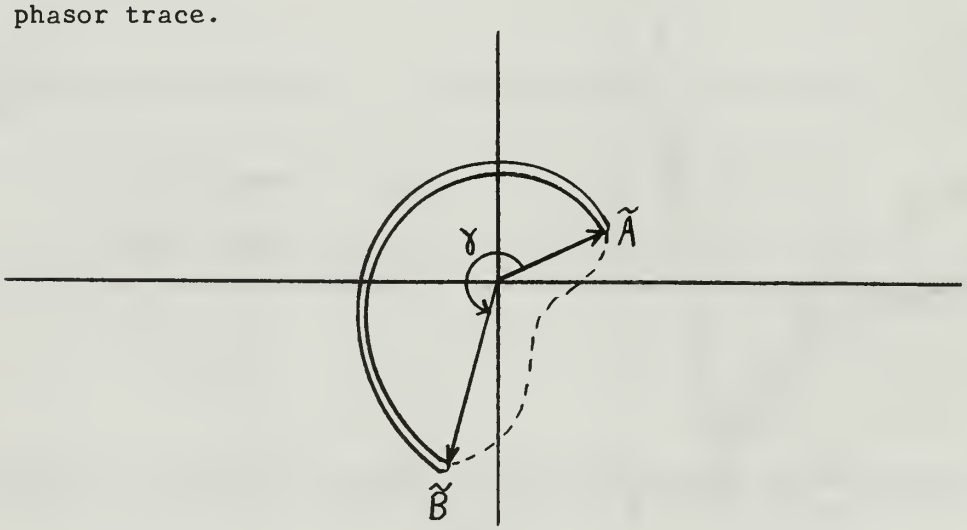

Figure 9-6. Phasor representation of a 24-hour phase and amplitude curve

This figure is drawn assuming a trapezoidal diurnal pattern of both phase delay and amplitude, both being greater at night. Thus $\tilde{A}$ represents the daytime phase and amplitude, $\tilde{B}$ represents the nighttime phase and amplitude, γ is the diurnal phase shift, and $|B| - |A|$ is the nighttime increase in amplitude.

Cycle-slipping has occurred if the curve traced by the phasor encloses the origin, as shown by the dotted line in Figure 9-6. This could be due to long path interference, loss of signal (in which case the magnitude of the vector is zero), or several other causes. The case for which the diurnal shift is greater than one cycle (2π) should not be confused with cycle-slipping as shown here. Figure 9-7 shows one possible curve of this type and it can be seen here how easily cycle-slipping could occur.

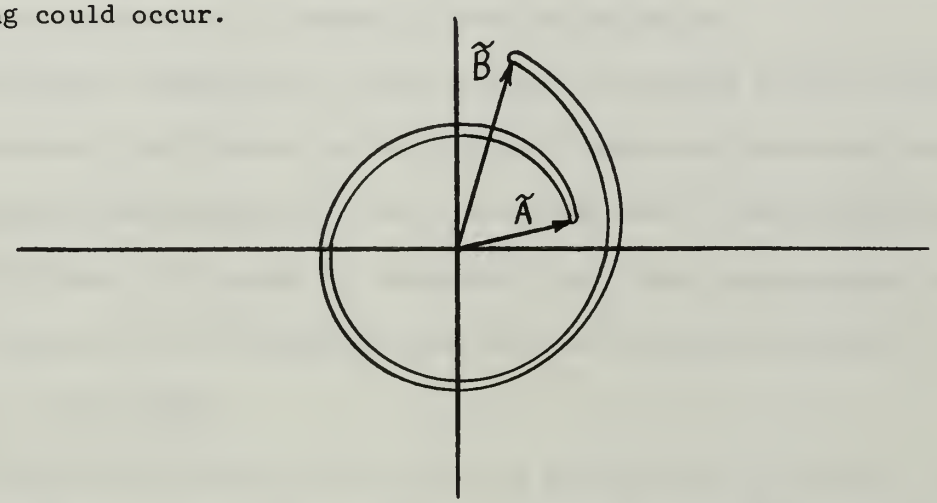

Figure 9-7. Phasor representation of a 24 hour phase and amplitude curve with a large diurnal phase shift

A rapid change in phase, as sometimes experienced during sunset or sunrise, could cause the carrier level in the receiver to be greatly reduced for a time, particularly if a long servo time constant is used. This could result in a phasor trace similar to the one shown in Figure 9-8, with an increased probability of cycle-slipping. This rapid phase

change and resultant cycle-slipping is typical of north-south propagation paths.

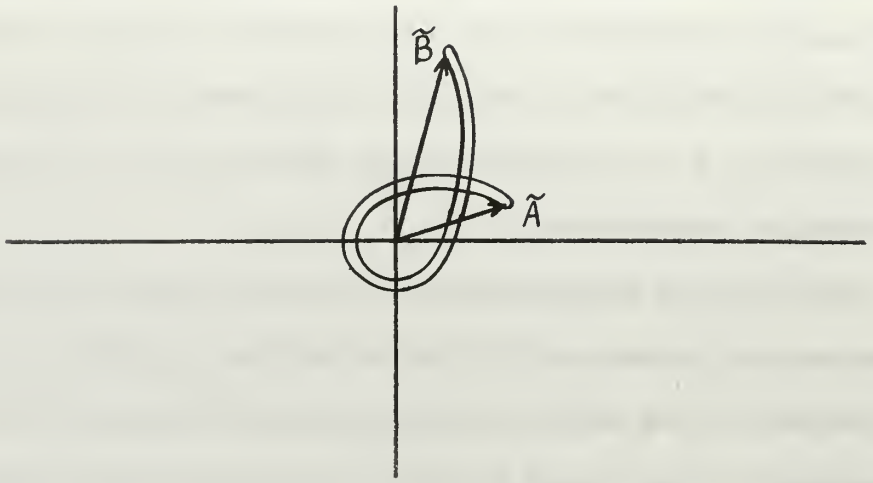

Figure 9-8. Phasor representation of loss of carrier level due to rapid phase change

10. Conclusions

Attenuation rates and relative signal strengths of long and short path signals can be determined easily. The accuracy of the method used here has not been determined, however, because of a lack of dependable experimental data.

It has also been demonstrated that the phase of a signal can be predicted for a typical 24 hour period, both with and without long path interference. Experimental data has shown the short path phase calculations to be very accurate for some cases when three-to five-day averages of observed phase are considered. Lack of experimental data prevented a check of the calculated phase in the presence of long path interference; however, it was shown that when this type of signal is present the phase is highly sensitive to a change in receiver position.

Additional experimental data, possibly from some location other than Monterey, California, would be highly desirable and would probably lead to some modifications of the parameters used in the calculations presented here. It should be emphasized that these calculations are a first iteration in an attempt to predict, at any point on earth, the phase of a VLF signal.

A cardioid antenna system should be suitable for use aboard ship in a VLF relative navigation system. A simple servo system driven by the ship's gyro, and provided at intervals with the true bearing to the desired VLF station, should be adequate to keep the cardioid pattern oriented with sufficient accuracy. With proper adjustment of the cardioid system, interference from the long path signal may be eliminated. In case of a location at which the long path signal is always equal to or greater in strength than that of the short path, however, it may be

impossible to adjust the cardioid system properly, and hence it could not provide the desired amount of long path signal attenuation.

BIBLIOGRAPHY

1. Lambert, W. P. The Distance Between Two Widely Separated Points on the Surface of the Earth. Journal of the Washington Academy of Sciences, v. 32, 1942.

2. Kraus, J. D. Antennas. McGraw-Hill, New York, 1950.

3. Terman, F. E. Electronic and Radio Engineering. McGraw-Hill, New York, 1955.

4. Rainsford, H. F. Long Geodesics on the Ellipsoid. Bulletin Geodesique, New Series, no. 37, 1 September 1955.

5. Chapman, F. W. and Macario, R.C.V. Propagation of Audio Frequency Radio Waves to Great Distances. Nature, vol. 177, 1956.

6. Hill, E. L. VLF Radiation from Lightning Strokes. Proc. IRE, v. 45, no. 6, June 1957.

7. Crombie, D. D. Differences between the east-west and west-east propagation of VLF signals over long distances. Journal of Atmospheric and Terrestial Physics, vol. 12, 1958.

8. Taylor, W. L. and Lange, L. J. Some Characteristics of VLF Propagation Using Atmospheric Waveforms. Proc. Second Conference on Atmos. Electricity. Pergamon Press, London, 1958.

9. Taylor, W. L. VLF Attenuation for East-West and West-East Daytime Propagation Using Atmospherics. Journal of Geophysical Research, vol. 65, 1960.

10. Blackband, W. T. Effects of the Ionosphere on VLF Navigational Aids. Radio Propagation, Journal of Research of the National Bureau of Standards, v. 64D, no. 3, May-June 1961, pp. 575-580.

11. Wait, J. R. Electromagnetic Waves in Stratified Media. The MacMillan Company, 1962.

12. Blackband, W. T. Diurnal Phase Changes in the Arctic Propagation of VLF Waves. Royal Aircraft Establishment (Farnborough) Technical Note No. RAD 814, March 1962.

13. Belser, R. B. and Hicklin, W. H. Aging Characteristics of Quartz Resonators with Comments on the Effect of Radiation. 1963 Proc. 17th Annual Symposium on Frequency Control, pp. 127-175.

14. Thompson, A. M., Archer, R. W., Harvey, I. K. Some Observations on VLF Standard Frequency Transmissions as Received at Sydney, N.S.W. Proc. IEEE, vol. 51, no. 11, Nov. 1963.

15. Guttwein, G. K. Quartz Crystals and Quartz Oscillators. 1964 Proc. International Conference on Chronometry, pp. 30-51.

16. Stanbrough, J. H., Jr. and Keilly, D. P. Long Range Relative Navigation by Means of VLF Transmissions. Deep Sea Research, v. 11, 1964, pp. 249-255.

17. The Nautical Almanac for the Year 1966. United States Naval Observatory, 1964.

18. Watt, A. D., Croghan, R. D. Comparison of Observed VLF Attenuation Rates and Excitation Factors with Theory. RADIO SCIENCE, Journal of Research, National Bureau of Standards, v. 68D, no. 1, Jan. 1964.

19. Chilton, C. J., Steele, F. K. and Crombie, E. E. An Atlas of Solar Flare Effects Observed on Long VLF Paths During 1961. National Bureau of Standards Technical Note No. 210, March 13, 1964.

20. Kirkland, C. Geodesics and LORAN Coordinate Computation. U.S. Naval Oceanographic Office IMR N-1-64, April 1964.

21. Westfall, W. D. Simultaneous Measurement of Phase and Amplitude of NAA Very Low Frequency East-West and West-East Radio Transmissions at San Diego. Journal of Geophysical Research, vol. 69, no. 21, Nov. 1, 1964.

22. Brady, A. H. and Crombie, D. D. Calculation of Sunrise and Sunset Times at Ionospheric Heights Along a Great Circle Path. National Bureau of Standards Technical Note 209, November 8, 1964.

23. Wait, J. R., Spies, K. P. Characteristics of the Earth-Ionosphere Waveguide for VLF Radio Waves. National Bureau of Standards Technical Note 300, 30 Dec. 1964.

24. Austin, LT D. R. An Experimental Investigation of the Effects of Position and Motion of the Frequency Stability of Certain Crystal Oscillators. Unpublished Master's Thesis, Naval Postgraduate School, Monterey, California, 1965.

25. Lake, LCDR Rodney D. An Investigation into the Use of Very Low Frequency Transmissions for Ship Navigation. Unpublished Master's Thesis, Naval Postgraduate School, Monterey, California, 1965.

26. Stanley, J. M. Effects of Transient Radiation on Frequency Control Devices. Transient Radiation Effects on Electronics, Battelle Memorial Institute Handbook, 1965, pp. L-1 to L-11.

27. McNeill, F. A. and Allan, A. H. VLF Phase Anomolies. Journal of Geophysical Research, v. 70, no. 3, February 1, 1965, pp. 731-732.

28. Davies, K. Ionospheric Radio Propagation. National Bureau of Standards Monograph 80, 1 April 1965.

29. Gerber, E. A. and Sykes, R. A. State of the Art--Quartz Crystal Units and Oscillators. Proc. IEEE, vol. 54, no. 2, pp. 103-116, Feb. 1966.

30. McCoubrey, A. O. A Survey of Atomic Frequency Standards. Proc. IEEE, vol. 54, no. 2, pp. 116-135, Feb. 1966.

31. Pierce, J. A., Palmer, W., Watt, A. D., Woodward, R. H. OMEGA, A World-Wide Navigational System. 2nd revision, DDC # AD-630 900. 1 May, 1966.

32. Palmer, W. Intermittent Control of Synchronization. Omega Technical Note No. 9, August 24, 1966.

APPENDIX I

GEODESICS AND LONG PATHS

A. Geodesics

The great circle distance between two points on a sphere is easily calculated; however, determination of the length of a geodesic (analogous to a great circle) on an ellipsoid is more difficult.

Kirkland [20] states very concisely the simplest method of obtaining the length of a geodesic.

Given two points (ϕ_1, λ_1), (ϕ_2, λ_2) find their respective parametric latitudes, β_1 and β_2 as shown in Figure I-1.

ϕ = geodetic latitude
β = parametric latitude
a = equatorial radius
b = polar radius

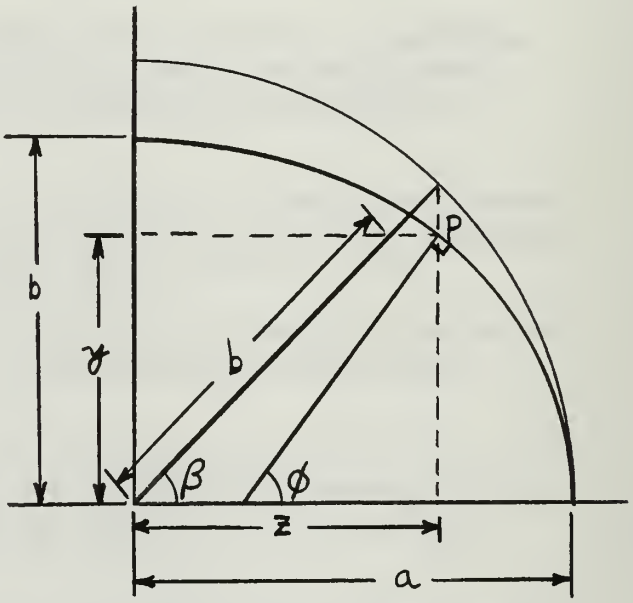

Figure I-1. Geodetic and parametric latitudes

$$\tan\phi = -\frac{dz}{dy}$$

$$z = a\cos\beta$$

$$y = b\sin\beta$$

$$\frac{dz}{dy} = -\frac{a}{b}\tan\beta$$

$$\tan\beta = \frac{b}{a}\tan\phi = c\tan\phi$$

$$\sec^2\beta = 1 + c^2\tan^2\phi$$

$$\cos\beta = \frac{1}{\sec\beta}$$

$$= \frac{\cos\phi}{\sqrt{\cos^2\phi + c^2\sin^2\phi}}$$

$$\sin\beta = \sqrt{1 - \cos^2\beta} = \frac{c\sin\phi}{\sqrt{\cos^2\phi + c^2\sin^2\phi}}$$

The arc distance between the two points (x) is then found from:

$$\cos x = \sin\beta_1\sin\beta_2 + \cos\beta_1\cos\beta_2\cos(\lambda_1 - \lambda_2)$$

and the great circle distance is D = a x .

Now using the correction factors derived by Lambert [1] the length of the geodesic is:

$$d = D - A_o P - B_o Q$$

where $$P = \frac{(a - b)(x - \sin x)}{4(1 + \cos x)}$$

$$Q = \frac{(a - b)(x + \sin x)}{4(1 - \cos x)}$$

$$A_o = (\sin \beta_1 + \sin \beta_2)^2$$

$$B_o = (\sin \beta_1 - \sin \beta_2)^2$$

The accuracy of this method is, according to Lambert, better than $\pm$ 0.05 km but breaks down near the antipodes (i.e. for $x > 175^o$). This method was checked against the examples in an article by Rainsford [4] with the largest error being about 0.85 km. (It should be noted that Rainsford specified the position of the points to within 0.0001 second.)

B. Long Path Distances

The method used in this paper to obtain the long path distance between two points is to find the length of the perimeter of the ellipse on which the two points lie (analogous to the great circle on a sphere) and subtract the geodesic length from this distance.

The major axis of this ellipse is the equatorial radius of the ellipsoid and the minor axis can be found as follows:

β = parametric latitude

x = arc distance between the two points

$$\cos \alpha = \frac{\cos A - \cos x \cos C}{\sin x \sin C}$$

$$= \frac{\sin \beta_2 - \cos x \sin \beta_1}{\sin x \cos \beta_1}$$

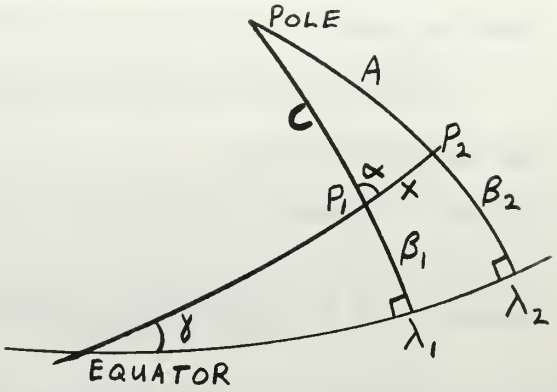

Figure I-2. Ellipse of geodesic

$$\cos \gamma = \sin \alpha \cos \beta_1 = \cos \beta_1 \sqrt{1 - \left[\frac{\sin \beta_2 - \cos x \sin \beta_1}{\sin x \cos \beta_1}\right]^2}$$

Here gamma is the parametric latitude of the northernmost point on the ellipse. From Figure I-3:

$$z = a \cos \gamma$$

$$\frac{z^2}{a^2} + \frac{y^2}{b^2} = 1$$

$$y^2 = b^2 - \frac{b^2}{a^2} z^2 = b^2(1 - \cos^2 \gamma)$$

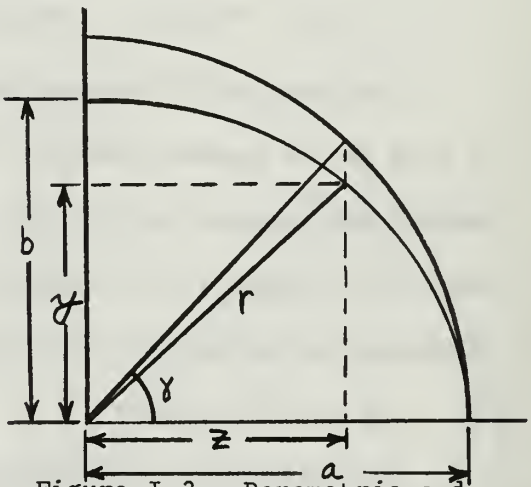

Figure I-3. Parametric and geocentric latitudes

The minor axis of the ellipse of interest is then:

$$r = \sqrt{z^2 + y^2} = \sqrt{b^2 + (a^2 - b^2) \cos^2 \gamma}$$

The length of the perimeter of the ellipse described by a and r is found by evaluating the elliptic integral:

$$E(k) = \int_0^{\pi/2} \sqrt{1 - k^2 \sin^2 x}\, dx$$

where

$$k = \sqrt{1 - \left(\frac{r}{a}\right)^2}$$

The perimeter is then:

$$P = 4\ a\ E\ (k)$$

and the long path distance is:

$$d_L = P - d$$

where d is the geodesic length.

The FORTRAN 60 program used to compute these distances is shown on the following pages along with sample results.

```
      PROGRAM GEODESIC
C      THIS PROGRAM COMPUTES THE DISTANCE BETWEEN TWO POINTS ON THE
C     SURFACE OF THE EARTH ALONG THE GEODESIC (SHORTEST DISTANCE)
C     USING THE EQUATIONS DEVELOPED BY W.P. LAMBERT. A,B, AND C DETERMINE
C     THE SPHERIOD TO BE USED. A IS THE EQUATORIAL RADIUS, B IS THE
C     POLAR RADIUS AND C IS THE RATIO OF THE TWO (B/A). THE SPHEROID
C     IS OFTEN SPECIFIED BY A AND R, THE RECIPROCAL OF THE FLATTENING,
C     R = A/(A - B), IN WHICH CASE C = 1 - 1/R.
C         BESSEL SPHERIOD          A = 6377.397155 KM
C                                  R = 299.1528128
C         INTERNATIONAL SPHERIOD   A = 6378.388 KM
C                                  R = 297.0
C         BOMFORD SPHERIOD (1960)  A = 6378.155 KM
C                                  B = 6356.773 KM
C                                  R = 298.3
C     INPUT IS LAT. AND LONG. OF THE TWO POINTS OF INTEREST, IN
C     DEGREES MIN. AND SEC., ON ONE DATA CARD. PRINTED OUTPUT LISTS
C     LAT. AND LONG. OF EACH POINT IN RADIANS AND THE GEODESIC IN
C     NAUTICAL MILES AND KM.
C     GREAT CIRCLE OUTPUT IS THE DECLINATION  OF THE GREAT CIRCLE PATH
C     WITH RESPECT TO THE EQUATOR AND THE LONGITUDE OF THE POSITION
C     WHERE THE GREAT CIRCLE CROSSES THE EQUATOR
C     NORTH LATITUDE IS POSITIVE, WEST LONG. IS POSITIVE.
      PI = 3.1415926536
      A = 6378.155
      B = 6356.773
      C=B/A
      RADD = .017453292519
      RADM = 2.908820866E-4
      RADS = 4.848136811E-6
      COMMON DK
F     ELIPSE
      PRINT 6
    6 FORMAT(99H1                    PATH                                GEODESIC
     3           LONG PATH          GREAT CIRCLE  )
      PRINT 7
```

```
    7 FORMAT(99H                                                    NAUT MI
     2KM       NAUT MI      KM        DECL.      LONG.)
       DIMENSION PHI(2), SINB(2),COSB(2)
    5 READ 4,PHI1D,PHI1M,PHI1S,ZL1D,ZL1M,ZL1S,PHI2D,PHI2M,PHI2S,ZL2D,
     1ZL2M,ZL2S, POSA, POSB, POSC, POSD
    4 FORMAT(F3.0,2F3.0, F5.0,2F3.0,F5.0, 2F3.0, F5.0,2F3.0, 4A8)
       PHI(1) = RADD*PHI1D + RADM*PHI1M + RADS*PHI1S
       ZL1 = RADD*ZL1D + RADM*ZL1M + RADS*ZL1S
       PHI(2) = RADD*PHI2D + RADM*PHI2M + RADS*PHI2S
       ZL2 = RADD*ZL2D + RADM*ZL2M + RADS*ZL2S
       DO 1 I=1,2
       CSPH1 = COSF(PHI(I))
       CSPH2 = CSPH1*CSPH1
       SNPH1 = SINF(PHI(I))
       SNPH2 = SNPH1*SNPH1
       S = SQRTF(CSPH2 + C*C*SNPH2)
       SINB(I) = C*SNPH1/S
    1 COSB(I) = CSPH1/S
       ZL3 = ABSF(ZL1 - ZL2)
       COSL = COSF(ZL3)
       COSX = SINB(1)*SINB(2) + COSB(1)*COSB(2)*COSL
       SINX = SQRTF(1. - COSX*COSX)
       X = ATANF(SINX/COSX)
       IF(COSX) 2,3,3
    2 X = X + PI
    3 P =((A-B)*(X - SINX))/(4.*(1. + COSX))
       Q = ((A-B)*(X + SINX))/(4.*(1. - COSX))
       AO = (SINB(1) + SINB(2))*(SINB(1) + SINB(2))
       BO= (SINB(1) - SINB(2))*(SINB(1) - SINB(2))
       DISTKM = A*X - AO*P - BO*Q
       DISTNM = DISTKM/1.852
C      FOR THE FOLLOWING COMPUTATIONS THE GEOCENTRIC LATITUDE, PSI, MUST
C      BE USED.
       PSI1=ATANF((B*B/(A*A))*TANF(PHI(1)))
       PSI2=ATANF((B*B/(A*A))*TANF(PHI(2)))
```

```
   40 IF(ZL2 - PI)70070060
   50 IF(ZL3 - PI) 60,70,70
   60 ZL1 = ZL2
      ZL2 = RADD*ZL1D + RADM*ZL1M + RADS*ZL1S
      COSB(1) = COSF(PSI2)
      SINB(1) = SINF(PSI2)
      COSB(2) = COSF(PSI1)
      SINB(2) = SINF(PSI1)
      GO TO 75
   70 CONTINUE
      COSB(1)=COSF(PSI1)
      SINB(1)=SINF(PSI1)
      COSB(2)=COSF(PSI2)
      SINB(2)=SINF(PSI2)
   75 COSX=SINB(1)*SINB(2)+COSB(1)*COSB(2)*COSL
      SINX = SQRTF(1.  -(COSX**2))
      BMOD = SQRTF(B*B+(A*A-B*B)*((COSB(1))**2)*(1. - ((SINB(2) - COSX*S
     4INB(1))/(SINX*COSB(1)))**2))
      DK = SQRTF(1.- (BMOD/A)**2)
      CALL SIMPSON(0,PI/2., EK, ELIPSE, 3.0E-8, NDIV)
      DLNGKM = 4.*A*EK - DISTKM
      DLNGNM = DLNGKM/1.852
      GAMMA = ACOSF(COSB(1)*SQRTF(1. - ((SINB(2) - COSX*SINB(1))/(SINX
     1 *COSB(1)))**2))*180./PI
      TALFA = ACOSF((SINB(2)-COSX*SINB(1)) /(SINX*COSB(1)))
      XLAM3 = (ZL1+ATANF(SINB(1)*TANF(TALFA)))*180./PI
      ZL9 = ZL1*180./PI
      IF (XLAM3 - ZL9) 13,13,12
   12 XLAM3 = XLAM3 - 180.
   13 PRINT 8, POSA, POSB,POSC,POSD,     DISTNM,DISTKM,DLNGNM,DLNGKM,
     1 GAMMA,XLAM3
    8 FORMAT(9X4A8, 4F10.2,2F10.5)
      IF(PHI(1) - PHI(2)) 5,9,5
    9 IF (ZL3) 5,15,5
   15 END
      SUBROUTINE SIMPSON(A,B,ANS,FUNC,ERR,NDIV)                    0000
```

```
C       SIMPSONS RULE                                                   0000
C       A=LOWER LIMIT                                                   0000
C       B=UPPER LIMIT                                                   0000
C       ANS=ANSWER OR VALUE OF INTEGRAL                                 0000
C       ERR=TEST                                                        0000
C       NDIV=NUMBER OF DIVISIONS
C       FUNC=FUNCTION SUBROUTINE WHICH DEFINES INTEGRAND                0000
        NDIV=1                                                          0000
        PREV=0.                                                         0000
        SONE=(B-A)*(FUNC(A)+FUNC(B))/2.
   10   NDIV=2*NDIV                                                     0000
        STWO=0.                                                         0000
        DEL=(B-A)/FLOATF(NDIV)                                          0000
        DO 20 I=1,NDIV,2                                                0000
        X=A+DEL*FLOATF(I)                                               0000
        STWO=STWO+FUNC(X)                                               0000


   20   CONTINUE                                                        0000
        CUR=SONE+4.*DEL*STWO                                            0000
        IF (ERR*ABSF(CUR)-ABSF(CUR-PREV)) 30,40,40                      0000
   30   PREV=CUR                                                        0000
        SONE=(SONE+CUR)/4.                                              0000
        GO TO 10                                                        0000
   40   ANS=CUR/3.                                                      0000
        RETURN
        END
        FUNCTION ELIPSE(X)
        COMMON DK
        ELIPSE = SQRTF(1. - (DK*SINF(X))**2)
        RETURN
        END
        END
```

```
66 25 15 -013-09-10    36 36     121 52 30 ALDRA TO MONTEREY
10 42 06   61 38 20    36 36     121 52 30 TRINIDAD TO MONTEREY
21 24 21  157 49 48    36 36     121 52 30 HAIKU TO MONTEREY
43 26 41   75 05 10    36 36     121 52 30 FORRESTPORT TO MONTEREY
52 22      01 11       36 36     121 52 30 GBR TO MONTEREY
44 39      67 17       36 36     121 52 30 NAA TO MONTEREY
48 12     121 55       36 36     121 52 30 NLK/NPG TO MONTEREY
40 40 51  105  3  2    36 36     121 52 30 WWVL TO MONTEREY
38 59      76 27       36 36     121 52 30 NSS TO MONTEREY
 9  4      79 39       36 36     121 52 30 NBA TO MONTEREY
21 25     158  9       36 36     121 52 30 NPM TO MONTEREY
```

Sample input

PATH	GEODESIC		LONG PATH	
	NAUT MI	KM	NAUT MI	KM
ALDRA TO MONTEREY	4296.85	7957.77	17307.84	32054.12
TRINIDAD TO MONTEREY	3595.49	6658.85	18029.96	33391.48
HAIKU TO MONTEREY	2082.34	3856.50	19541.97	36191.73
FORRESTPORT TO MONTEREY	2166.17	4011.74	19455.49	36031.57
GBR TO MONTEREY	4645.45	8603.37	16963.99	31417.31
NAA TO MONTEREY	2492.58	4616.27	19128.08	35425.21
NLK/NPG TO MONTEREY	695.76	1288.55	20906.82	38719.43
WWVL TO MONTEREY	826.35	1530.41	20796.33	38514.81
NSS TO MONTEREY	2142.68	3968.25	19481.17	36079.13
NBA TO MONTEREY	2825.75	5233.30	18796.15	34810.48
NPM TO MONTEREY	2096.87	3883.40	19527.51	36164.95

Sample output

APPENDIX II

PROPORTION OF DAYLIGHT AND DARKNESS ON PATHS OF PROPAGATION

The difference in the height of the D-layer of the ionosphere from day to night is the largest single cause of variations in the phase velocities of VLF waves and causes variations in the attenuation rates of a magnitude equal to those caused by other factors. Because of this the percentage of daylight and darkness on each path of interest must be calculated as a function of time.

This problem has been solved by Brady and Crombie [22]. However, since the following solution was developed independently, it will be outlined here.

The following is based on the premise that the percentage of daylight on a path can be found if four points are known: (1) transmitter location, (2) receiver location, (3) and (4) intersection of the sunrise and sunset lines with the great circle path between (1) and (2). (A spherical earth of unspecified radius is assumed.)

The great circle path can be described by the longitude of one of the points where it crosses the equator (λ_1) and its declination at the equator (α_1). The sunrise-sunset line forms another great circle that can be described in the same way. The intersection of these two great circles on the sunrise side of the earth will determine the coordinates of point (3) mentioned previously. The geometry of the situation is shown in Figure II-1.

Here:

$$\lambda_2 = 15t - 90 \text{ degrees}$$

$$\alpha_2 = \alpha_s + 90 \text{ degrees}$$

where

t = GMT

α_s = declination of the sun

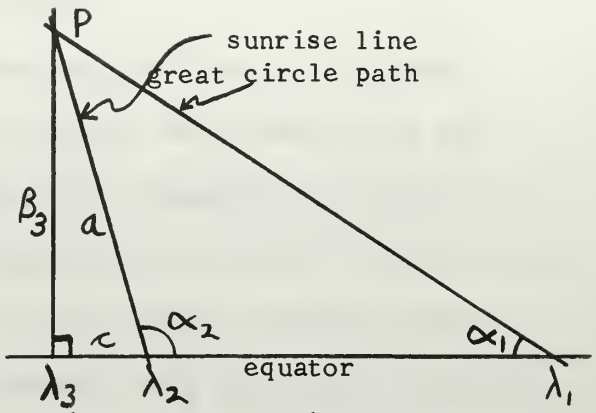

Figure II-1. Point of sunrise on great circle path

Using spherical trigonometry the coordinates of P (β_3, λ_3) can easily be found:

$$a = \tan^{-1}\left[\tan\tfrac{1}{2}(\lambda_2 - \lambda_1)\frac{\cos\tfrac{1}{2}(\alpha_1 - \alpha_2)}{\cos\tfrac{1}{2}(\alpha_1 + \alpha_2)}\right]$$

$$+ \tan^{-1}\left[\tan\tfrac{1}{2}(\lambda_2 - \lambda_1)\frac{\sin\tfrac{1}{2}(\alpha_1 - \alpha_2)}{\sin\tfrac{1}{2}(\alpha_1 + \alpha_2)}\right]$$

$$\tan c = \tan a \cos(180^\circ - \alpha_2) = -\tan a \cos\alpha_2$$

$$\lambda_3 = \lambda_2 + c$$

$$\sin\beta_3 = \sin a \sin\alpha_2$$

The point at which the sunset line crosses the great circle path is then:

$$\lambda_4 = \lambda_3 \pm 180^\circ$$

$$\beta_4 = -\beta_3$$

At a height of 70 km the point P will be further along the great circle path in a direction away from the sun. Figure II-2 shows the arc distance by which the sunrise and sunset lines are shifted.

Here:

h = ionospheric height

S = screening height

R = earth radius

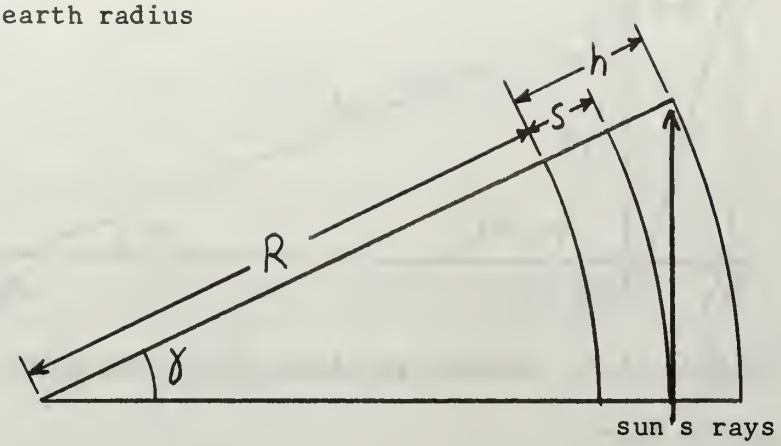

Figure II-2. Sunrise/sunset at ionospheric height

The screening height, mentioned by Brady and Crombie [22], is the height below which the components of the sun's rays that most affect ionization cannot penetrate. This, in effect, changes the radius of the earth by an amount S. From Figure II-2 then:

$$\cos\gamma = \frac{R + S}{R + H}$$

The point at which this new sunrise line crosses the great circle path (P_1) is shown in Figure II-3. The coordinates of this point can be found by spherical trigonometry:

$$\tan\tfrac{1}{2}(a + d) = \tan\tfrac{1}{2}(\lambda_2 - \lambda_1)\frac{\cos\tfrac{1}{2}(\alpha_1 - \alpha_2)}{\cos\tfrac{1}{2}(\alpha_1 + \alpha_2)}$$

$$\tan\tfrac{1}{2}(a - d) = \tan\tfrac{1}{2}(\lambda_2 - \lambda_1)\frac{\sin\tfrac{1}{2}(\alpha_1 - \alpha_2)}{\sin\tfrac{1}{2}(\alpha_1 + \alpha_2)}$$

$$\cot\tfrac{1}{2}\psi = \tan\tfrac{1}{2}(\alpha_1 - \alpha_2)\frac{\sin\tfrac{1}{2}(a + d)}{\sin\tfrac{1}{2}(a - d)}$$

$$\sin\Delta d = \frac{\sin\gamma}{\sin\psi}$$

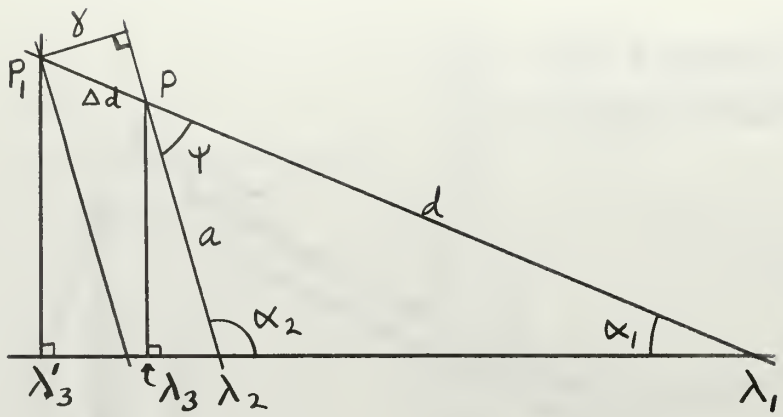

Figure II-3. Revised position of sunrise point

From Figure II-4:

$$\cos\rho = \sin\alpha_1 \cos(\lambda_3 - \lambda_1)$$

$$\cot\theta = \frac{\cot\Delta d \cos\beta_3 - \sin\beta_3 \cos\rho}{\sin\rho}$$

$$\lambda'_3 = \lambda_3 + \theta$$

$$\sin\beta'_3 = \sin\beta_3 \cos\Delta d + \cos\beta_3 \sin\Delta d \cos\rho$$

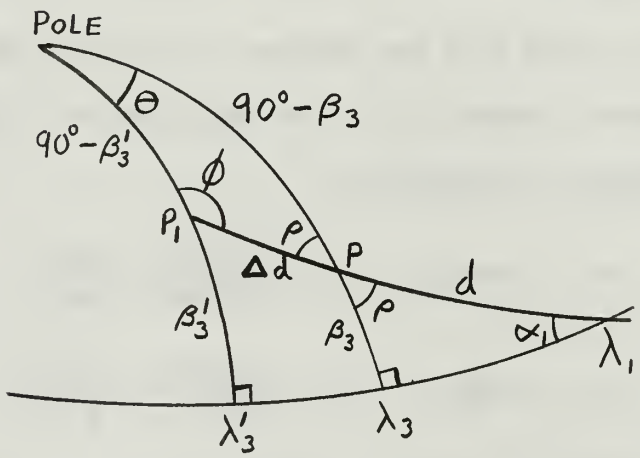

Figure II-4. Sunrise position coordinates

The coordinates of the point of sunset (β'_4, λ'_4) can be found in a similar manner from Figures II-5 and II-6:

$$\lambda_4 = \lambda_3 \pm 180^\circ$$

$$\beta_4 = -\beta_3$$

$$\Delta d' = -\Delta d$$

$$\cot \theta' = \frac{\cot \Delta d' \cos \beta_4 + \sin \beta_4 \cos \rho}{\sin \rho}$$

$$\lambda_4' = \lambda_4 + \theta'$$

$$\sin \beta_4' = \sin \beta_4 \cos \Delta d - \cos \beta_4 \sin \Delta d \cos \rho$$

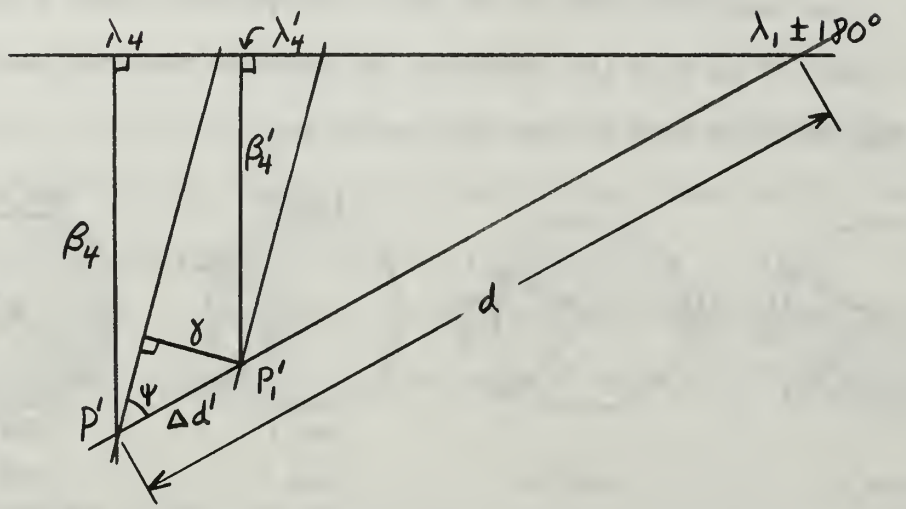

Figure II-5. Revised position of sunset point

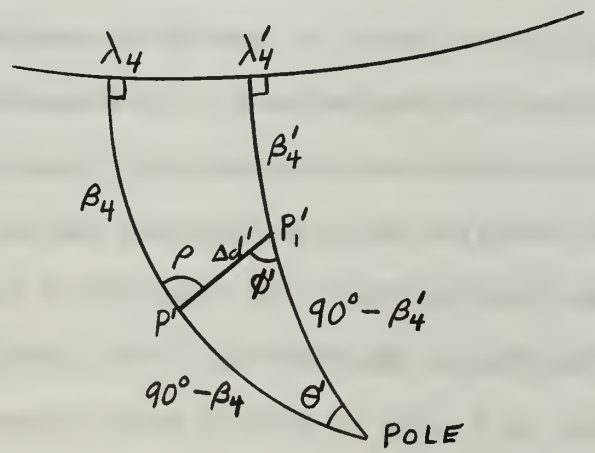

Figure II-6. Sunset position coordinates

It should be noted here that if it is assumed that β_4 and $\Delta d'$ are negative quantities, then θ' will also be negative and the resulting longitude correction will be in the opposite direction from the sunrise

longitude correction.

Once the coordinates of the four required points are determined the amount of sunlight can easily be found with the aid of Figure II-7. This shows the four possible situations that can exist on the great circle path of propagation. Points (1) and (2) are the transmitter and receiver positions, (3) is the sunrise point, and (4) is the sunset point. The amount of daylight on the short path for case A is the distance from (3) to (2); the amount of daylight on the long path for case A is the distance from (4) to (2), and so on.

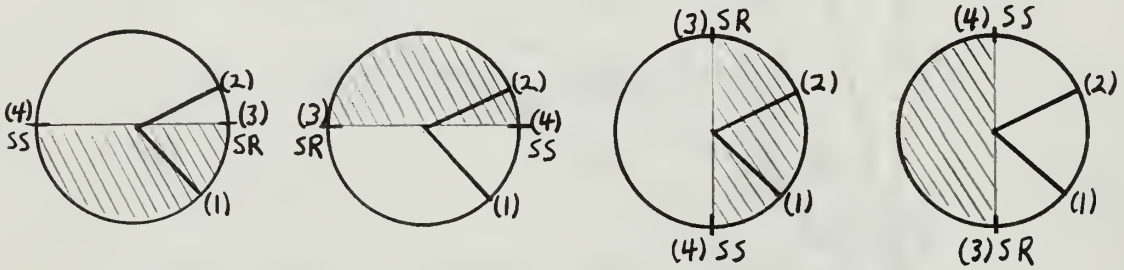

case A case B case C case D

Figure II-7. Possible positions of sunrise and sunset on great circle path

The actual program is shown on pages 116 through 120. The geodesic program was converted to a subroutine for convenience here. In the program the declination of the sun as a function of the time of the year is approximated by two sine waves of different periods; one being used from the 1st to the 80th and the 267th to the 365th days, and the other being used from the 81st to the 266th day. Data from the Nautical Almanac [17] was used as a guide in setting up this approximation.

The program also includes a correction factor for the Greenwich Hour Angle, which was also found necessary from data in the Nautical Almanac. This correction factor has a maximum value of 4.1 degrees (this changes λ_2 in Figure II-1) and is again approximated by sine

waves of various periods and amplitudes (see statements 311, 511, 711, and 812 in the program).

Geocentric latitudes, obtained from the geodesic program, are used so that no error is involved due to the ellipticity of the earth. The radius of the earth is not even used in this program, since the distances between points are expressed as arc distances and the amount of daylight is expressed as a percentage of the long or short path.

The only inputs required are the time of day and the day of the year. The latitude and longitude of the two points of interest and the description of the great circle path through these points are obtained from the geodesic subroutine.

In the paper by Brady and Crombie [22] three basic simplifications were made which could result in some error. These were the assumptions that:

1) the sun is a point source,

2) atmospheric refraction can be neglected,

3) the earth is spherical.

The third assumption does not introduce any error in the program developed here because geocentric latitudes were used. The other two could, according to Brady and Crombie, result in errors of about 16 minutes and 34 minutes of arc respectively in the quantity Δd (Figure II-3). These errors, although small, could cause considerable error on high latitude great circle paths.

This program is not valid for the case in which the highest latitude on the path is greater than the quantity $(90^{o} - \alpha_{s})$. This causes a portion of the path to be continually in daylight or darkness (e.g., polar paths during the winter or summer) and the method used here breaks down.

```
..JOB0564F,MCKAY,J.D.EAY4
      PROGRAM SHADOW
C     THIS PROGRAM COMPUTES THE PERCENTAGE OF DARKNESS AND DAYLIGHT ON
C     THE LONG AND SHORT PATHS (GREAT CIRCLES) BETWEEN TWO POINTS ON
C     THE SURFACE OF THE EARTH FOR ANY TIME OF DAY(UT) AND ANY DAY OF
C     THE YEAR (D(N)). THE SPHERICAL EARTH IS USED, AND THE LATITUDES
C     USED ARE GEOCENTRIC LATITUDES. THE GREAT CIRCLE PATH USED IS
C     OBTAINED FROM THE GEODESIC SUBROUTINE.
      DIMENSION ALFA(2), XLAMDA(3), UT(24),D(365),XL(4),PT(24)
      PI = 3.1415926536
      RAD = PI/180.0
      DER = 180.0/PI
    4 CALL       GDSC(PA   ,PB   ,PC   ,PHI1,ZL1,PHI2,ZL2,GAM,ZL3,
     1 ENDFLAG,DISTKM,DLNGKM)
      IF (ENDFLAG) 42,3,42
    3 CONTINUE
      DAY = 244.
      ALFA(1)=GAM*RAD
      XLAMDA(1) = ZL3*RAD
      I = 1
      D(I) = DAY
      PRINT 11 D(I)
   11 FORMAT(10X7H DAY = F5.0)
      PRINT 10
   10 FORMAT(120H                                        SHORT PATH          LONG PATH
     1                                                                              )
      PRINT 9
    9 FORMAT(120H       UT    PDT                 DAYLIGHT           DAYLIGHT
     1                                                                              )
      DO 32 K = 1,24
      IF (D(I) - 80.1) 60,60,70
   60 ALFA(2) =SINF((360./357.2)*(D(I)-80.1)*RAD)*(23.+(26.7/60.))*RAD
     1 + PI/2.
      GO TO 100
   70 IF (D(I) -266.5) 80,90,90
   80 ALFA(2) =SINF((360./373.2)*(D(I)-80.1)*RAD)*(23.+(26.7/60.))*RAD
```

```
     1 + PI/2.
      GO TO 100
  90 ALFA(2) =SINF((360./357.2)*(D(I)-87.9)*RAD)*(23.+(26.7/60.))*RAD
     1 + PI/2.
 100 UT(K)=FLOATF(K)
      PT(K) = FLOATF(K + 17)
      IF(PT(K) - 24.) 211,211,111
 111 PT(K) = PT(K) - 24.
 211 CONTINUE
      XLAMDA(2)= (UT(K)*15. - 90.)*RAD
C     THE FOLLOWING ARE CORRECTIONS NECESSARY TO OBTAIN THE CORRECT GHA
      IF(D(I) - 105.) 311,911,411
 311 XLAMDA(2) = XLAMDA(2) - 3.573*SINF((2.*PI/222.84)*(D(I) - 005.50))
     1 *RAD
      GO TO 911
 411 IF(D(I) - 165.) 511,911,611
 511 XLAMDA(2) = XLAMDA(2) + 00.94*SINF((2.*PI/118.58)*(D(I) - 105.92))
     1 *RAD
      GO TO 911
 611 IF(D(I) - 244.) 711,911,811
 711 XLAMDA(2) = XLAMDA(2) - 01.61*SINF((2.*PI/159.08)*(D(I) - 165.21))
     1 *RAD
      GO TO 911
 811 IF(D(I) - 359.) 812,911,311
 812 XLAMDA(2) = XLAMDA(2) + 004.1*SINF((2.*PI/114.75)*(D(I) - 244.75))
     1 *RAD
 911 CONTINUE
      B=0.5*(ALFA(1) + ALFA(2))
      C = 0.5*(ALFA(1) - ALFA(2))
      DA= TANF(0.5*(XLAMDA(2) - XLAMDA(1)))
      A = ATANF(DA*SINF(C)/SINF(B))+ ATANF(DA*COSF(C)/COSF(B))
      XLONG3 = XLAMDA(2) - ATANF(COSF(ALFA(2))*TANF(A))
      XLAT3 = ASINF(SINF(ALFA(2))*SINF(A))
      XLONG4 = XLONG3 + PI
      XLAT4 = -XLAT3
```

```
C     FOLLOWING IS A POSITION CORRECTION TO OBTAIN THE SR AND SS
C     POSITIONS AT A HEIGHT OF 70 KM ABOVE EARTH.
      SH = 30.
      R = 6370.
      DR = 70.
      Y =ACOSF((R + SH)/(R + DR))
      PSI = ACOSF(-COSF(ALFA(1))*COSF(ALFA(2)) + SINF(ALFA(1))*SINF(ALFA
     1(2))*COSF(XLAMDA(2) - XLAMDA(1)))
      IF (Y - PSI) 660,660,650
  650 SPD = 100.
      ZLPD = 100.
      GO TO 30
  660 CONTINUE
      DC = ASINF(SINF(Y)/SINF(PSI))
  670 CONTINUE
      PSI = ACOSF(SINF(ALFA(1))*COSF(XLONG3 - XLAMDA(1)))
      TH = ACTNF((CTNF(DC)*COSF(XLAT3) - SINF(XLAT3)*COSF(PSI))/SINF(PSI
     1 ))
      XLONG3 = XLONG3 + TH
      XLAT3 =ASINF(SINF(XLAT3)*COSF(DC) +COSF(XLAT3)*SINF(DC)*COSF(PSI))
      DC = -DC
      THL= ACTNF((CTNF(DC)*COSF(XLAT4) + SINF(XLAT4)*COSF(PSI))/SINF(PSI
     1 ))
      XLONG4 = XLONG4 + THL
      XLAT4 =ASINF(SINF(XLAT4)*COSF(DC) -COSF(XLAT4)*SINF(DC)*COSF(PSI))
      X14=SINF(PHI1)*SINF(XLAT4)+COSF(PHI1)*COSF(XLAT4)*COSF(ZL1-XLONG4)
      X13=SINF(PHI1)*SINF(XLAT3)+COSF(PHI1)*COSF(XLAT3)*COSF(ZL1-XLONG3)
      X24=SINF(PHI2)*SINF(XLAT4)+COSF(PHI2)*COSF(XLAT4)*COSF(ZL2-XLONG4)
      X23=SINF(PHI2)*SINF(XLAT3)+COSF(PHI2)*COSF(XLAT3)*COSF(ZL2-XLONG3)
      X= SINF(PHI1)*SINF(PHI2)+COSF(PHI1)*COSF(PHI2)*COSF(ZL1-ZL2)
      X14 =ACOSF(X14)
      X13 =ACOSF(X13)
      X24 =ACOSF(X24)
      X23 =ACOSF(X23)
      X =ACOSF (X)
      IF(ALFA(1) - ALFA(2)) 14,12,14
```

```
 12 IF(XLAMDA(1) - XLAMDA(2)) 14,13,14
 13 SPD = 0.
    ZLPD=0.
    GO TO 30
 14 XL(1)=0.
    XL(2)=ZL2 - ZL1
    XL(3) = XLONG3 - ZL1
    XL(4)= XLONG4 - ZL1
    DO 16 L=2,4
    IF(XL(L)) 15,115,115
 15 XL(L) = XL(L) + 2.*PI
115 IF(XL(L) - 2.*PI) 16,16,215
215 XL(L)=XL(L)-2.*PI
 16 CONTINUE
 17 IF(XL(3) - XL(2)) 117,119,18
117 IF(XL(4) - XL(2)) 217,219,19
217 IF(XL(4) - XL(3)) 119,119,219
 18 SPD = X23*100./X
    ZLPD = X24*100./(2.*PI-X)
    GO TO 30
 19 SPD = X14*100./X
    ZLPD = X13*100./(2.*PI-X)
    GO TO 30
119 SPD = 0.
    ZLPD =-(X14 + X23)*100./(2.*PI - X) + 100.0
    GO TO 30
219 SPD = 100.
    ZLPD = (X24 + X13)*100./(2.*PI - X)
 30 SPN = 100. - SPD
    ZLPN = 100. - ZLPD
 40 CONTINUE
    PRINT 32,UT(K),PT(K),SPD,ZLPD
 32 FORMAT(2X 2(3XF4.1),2(13XF6.2))
    GO TO 4
 42 END
```

PATH	GEODESIC KM	LONG PATH KM	GREAT CIRCLE DECL.	GREAT CIRCLE LONG.
TRINIDAD TO MONTEREY	6658.85	33391.48	37.45	47.45

DAY = 244.

UT	PDT	SHORT PATH DAYLIGHT	LONG PATH DAYLIGHT
1.0	18.0	54.48	51.11
2.0	19.0	44.66	51.40
3.0	20.0	42.79	50.04
4.0	21.0	.00	53.32
5.0	22.0	.00	54.90
6.0	23.0	.00	56.04
7.0	24.0	.00	56.94
8.0	1.0	.00	57.53
9.0	2.0	.00	57.38
10.0	3.0	36.13	49.34
11.0	4.0	39.61	52.94
12.0	5.0	57.44	51.97
13.0	6.0	76.80	48.61
14.0	7.0	100.00	54.69
15.0	8.0	100.00	53.39
16.0	9.0	100.00	52.69
17.0	10.0	100.00	52.32
18.0	11.0	100.00	52.16
19.0	12.0	100.00	52.12
20.0	13.0	100.00	52.14
21.0	14.0	100.00	52.20
22.0	15.0	100.00	52.40
23.0	16.0	90.94	45.66
24.0	17.0	70.44	49.07

APPENDIX III

LOOP ANTENNA CALCULATIONS

Consider Figure III-1 below. This is a schematic representation of a loop antenna showing a voltage generator in each vertical side of the loop to indicate the voltage induced by the passing wave. The z-axis is taken as the vertical axis and the xy plane the horizontal plane with respect to the earth. The voltage E_R appearing across the tuning

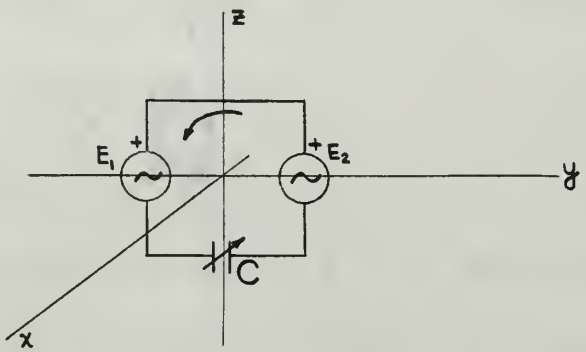

Figure III-1. Loop Antenna

capacitor C is the signal produced by the antenna and is found by phasor addition to be $\tilde{E}_R = \tilde{E}_2 - \tilde{E}_1$. The symbol $\sim$ here denotes a phasor quantity, while a letter without this indicates magnitude only.

In order to find the effect on the antenna output of various directions of arrival of the signal, assume the antenna to be rotatable about the z-axis. The angle α is defined as the angle between the normal to the loop and the direction of arrival of the signal, as shown in Figure III-2.

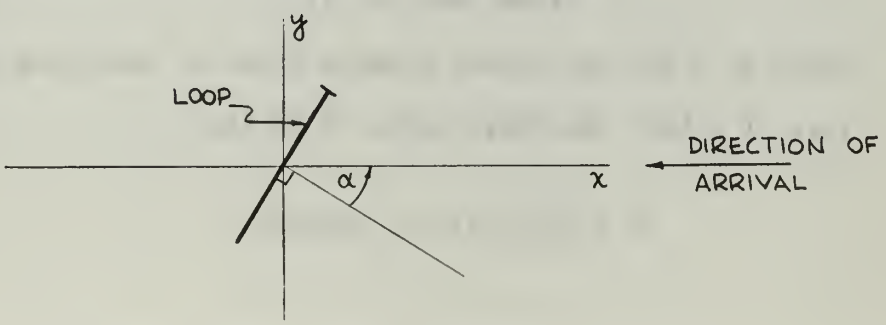

Figure III-2. Loop Geometry

The angle varies from 0^{o} to 360^{o} and taken to increase positively as the loop rotates clockwise. The bar shown on the loop in Figure III-2 is for reference and corresponds to side 2 of the loop as seen in Figure III-1.

The phasor diagram of the loop voltages is given in Figure III-3. The angle φ represents the phase of the antenna output signal, where $\varphi = 0$ when the loop is oriented broadside to the direction of arrival of the wavefront.

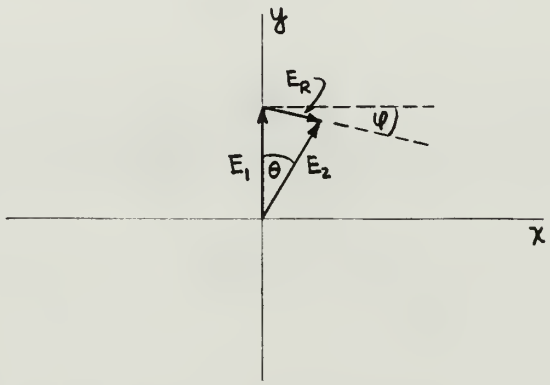

Figure III-3. Phasor Diagram

The angle θ in Figure III-3 represents the difference in phase between the voltage induced in side 2 and that in side 1 of the loop. It is determined by the distance d between the two vertical sides, and is given by

$$\theta = \frac{2\pi d}{\lambda} \sin\alpha \quad \text{radians, where}$$

λ = free-space wavelength of the received signal (same units as d).

Since $E_1 = E_2$, the phasor diagram forms an isosceles triangle and therefore $\varphi = \frac{1}{2}\theta$. The phase angle φ is then

$$\varphi = \frac{\pi d}{\lambda} \sin\alpha \quad \text{radians.}$$

The resultant E_R is also found readily from the phasor diagram. Using the Law of Cosines, one has

$$E_R^2 = E_1^2 + E_2^2 - 2E_1E_2 \cos \theta$$

$$= 2E_1^2 - 2E_1^2 \cos \theta$$

$$= 2E_1^2 (1 - \cos \theta)$$

$$E_R = E_1 \sqrt{2} (1 - \cos \theta)$$

$$= E_1 \sqrt{2} (\sqrt{2} \sin \frac{\theta}{2})$$

$$= 2E_1 \sin \varphi .$$

It is convenient to normalize by setting $E_1 = 1$. One can then express the magnitude of the relative output E_{out} in db below E_{Rmax}:

$$E_{out} = 20 \log_{10} \frac{E_R}{E_{Rmax}}$$

$$= 20 \log_{10} (\frac{2 \sin \varphi}{2 \sin \varphi_o}), \text{ where } \varphi_o = \varphi_{max}$$

$$= 20 \log_{10} (\frac{\sin \varphi}{\sin \varphi_o}) .$$

APPENDIX IV

CARDIOID ANTENNA CALCULATIONS

As in Appendix III, assume the direction of travel of the incoming signal fixed and the loop antenna rotatable, with the angle α defined as before; see Figure IV-1. In addition, the sense antenna is placed at some arbitrary position, forming the angle α' as shown. The distance d_s of the sense antenna from the loop midpoint is non-critical, so long as it is short with respect to a wavelength.

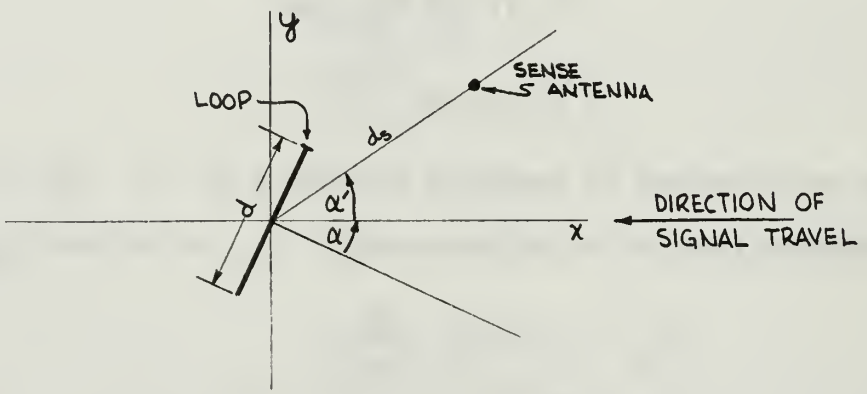

Figure IV-1. Cardioid Geometry.

Because of the 180° phase reversal of the loop antenna when $\alpha = 0°$ and 180°, it is convenient to analyze the cardioid system in two parts, with $0° < \alpha < 180°$ and with $180° < \alpha < 360°$ (or equivalently, $-180° < \alpha < 0°$). As in Appendix III, the loop phasor resultant $\tilde{E}_R$ is given by $\tilde{E}_2 - \tilde{E}_1$ and phase φ is $\theta/2$. This is illustrated in the phasor diagram of Figure IV-2. In this diagram, both θ and φ are taken to be negative angles.

For proper adjustment of the cardioid pattern, the magnitude and phase of the signal from the sense antenna must be made equal, respectively, to the magnitude and phase of the signal from the loop antenna when the loop is positioned for maximum response ($\alpha = 90°$). This

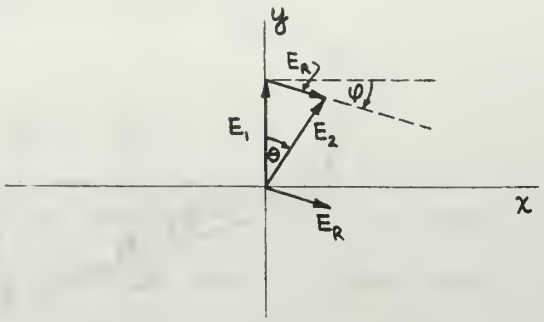

Figure IV-2. Loop Phasor Diagram

condition is shown in Figure IV-3, where E_s is the magnitude (after the necessary amplification and attenuation) of the sense antenna signal. The angle φ_o is the largest (negative) value of φ. Once set, the magnitude and phase of $\tilde{E}_s$, of course, remain constant as the loop is rotated.

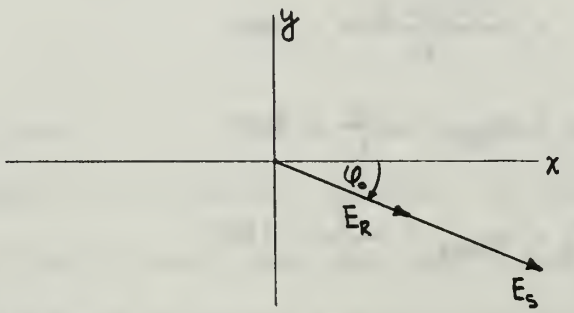

Figure IV-3. Cardioid Adjustment

The phasor diagram for some value of α between 0^o and 180^o, other than $\alpha = 90^o$, is shown below in Figure IV-4. The overall signal output of the cardioid unit is given by $E_o \angle \Upsilon^o$ (note that Υ is negative and its magnitude less than that of φ_o). This is obtained by the phasor relationship $\tilde{E}_o = \tilde{E}_R + \tilde{E}_s$, accomplished in the cardioid unit which mixes the loop and sense antenna signals.

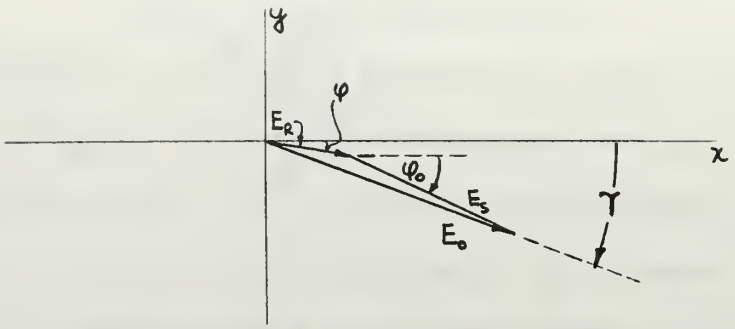

Figure IV-4. Cardioid Phasor Diagram

As in Appendix III, the angles φ, φ_o, θ, and θ_o may now be expressed in terms of the angle of loop orientation α, as follows:

$$\theta = \frac{-d \sin \alpha}{\lambda} \times 360^o \quad \text{(degrees)}$$

$$= \frac{-d \sin \alpha}{\lambda} \times 180^o$$

$$\theta_o = \theta_{max} = \frac{-d}{\lambda} \times 360^o$$

$$\varphi_o = \varphi_{max} = \frac{-d}{\lambda} \times 180^o$$

The objective is to find γ and E_o in terms of α. At this point, it is convenient to derive an expression for E_R as a function of E_s. This is done as follows, referring to Figure IV-2 and using the Law of Cosines:

$$E_R^2 = E_1^2 + E_2^2 - 2E_1E_2 \cos \theta$$

$$= 2E_1^2 (1 - \cos \theta), \quad \text{since } E_1 = E_2.$$

$$\therefore E_R = E_1 \sqrt{2} \sin \theta$$

$$\theta \doteq \sin \theta, \quad \text{since } \theta \text{ is small.}$$

$$\therefore \frac{E_R}{E_1} = \theta \sqrt{2}.$$

$$\frac{E_{Rmax}}{E_1} = \theta_o\sqrt{2} = \frac{E_s}{E_1} .$$

$$\therefore \frac{E_R}{E_s} = \frac{\theta}{\theta_o} .$$

Figure IV-5 is an expanded view of the phasor diagram of Figure IV-4, drawn on an exaggerated scale to make angular relationships clearer. In this diagram and the following equations, the fact that

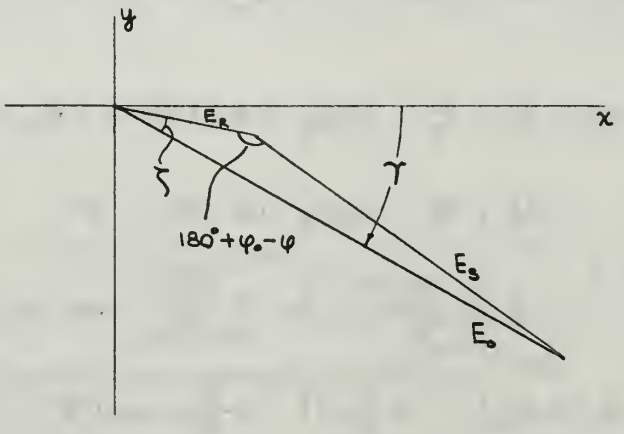

Figure IV-5. Angular Relationships

φ and φ_o are negative is taken into account. In the triangle of Figure IV-5, the two sides E_R and E_s and the angle between them are known, so that ζ may be found by geometry. One can then determine $\gamma = \varphi - \zeta$, which is the phase angle of $\tilde{E}_o$. Solving the triangle,

$$\zeta = 90^\circ - \frac{180^\circ + \varphi_o - \varphi}{2} + \tan^{-1}\left[\frac{E_s - E_R}{E_s + E_R}\cot\left(\frac{180^\circ + \varphi_o - \varphi}{2}\right)\right]$$

$$= 90^\circ - 90^\circ + \frac{\varphi - \varphi_o}{2} + \tan^{-1}\left[\frac{1 - \frac{\theta}{\theta_o}}{1 + \frac{\theta}{\theta_o}}\cot\left(90^\circ - \frac{\varphi - \varphi_o}{2}\right)\right]$$

$$\therefore \zeta = \frac{\varphi - \varphi_o}{2} + \tan^{-1}\left[\frac{1 - x}{1 + x}\tan\frac{\varphi - \varphi_o}{2}\right],$$

where $x = \frac{\theta}{\theta_o}$.

Since φ and ζ can be found for any given value of α, Υ is uniquely determined. It is a negative angle and $\varphi_o < \Upsilon < 0^o$ for $0^o < \alpha < 180^o$.

Determining the relative amplitude response for these values of α is very straightforward. Refer to Figure IV-5 and use the Law of Cosines as follows:

$$E_o^2 = E_R^2 + E_s^2 - 2E_RE_s \cos\left[180^o + (\varphi_o - \varphi)\right]$$

$$= E_R^2 + E_s^2 + 2E_RE_s \cos(\varphi_o - \varphi)$$

$$= E_R^2\left[\left(\frac{E_R}{E_s}\right)^2 + 1 + 2\frac{E_R}{E_s}\cos(\varphi_o - \varphi)\right]$$

$$E_o = E_s\sqrt{1 + \left(\frac{\theta}{\theta_o}\right)^2 + 2\frac{\theta}{\theta_o}\cos(\varphi_o - \varphi)}$$

$$\frac{E_o}{E_s} = \sqrt{1 + x^2 + 2x\cos(\varphi_o - \varphi)}$$

One may now normalize by setting $E_s = 1$ and taking $20\log_{10}E_o$ to obtain relative output in db, with zero db occurring at $\alpha = 0^o$ and 180^o:

$$E_o = 20\log_{10}\sqrt{1 + x^2 + 2x\cos(\varphi_o - \varphi)} \quad \text{db.}$$

The procedures for obtaining cardioid phase and amplitude for loop positions $180^o < \alpha < 360^o$ are quite similar to the methods given above. Figures IV-6 and IV-7 below are self-explanatory and are analogous to Figures IV-2 and IV-4, respectively, discussed above.

Angles are similar to those determined before, the principal difference being that 180^o is now added to φ due to the difference in loop position. Note that all of the following angles are now positive, while Υ remains negative:

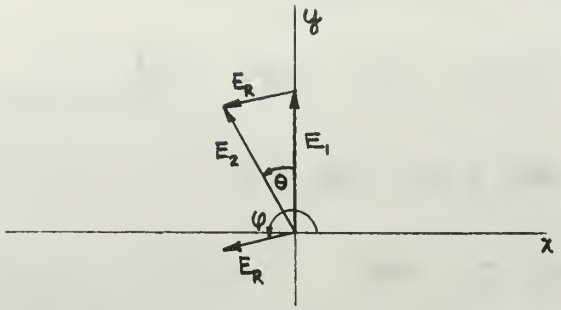

Figure IV-6. Loop Phasors ($180^o < \alpha < 360^o$)

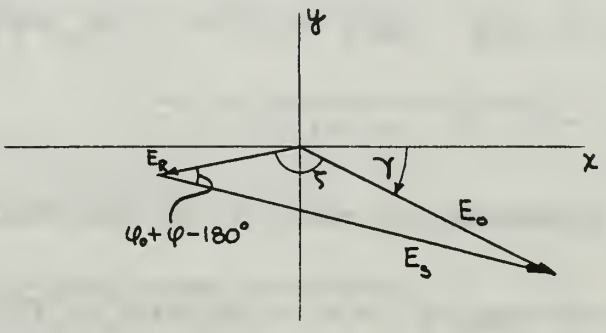

Figure IV-7. Cardioid Phasors ($180^o < \alpha < 360^o$)

$$\theta = -\frac{d}{\lambda} \sin \alpha \times 360^o$$

$$= 180^o - \frac{d}{\lambda} \sin \alpha \times 180^o$$

$$\varphi_o = \frac{d}{\lambda} \times 180^o$$

$$\theta_o = \frac{d}{\lambda} \times 360^o.$$

As before, ζ is found by trigonometry as follows:

$$\zeta = 90^o - \frac{(\varphi_o + \varphi - 180^o)}{2} + \tan^{-1} \left[\frac{E_s - E_R}{E_s + E_R} \cot \left(\frac{\varphi_o + \varphi - 180^o}{2} \right) \right]$$

$$= 180^o - \frac{\varphi_o + \varphi}{2} + \tan^{-1} \left[\frac{x-1}{x+1} \tan \frac{\varphi_o + \varphi}{2} \right].$$

$$|\Upsilon| = 180^\circ - [(\varphi - 180^\circ) + \zeta]$$

$$\therefore \Upsilon = -\{180^\circ - [(\varphi - 180^\circ) + \zeta]\}$$

$$= -180^\circ + \varphi - 180^\circ + \zeta$$

$$\Upsilon = \varphi + \zeta - 360^\circ.$$

Relative amplitude is found as before using the Law of Cosines, and referring to Figure IV-7:

$$E_o^2 = E_s^2 + E_R^2 - 2E_R E_S \cos\left[180^\circ - (\varphi_o + \varphi)\right]$$

$$\therefore \frac{E_o}{E_s} = \sqrt{1 + x^2 + 2x \cos(\varphi_o + \varphi)}\ .$$

Normalizing and expressing the result in db, one obtains:

$$E_o = 20 \log_{10} \sqrt{1 + x^2 + 2x \cos(\varphi_o + \varphi)} \quad \text{db.}$$

INITIAL DISTRIBUTION LIST

		No. Copies
1.	Defense Documentation Center Cameron Station Alexandria, Virginia 23314	20
2.	Library Naval Postgraduate School Monterey, California 93940	2
3.	Commander, Ship Systems Command Department of the Navy Washington, D. C. 20360	1
4.	Commander, Electronic Systems Command Department of the Navy Washington, D. C. 20360	1
5.	J. H. Stanbrough, Jr. Woods Hole Oceanographic Institution Woods Hole, Massachusetts 02543	1
6.	M. L. Tibbals Navy Electronics Laboratory San Diego, California 92152	1
7.	Prof. C. E. Menneken (Thesis Advisor) Dean of Research Administration Naval Postgraduate School Monterey, California 93940	5
8.	LT John Douglas McKay 19070 Wood Melvindale, Michigan 48122	1
9.	LT Gerry Lee Preston 1010 S. Derby Denison, Texas 75021	1
10.	Commanding Officer Mine Defense Laboratory Panama City, Florida 32401	1

DOCUMENT CONTROL DATA - R&D

(Security classification of title, body of abstract and indexing annotation must be entered when the overall report is classified)

1. ORIGINATING ACTIVITY *(Corporate author)*

Naval Postgraduate School
Monterey, California 93940

2a. REPORT SECURITY CLASSIFICATION

UNCLASSIFIED

2b. GROUP

3. REPORT TITLE

AN INVESTIGATION OF FACTORS WHICH DEGRADE PHASE ACCURACY IN A VLF RELATIVE NAVIGATION SYSTEM

4. DESCRIPTIVE NOTES *(Type of report and inclusive dates)*

Thesis, M.S., December 1966

5. AUTHOR(S) *(Last name, first name, initial)*

MCKAY, John Douglas and PRESTON, Gerry Lee

6. REPORT DATE	7a. TOTAL NO. OF PAGES	7b. NO. OF REFS
December 1966	132	32

8a. CONTRACT OR GRANT NO.	9a. ORIGINATOR'S REPORT NUMBER(S)
b. PROJECT NO.	
c.	9b. OTHER REPORT NO(S) *(Any other numbers that may be assigned this report)*
d.	

10. AVAILABILITY/LIMITATION NOTICES

This document has been approved for public release and sale; its distribution is unlimited. Newman 1/26/70

Qualified requesters may obtain copies of this report from DDC.

11. SUPPLEMENTARY NOTES	12. SPONSORING MILITARY ACTIVITY

13. ABSTRACT

A VLF relative navigation system makes use of the fact that, at any given point on the earth, phase delay of a received VLF signal is highly stable and predictable. As the receiver is physically moved, phase delay changes linearly with distance from the transmitting station, so that by keeping track of the phase delay of the received signal from several VLF stations, one may keep an accurate plot of geographical position.

Two problems experienced in measuring phase delay are the diurnal shift and long path interference. An investigation is made into a method of predicting the diurnal phase shift and the resultant phase due to simultaneous reception of long and short path signals. Also investigated is a receiving antenna having a cardioid shaped radiation pattern which could provide discrimination against long path signals.

DD FORM 1 JAN 64 1473

14. KEY WORDS	LINK A		LINK B		LINK C	
	ROLE	WT	ROLE	WT	ROLE	WT
VLF Antennas						
VLF Attenuation						
VLF Navigation						
VLF Phase Delay						
VLF Propagation						
Cardioid Antennas						
Geodesic						
Loop Antennas						
Relative Navigation						

INSTRUCTIONS

1. ORIGINATING ACTIVITY: Enter the name and address of the contractor, subcontractor, grantee, Department of Defense activity or other organization *(corporate author)* issuing the report.

2*a*. REPORT SECURITY CLASSIFICATION: Enter the overall security classification of the report. Indicate whether "Restricted Data" is included. Marking is to be in accordance with appropriate security regulations.

2*b*. GROUP: Automatic downgrading is specified in DoD Directive 5200.10 and Armed Forces Industrial Manual. Enter the group number. Also, when applicable, show that optional markings have been used for Group 3 and Group 4 as authorized.

3. REPORT TITLE: Enter the complete report title in all capital letters. Titles in all cases should be unclassified. If a meaningful title cannot be selected without classification, show title classification in all capitals in parenthesis immediately following the title.

4. DESCRIPTIVE NOTES: If appropriate, enter the type of report, e.g., interim, progress, summary, annual, or final. Give the inclusive dates when a specific reporting period is covered.

5. AUTHOR(S): Enter the name(s) of author(s) as shown on or in the report. Enter last name, first name, middle initial. If military, show rank and branch of service. The name of the principal author is an absolute minimum requirement.

6. REPORT DATE: Enter the date of the report as day, month, year; or month, year. If more than one date appears on the report, use date of publication.

7*a*. TOTAL NUMBER OF PAGES: The total page count should follow normal pagination procedures, i.e., enter the number of pages containing information.

7*b*. NUMBER OF REFERENCES: Enter the total number of references cited in the report.

8*a*. CONTRACT OR GRANT NUMBER: If appropriate, enter the applicable number of the contract or grant under which the report was written.

8*b*, 8*c*, & 8*d*. PROJECT NUMBER: Enter the appropriate military department identification, such as project number, subproject number, system numbers, task number, etc.

9*a*. ORIGINATOR'S REPORT NUMBER(S): Enter the official report number by which the document will be identified and controlled by the originating activity. This number must be unique to this report.

9*b*. OTHER REPORT NUMBER(S): If the report has been assigned any other report numbers *(either by the originator or by the sponsor)*, also enter this number(s).

10. AVAILABILITY/LIMITATION NOTICES: Enter any limitations on further dissemination of the report, other than those imposed by security classification, using standard statements such as:

(1) "Qualified requesters may obtain copies of this report from DDC."

(2) "Foreign announcement and dissemination of this report by DDC is not authorized."

(3) "U. S. Government agencies may obtain copies of this report directly from DDC. Other qualified DDC users shall request through

_____."

(4) "U. S. military agencies may obtain copies of this report directly from DDC. Other qualified users shall request through

_____."

(5) "All distribution of this report is controlled. Qualified DDC users shall request through

_____."

If the report has been furnished to the Office of Technical Services, Department of Commerce, for sale to the public, indicate this fact and enter the price, if known.

11. SUPPLEMENTARY NOTES: Use for additional explanatory notes.

12. SPONSORING MILITARY ACTIVITY: Enter the name of the departmental project office or laboratory sponsoring *(paying for)* the research and development. Include address.

13. ABSTRACT: Enter an abstract giving a brief and factual summary of the document indicative of the report, even though it may also appear elsewhere in the body of the technical report. If additional space is required, a continuation sheet shall be attached.

It is highly desirable that the abstract of classified reports be unclassified. Each paragraph of the abstract shall end with an indication of the military security classification of the information in the paragraph, represented as *(TS)*, *(S)*, *(C)*, *or (U)*.

There is no limitation on the length of the abstract. However, the suggested length is from 150 to 225 words.

14. KEY WORDS: Key words are technically meaningful terms or short phrases that characterize a report and may be used as index entries for cataloging the report. Key words must be selected so that no security classification is required. Identifiers, such as equipment model designation, trade name, military project code name, geographic location, may be used as key words but will be followed by an indication of technical context. The assignment of links, roles, and weights is optional.

DD FORM 1 JAN 64 1473 (BACK)